A Computational and Experimental Study of Viscous Flow Around Cavitating Propulsors

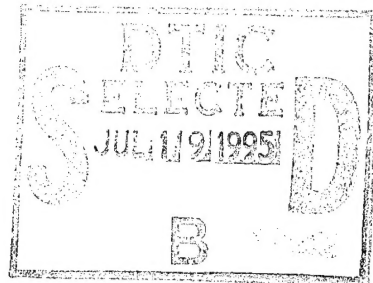### Wesley H. Brewer

19950717 096

Report 95-4

MASSACHUSETTS INSTITUTE OF TECHNOLOGY
DEPARTMENT OF OCEAN ENGINEERING
CAMBRIDGE, MA 02139

Report No. 95-4

A Computational and Experimental Study of Viscous Flow Around Cavitating Propulsors
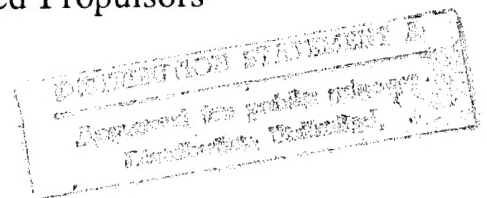
Wesley H. Brewer

June 1995

REPORT DOCUMENTATION PAGE		READ INSTRUCTIONS BEFORE COMPLETING FORM
1. REPORT NUMBER 95-4	2. GOVT ACCESSION NO.	3. RECIPIENT'S CATALOG NUMBER
4. TITLE *(and Subtitle)* A Computational and Experimental Study of Viscous Flow Around Cavitating Propulsors		5. TYPE OF REPORT & PERIOD COVERED Technical Report
		6. PERFORMING ORG. REPORT NUMBER
7. AUTHOR(s) Wesley H. Brewer		8. CONTRACT OR GRANT NUMBER(s) N00014-90-J-1086
9. PERFORMING ORGANIZATION NAME AND ADDRESS Department of Ocean Engineering Massachusetts Institute of Technology 77 Mass. Ave., Cambridge, MA 02139		10. PROGRAM ELEMENT, PROJECT, TASK AREA & WORK UNIT NUMBERS
11. CONTROLLING OFFICE NAME AND ADDRESS Office of Naval Research 800 North Quincy St. Arlington, VA 22217-5660		12. REPORT DATE June 1995
		13. NUMBER OF PAGES
14. MONITORING AGENCY NAME & ADDRESS*(if different from Controlling Office)*		15. SECURITY CLASS. *(of this report)* Unclassified
		15a. DECLASSIFICATION/DOWNGRADING SCHEDULE
16. DISTRIBUTION STATEMENT *(of this Report)* Approved for public release; distribution unlimited		
17. DISTRIBUTION STATEMENT *(of the abstract entered in Block 20, if different from Report)*		
18. SUPPLEMENTARY NOTES		
19. KEY WORDS *(Continue on reverse side if necessary and identify by block number)* Cavitation Viscous Flows Boundary Layers Hydrofoils		

20. ABSTRACT *(Continue on reverse side if necessary and identify by block number)*

A method for analyzing viscous flow around partially-cavitating and super-cavitating hydrofoils is presented. A nonlinear perturbation potential-based panel method is used to first solve the cavity solution in inviscid flow. A boundary layer solver is then applied on the surface bounded by the union of the foil and cavity surface. The effects of viscosity on lift and drag are studied for both partial and super-cavitating hydrofoils. Viscosity is shown to have a substantial effect in the condition of partial cavitation; on the other

DD FORM 1473 EDITION OF 1 NOV 65 IS OBSOLETE
1 JAN 73
S/N 0102-014-6601

hand, minimal deviations from the inviscid solution are observed in the case of super-cavitation. Finally, the applicability of the present method to analyzing the viscous flow around cavitating propulsors is discussed.

Experiments are performed at the MIT Variable Pressure Water Tunnel to ultimately assess the validity of coupled inviscid/viscous cavity analysis method. Velocities are measured along a rectangular control surface surrounding the hydrofoil, in the boundary layer region, as well as in the proximity of the cavity surface. The cavitation number is evaluated by measuring the pressure inside the cavity via a manometer. The measurements are compared to the numerical results from the coupled, nonlinear, inviscid cavity analysis method and a boundary layer solver. Forces are computed from measured velocities via momentum integrations and are compared with those predicted by the numerical method.

A Computational and Experimental Study of Viscous Flow Around Cavitating Propulsors

by

Wesley H. Brewer

B.S., University of Tennessee (1993)

Submitted to the Department of Ocean Engineering
in partial fulfillment of the requirements for the degree of

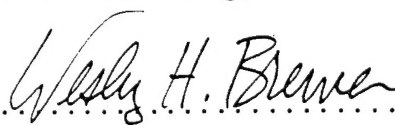Master of Science in Ocean Engineering

at the

MASSACHUSETTS INSTITUTE OF TECHNOLOGY

June 1995
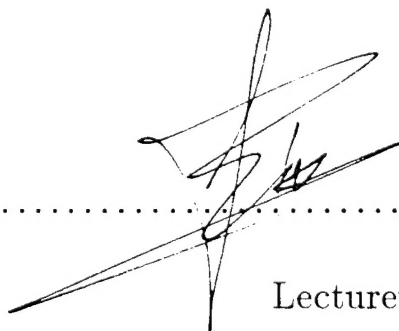
© Massachusetts Institute of Technology 1995

Signature of Author . . . .
Department of Ocean Engineering
May 1995
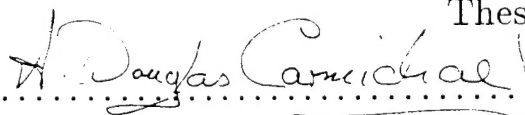
Certified by . . . .
Dr. Spyros A. Kinnas
Lecturer and Principal Research Engineer
Thesis Supervisor

Accepted by . . . .
Professor A. Douglas Carmichael
Chairman, Departmental Committee on Graduate Students

A Computational and Experimental Study of Viscous Flow Around Cavitating Propulsors

by

Wesley H. Brewer

Submitted to the Department of Ocean Engineering
on May 1995, in partial fulfillment of the
requirements for the degree of
Master of Science in Ocean Engineering

Abstract

A method for analyzing viscous flow around partially-cavitating and super-cavitating hydrofoils is presented. A nonlinear perturbation potential-based panel method is used to first solve the cavity solution in inviscid flow. A boundary layer solver is then applied on the surface bounded by the union of the foil and cavity surface. The effects of viscosity on lift and drag are studied for both partial and super-cavitating hydrofoils. Viscosity is shown to have a substantial effect in the condition of partial cavitation; on the other hand, minimal deviations from the inviscid solution are observed in the case of super-cavitation. Finally, the applicability of the present method to analyzing the viscous flow around cavitating propulsors is discussed.

Experiments are performed at the MIT Variable Pressure Water Tunnel to ultimately assess the validity of coupled inviscid/viscous cavity analysis method. Velocities are measured along a rectangular control surface surrounding the hydrofoil, in the boundary layer region, as well as in the proximity of the cavity surface. The cavitation number is evaluated by measuring the pressure inside the cavity via a manometer. The measurements are compared to the numerical results from the coupled, nonlinear, inviscid cavity analysis method and a boundary layer solver. Forces are computed from measured velocities via momentum integrations and are compared with those predicted by the numerical method.

Thesis Supervisor: Dr. Spyros A. Kinnas
Title: Lecturer and Principal Research Engineer

Acknowledgements

This thesis represents the work of which many people have contributed; I am very fortunate to be working among such a talented group of people. I am gratefully indebted to Spyros Kinnas for more than generous amounts of encouragement, advice, and assistance. Dr. Kinnas' unselfish motivation to help students has granted me the opportunity to achieve many goals that otherwise would not have been possible. I would also like to thank Professor Drela for his assistance in adapting the viscous routines of XFOIL to cavitating flow. Also, much thanks goes to Professor Justin Kerwin for his excellent advice in times of need and to all those in the propeller group. I especially would like to express my appreciation to Shige Mishima, whose talented help in both academics and research was invaluable to the completion of this work. I am also grateful to my roommate Jesse Hong, for his expert advice on computers and for putting up with me over the years. Additional thanks go to our UROP'S Matt Knapp, Dianne Egnor, and Luke Sosnowski, for helping out in all phases of the experiment.

Most importantly I would like to thank my fiancé Jenny, to whom I dedicate this thesis. Her constant love, devotion, and support has made graduate school much more fulfilling.

Much support also came from friends and family. A special thanks goes to my mother, for always believing in me. I could not have made it through college and graduate school without her substantial financial and emotional support. I also thank my dad for always inspiring me to the best and showing me a strong work ethic, and Michelle for always giving encouragement in times of need. Lastly, but most importantly, I would like to thank God who makes all things possible.

Contents

Nomenclature

B	bias limit
c	chord
C_d	dissipation coefficient $= (1/\rho_e u_e^3) \int \tau (\partial u/\partial \eta) d\eta$
C_D	drag coefficient $= D/\frac{1}{2}\rho U_\infty^2 c$
C_f	skin-friction coefficient $= 2\tau_{wall}/\rho u_e^2$
C_L	lift coefficient $= L/\frac{1}{2}\rho U_\infty^2 c$
C_P	pressure coefficient $= (p - p_\infty)/\frac{1}{2}\rho U_\infty^2$
C_τ	shear stress coefficient $= \tau_{max}/\rho U_e^2$
$C_{\tau_{EQ}}$	equilibrium shear stress coefficient
h	mercury level in manometer
H	shape factor $= \delta^*/\theta$
H^*	kinetic energy shape parameter $= \theta^*/\theta$
H_k	kinematic shape parameter
	$= \int [1 - (u/U_e)]d\eta \div \int (u/U_e)[1 - (u/U_e)]d\eta$
l	cavity length
$\boldsymbol{n}$	foil surface unit normal vector
$\tilde{n}$	transition disturbance amplification variable
N	number of velocity samples
p_k	measured cavity pressure
p_v	vapor pressure of water
p_∞	free-stream pressure
P	precision limit $= tS$
$\boldsymbol{q}_c$	cavity surface velocity vector

s	arclength along foil surface
S_u	precision index of the mean $= \sigma_u/\sqrt{N}$
t	coverage factor
t_{max}	maximum thickness of foil section
u, w	horizontal and vertical velocities
U	uncertainty estimate
U_e	edge velocity
U_∞	free-stream velocity
x	stream-wise distance
y	vertical distance (analytical)
z	vertical distance (experimental)

α	angle of attack
δ	boundary layer thickness
δ^*	boundary layer displacement thickness $= \int(1 - u/U_e)dy$
θ	boundary layer momentum thickness
	$= \int u/U_e(1 - u/U_e)dy$
θ^*	kinetic energy thickness $= \int(u/u_e)[1 - u^2/u_e^2]dy$
ρ_{H_2O}	water density
ρ_{Hg}	mercury density
ρ_{LE}	leading edge radius of foil
σ	cavitation number $= (p_\infty - p_v)/\frac{1}{2}\rho U_\infty^2$
σ_u	standard deviation of horizontal velocity
	measurements
$\hat{\sigma}$	blowing source strength
Φ	total velocity potential $= \Phi_{in}(x, y) + \phi(x, y)$
ϕ	perturbation potential
Φ_{in}	velocity inflow potential

List of Tables

List of Figures

Chapter 1

Introduction

Cavitation is the manifestation of vapor pockets in a flowing liquid owing to a local minimization of pressure. This phenomenon of liquid vaporization has antagonized the design of propulsors by causing:

- diminished efficiency/performance

- excessive structural vibration (leading to failure)

- immense material corrosion due to the high forces involved in the bubble collapse

- flow noise

Cavitation is inevitably an issue in the design of efficient high speed pumps and propellers. Therefore, there is a great interest in studying the physics underlying the nature of cavitation. Research on cavitation was initiated in pursuit of developing methods to *control* cavitation: methods to design more efficient hydrofoils and propellers that use cavitation to their benefit.

In fact, optimally-cavitating propulsors can be more efficient than those designed to not cavitate. The presence of the cavity introduces the advantageous quality of having smaller viscous losses. However, it also introduces undesirable form drag, called *cavity drag*. Thus, the design of the most efficient propulsor represents a delicate balance between two extremes: no cavitation (large blade area with no cavity drag but high

viscous losses) *or* fully-cavitating (small blade area with minimal viscous losses but with cavity drag).

Computational tools have been of paramount importance in designing cavitating propulsors. These tools are developed in a systematic manner, starting with simple two-dimensional geometries in inviscid flow, working towards three-dimensional geometries in viscous flow. The philosophy underlying the development of the codes is to begin with the simplest model and progressively extend this model to more complicated and realistic flows. This work represents a small contribution in the efforts to ultimately develop an automated numerical method for the design of optimum propulsors.

This thesis attempts to address the issue of *viscosity* in cavitating flow. The effect of viscosity is studied by performing experiments on simple two-dimensional hydrofoils in cavitating flow. Knowledge obtained from experiments is then used to further develop existing computational methods to accurately model viscous flow around cavitating propulsors.

1.1   Research History

1.1.1   Experiments

Experimentation is an essential element in the study of cavitation. It is primarily useful for understanding the actual physics and details of the flow. A vast number of experiments have been conducted to investigate cavitation. The purpose in many of these experiments was to measure the lift, drag, and moment coefficients for various cavitation numbers. Parkin (1958) measured lift, drag, and pitching moment in cavitating and fully-wetted flow for flat plate and circular-arc sections. Meijer (1959) measured forces as well as pressures in the vicinity of the cavity trailing edge of a *partially-cavitating* hydrofoil. His experiments indicated essential differences between partially-cavitating and super-cavitating flows. Wade and Acosta (1966) studied the lift and drag on a plano-convex foil in the presence of partial and super cavitation. They also observed strong, periodic oscillations in both cavity length and forces acting on the hydrofoil. A secondary effort of

their experiments was to observe the formation and development of the cavity. Uhlman and Jiang (1977) studied the cavity length, for various cavitation numbers, on a plano-convex foil. There results were correlated to the theories of Wade (1967) and Geurst (1959). Maixner (1977) investigated the influence on wall effects on force and moment coefficients of a super-cavitating hydrofoil. His results were compared to the methods of Wu, Whitney, and Lin (1971).

Laser Doppler Velocimetry (LDV) measurements in the boundary layer, behind the cavity of a partially-cavitating hydrofoil, were performed by Kato et al (1987) and Fine (1988). Kato reported an appreciable increase in the boundary layer thickness due to the existence of cavitation. Kato also measured the unsteady flow in the presence of cloud cavitation using a conditional sampling technique. Lurie(1993) measured the formation of the *unsteady* boundary layer on a fully-wetted hydrofoil subject to sinusoidal gust (the Flapping Foil Experiment), in addition to unsteady pressures on the foil surface.

Kinnas and Mazel (1993) performed LDV measurements about a *super-cavitating* hydrofoil. They measured velocities near the cavity surface to calculate the cavitation number. Measurements were also made along a rectangular contour surrounding the foil and cavity. These measurements were used with momentum integrations to calculate the lift and drag forces acting on the hydrofoil. A list of earlier super-cavitating experiments is given in Kinnas and Mazel (1993).

1.1.2   Numerical Methods

Many codes have been developed over the past few years to aid the designer in developing optimal blade geometries. A history of numerical methods used to model sheet cavitation is given in Villeneuve (1993). The nonlinear perturbation potential method by Kinnas and Fine (1990) laid the groundwork for the viscous cavity model, **P2DBLWC**.

Villeneuve's viscous cavity analysis method was based on Drela's (1989) airfoil analysis code, XFOIL, which uses an interactive viscous-inviscid approach to solving the flow around airfoils. Drela's work was further developed by Hufford (1992) who applied the boundary layer method in a strip-wise sense to analyze the viscous flow around three-dimensional propeller blades. In doing this, Hufford coupled the viscous routines of
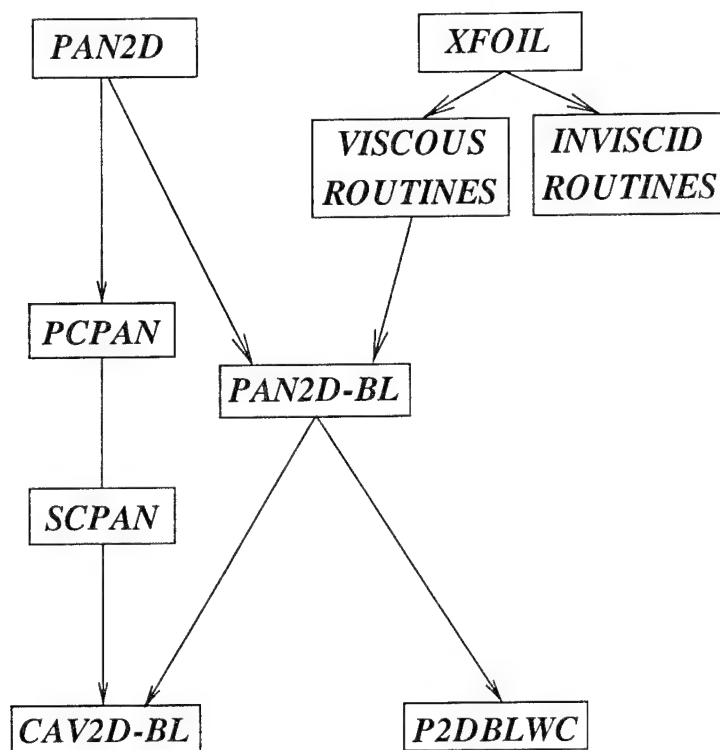
Figure 1-1: History of code development for two-dimensional cavitating boundary layer solver.

XFOIL to the inviscid perturbation potential method of PAN2D.[1] The history of the code is illustrated in Figure 1-1.

The scope of Villeneuve's work was divided into two strands: numerical and experimental. The numerical method, **P2DBLWC**, was based on Hufford's code, **PAN2D-BL**. To model the cavity, Villeneuve used a similar method to that used in boundary layer theory, where blowing sources were used to represent the cavity. This method is referred to as the "thin" cavity method, in which case both the cavity and the displacement thickness are assumed to be "small" with respect to the cavity length. Villeneuve's work also included the implementation of the method of images to account for the effects of tunnel walls.

To validate **P2DBLWC**, Villeneuve performed experiments on a partially-cavitating hydrofoil. In correlating experimental results with numerical predictions, he compared

---

[1]XFOIL uses a linear vorticity streamfunction formulation for inviscid flow (Drela, 1989).

P2DBLWC: "Thin" cavity approach   **CAV2D-BL: Nonlinear cavity approach**
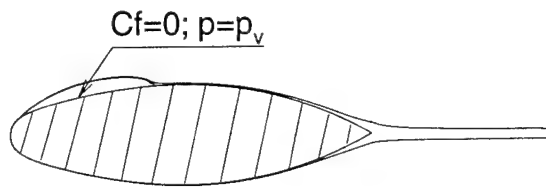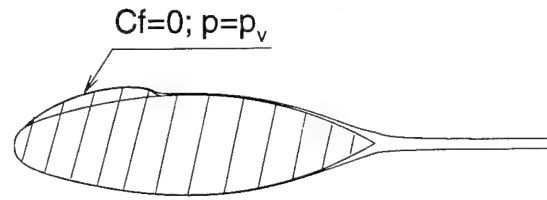
Figure 1-2: Hydrofoil with cavity and displacement thickness illustrating where boundary conditions are applied.

integral parameters, such as the boundary layer displacement and momentum thickness, as well as lift and drag coefficients. The predicted results by the analysis method were shown to be in good agreement with the experimental results.

1.2 Objectives

This thesis serves to continue Villeneuve's efforts to model viscous flow around cavitating hydrofoils. Instead of comparing integral parameters, such as the boundary layer displacement and momentum thickness (as Villeneuve did), the results herein compare actual velocities, which are predicted anywhere in the flowfield, with those from experiments. In doing this, a numerical method was developed to extract velocity profiles from the integral quantities given as a result of the boundary layer solver.

The secondary goal of this work lies in further developing the code **P2DBLWC**: increasing the versatility and robustness of the boundary layer solver used to model viscous cavitating hydrofoils.

To this end, the following improvements were made to **P2DBLWC**:

- The non-linear cavity method: The boundary layer is solved on the cavity surface resulting from "fully" non-linear cavity analysis.

- Implement a new spacing technique, blended spacing, which allows the user to specify the cavity detachment location exactly and ensures continuous panel spacing.

- Extend the method to super-cavitating sections.

- Fix bugs in the old code.

- Formulate and implement the "momentum jump" model which models the in-
  creased momentum and displacement thickness which occurs at the trailing edge
  of the cavity (as evidenced by experiments).

Villeneuve's "thin" cavity method, P2DBLWC, has been shown to work well when
the cavity is very thin compared to the foil thickness. In his method, he represents the
cavity and boundary layer by using blowing sources applied on the cavity surface as
shown in Figure 1-2. In this thesis, however, a different approach is used to model the
viscous flow around the cavity, namely, the nonlinear cavity approach, as shown in Figure
1-2. First, the cavity is generated in nonlinear theory, then the boundary conditions are
applied on the boundary surrounding the union of the cavity and foil surface. However,
the present method does not ensure that the dynamic boundary condition, requiring the
pressure to be constant on the cavity surface, is completely satisfied. The present method
only performs the first iteration of the inviscid/viscous coupling procedure. Kinnas et al
(1994) performed a second iteration of the present method, which showed not the affect
the results drastically.

The code incorporating these changes has been named CAV2D-BL – a **two-d**imensional
cavitating boundary layer solver.

Chapter 2

Experiment

The purpose of the partially-cavitating hydrofoil experiments (PACHE) is to acquire data which can be used to validate the coupled nonlinear cavity analysis method (PCPAN) and boundary layer solver (CAV2D-BL). Also of interest in these experiments is the study of how the cavity drag manifests itself into the wake. To fulfill these goals, velocity measurements and pressure measurements (cavitation numbers) were taken for various angles of attack and cavitation numbers.

PACHE was performed in three phases. The subsequent phases were necessary to fix problems in the previous phases. The following outline describes each phase of the experiment:

- Phase I:

  - Performed by: Shige Mishima, Cedric Savineau, Wesley Brewer, and Platon Velonias

  - Problems:

    * Fiber-optic beam was not working. Boundary layer measurements could only be taken with horizontal component of laser.

    * No turbulator strip on pressure side of foil introduced error in the prediction of the transition location.

- Phase II:

– Performed by: Wesley Brewer

– Corrections since phase I:

* Fiber-optic beam fixed.

* Turbulator strip placed on pressure side of foil.

– Phase II problems: Pressure measurements could not be taken because manometer was not working correctly.

• Phase III:

– Performed by: Wesley Brewer

– Corrections since phase II: Manometer fixed

– Phase III Problems: Manometer still not completely accurate.

2.1 Setup

The experiments were performed in the MIT Variable Pressure Water Tunnel (Kerwin, 1992). The tunnel has a twenty inch square testing cross-section enveloped on all sides by plexiglass windows. First, the tunnel was de-aired at low speeds using the vacuum pump; then, the pressure was dropped below the point of cavitation inception. One impeller, driven by a 75 horsepower motor, propels the water through the closed-loop tunnel at speeds up to 9 m/s (30 ft/s); a speed of 8 m/s (25 ft/s) was used for this experiment.

Figure 2-1 shows the experimental setup. The foil, a "heavy" symmetrical stainless-steel foil, has a chord of twelve inches and a span of twenty inches. The maximum thickness to chord ratio is twelve percent at half-chord. A turbulator strip was placed on the pressure side of the foil at 1/5 chord. Two rubber gaskets, squeezed in between the plexiglass window and the foil, served to prevent any secondary flow between the pressure and suction side. The foil was mounted on the vertical plexi-glass walls at two points on each side, as shown in Figure 2-1. A stainless-steel pin, set at approximately 3/4 chord, was used to adjust the angle of attack.

Figure 2-3 shows actual photographs of the cavitating hydrofoil in the testing section of the water tunnel. The top photo shows a very stable sheet cavity of extent 10%
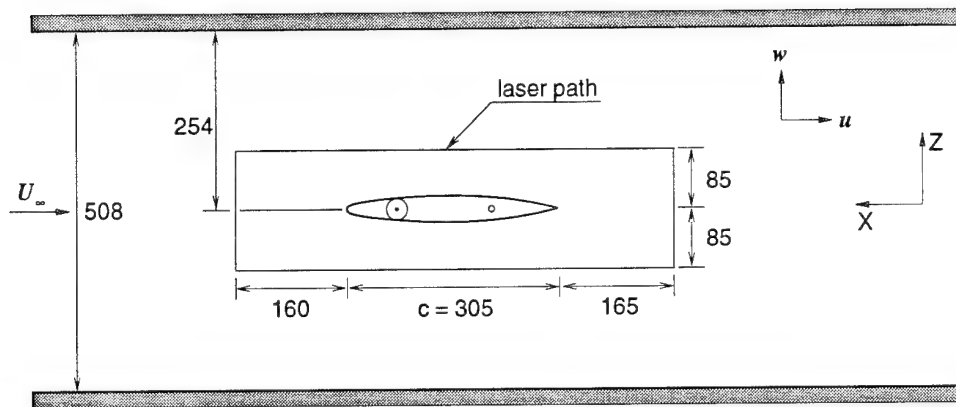
Figure 2-1: Experimental setup in water tunnel showing foil and contour path of laser (all units given in millimeters).

of the chord length. It is evident that the "clean appearance" of the cavity becomes worse for larger cavity lengths. The measurements also confirm that the amount of uncertainty increases with increasing cavity extent. Notice that the cavity detachment point is very pronounced in Figure 2-3, and very two-dimensional – an extremely desirable characteristic in studying cavity detachment location.

2.2 Velocity Measurements

The present section discusses issues related to the acquisition of velocities in the flow-field. A description of the method used in taking velocity measurements is first presented, followed by an analysis of the errors involved in the measurement process. A complete set of the measurements may be found in later sections, where they are compared to results of the analysis.

2.2.1 Procedure

Velocities can be taken instantaneously anywhere in the flow-field using the TSI model 9533 Argon Ion Laser Doppler Velocimeter (LDV). The crossing of two monochromatic
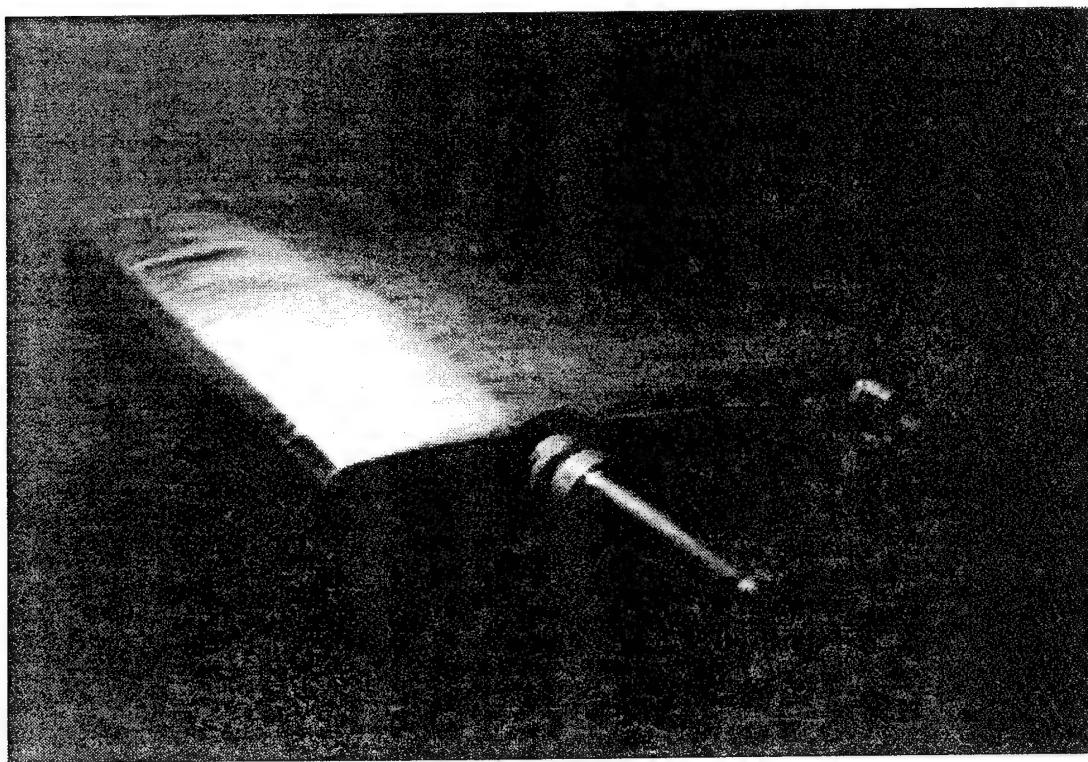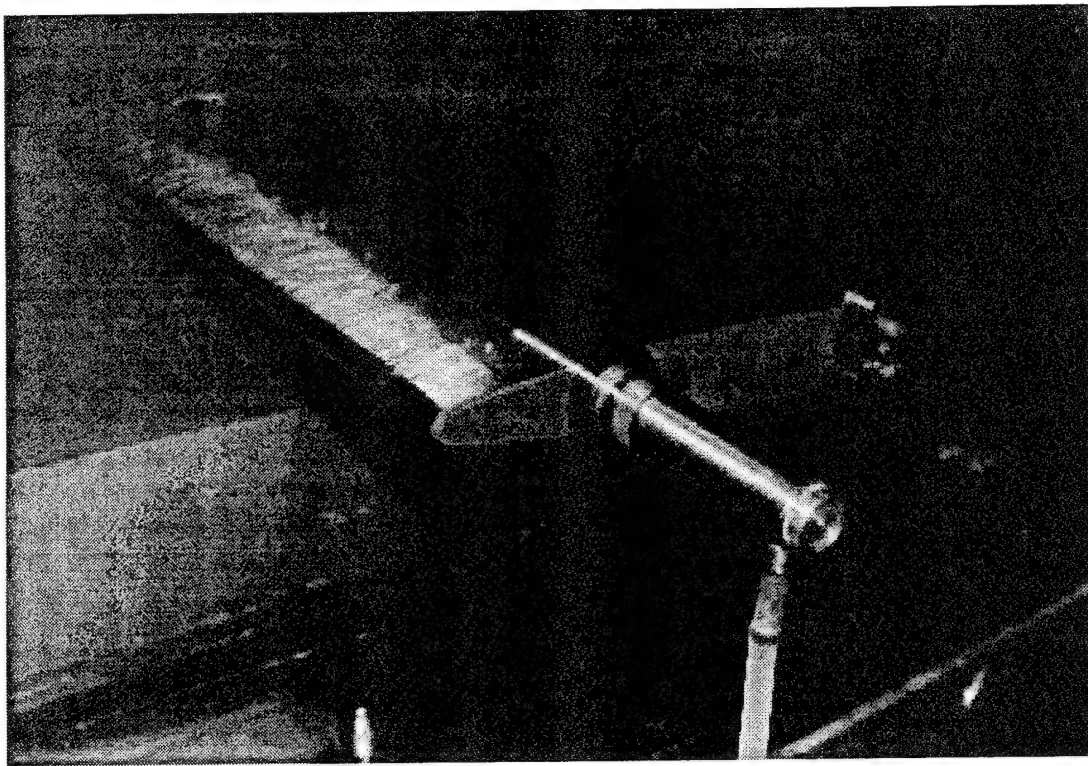
Figure 2-2: Photographs of the hydrofoil in the water tunnel testing section. Top: l/c=0.10, bottom: l/c= 0.20. $\alpha = 3.5^\circ$.
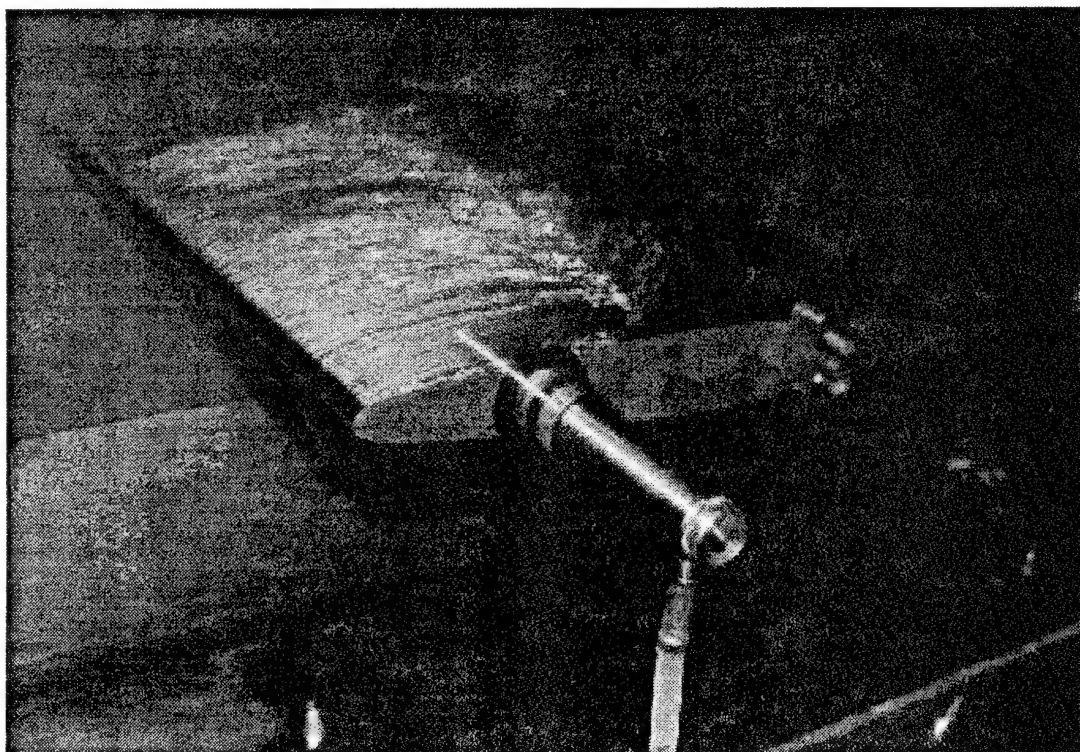
Figure 2-3: Photographs of the hydrofoil in the water tunnel testing section. Top: l/c=0.30, l/c=0.40. $\alpha = 3.5^\circ$.

beams creates an interference fringe pattern. Seed particles[1] in the flow create a disturbance in the fringe pattern; this disturbance is measured by a photodetector and then processed through digital signal analyzers, ultimately resulting in a velocity reading. A two-component optical laser was used in all phases of the experiment to measure velocities along the rectangular contour. In Phase I of the experiment, boundary layer velocities were acquired by the horizontal component of the laser (which cannot measure velocities within 1 - 3 mm of the foil surface). However in Phase II, boundary layer measurements were taken by a rotatable fiber-optic beam which measured velocities parallel to the foil surface.

At each data point, the LDV takes a user-specified number of samples, in this case 500. Velocities are rejected if they are greater than three standard deviations from the mean; the standard deviation and mean are recomputed with the reduced data set (Kinnas and Mazel, 1993). Figure 2-4 shows a representative set of "good" data with error bars attached. The error bars represent plus or minus a half standard deviation from the stream-wise velocity mean (solid line). The standard deviations ranged from approximately three percent in inviscid regions up to ten percent in viscous regions and near the cavity. In some unusual situations the measured velocity had a standard deviation which was in the order of twenty percent or more of the mean value.

Velocities were measured in the proximity of the cavity surface as well as in the boundary layer region behind the cavity, and along the sides of a box which surrounds the hydrofoil as shown in Figures 2-1 and 2-5. Table 2.1 not only lists the setup for each testing case, but also the observed cavity detachment and reattachment points, or cavity leading and trailing edges respectively.

The free-stream velocity, U_∞, is measured using a differential pressure cell far upstream of the hydrofoil. All velocity measurements are normalized on its respective instantaneous free-stream velocity. Typically, the free-stream velocity will drift, up to five percent, over the course of the experiment.

---

[1] Silver coated silicon carbide spheres 5 microns in diameter
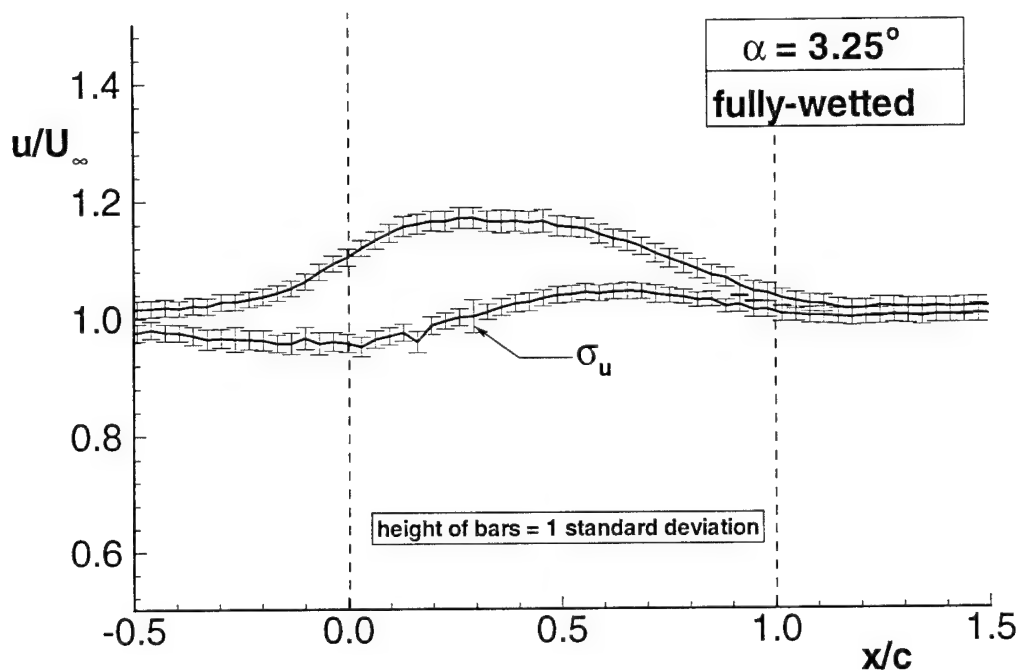
Figure 2-4: Horizontal velocity measurements on the top and bottom of a rectangular contour surrounding the hydrofoil with error bars showing plus or minus one-half standard deviation.
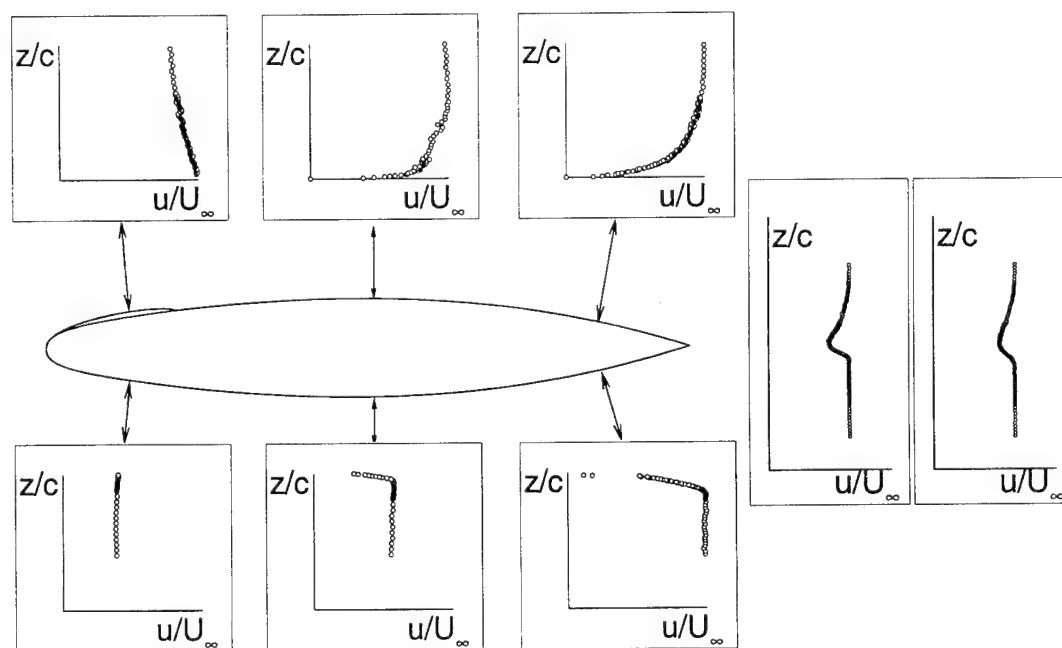
Figure 2-5: Example of boundary layer cuts near foil surface. $\alpha = 3.5^{\circ}$

Table 2.1: Testing cases and setup parameters at a free-stream velocity of 8 m/s (25 ft/s).

Phase	α	l/c	Cavity L.E.	Cavity T.E.	Measurement Type
I	0.4	0.0	—	—	Boundary layer/Contour
		0.4	0.01/0.50	0.1/0.80	Contour
	0.7	0.0	—	—	Boundary layer/Contour
		0.1	0.02	0.12	Contour
	1.66	0.0	—	—	Boundary layer/Contour
		0.1	0.02	0.11	Boundary layer/Contour
		0.2	0.01	0.20	Boundary layer/Contour
II	3.5°	0.0	—	—	Boundary layer/Contour
		0.1	0.02	0.20	Boundary layer/Contour
		0.2	0.02	0.25	Boundary layer/Contour
		0.3	0.02	0.32	Boundary layer/Contour
		0.4	0.02	(0.4)	Boundary layer/Contour
III	3.25°	0.0	—	—	Pressure/Contour
		0.1	0.024	0.13	Pressure/Cavity velocity
		0.2	0.025	0.24	Pressure/Cavity velocity
		0.3	0.025	0.34	Pressure/Cavity velocity
		0.4	0.021	0.47	Pressure/Cavity velocity

2.2.2 Errors in Velocity Measurements

Errors in the velocity measurements, as measured by the standard deviations, are composed of: 1) errors due to the random fluctuations, or turbulence, in the tunnel, and 2) errors associated with variations the data acquisition equipment. The turbulence value of the MIT facility is approximately one percent of the free-stream velocity. The following quantities contribute to the total error associated with the LDV:

- repeatability of the coordinate system

- variation of frequency shift

- calibration of the fringe spacing

- calibration of the flow angularity

By propagating these individual errors through a Taylor series expansion, the total error associated with each component (stream-wise, vertical, fiber-optic) of the LDV can be determined. This was recently done by Lurie (1995) to find the error characteristics of the laser in the Flapping Foil Experiment (FFX), which was also performed at the MIT Water Tunnel.

95% of the data should be expected to fall in a region, $+/-U$, where U is the total uncertainty of the data given by:

$$U = \sqrt{B^2 + P^2} \tag{2.1}$$

where B is the total bias limit of the propagated errors from each of the individual parameters listed above.

The precision limit, P, which is the range in which the mean of 95% of the data should fall, is defined as:

$$P = tS = \frac{t\sigma}{\sqrt{N}} \tag{2.2}$$

where S is the precision index and t is the coverage factor, equal to two for 95% coverage.

Table 2.2: The bias limit, precision limit, and uncertainty estimate of the Flapping Foil Experiment performed at the MIT Water Tunnel (adjusted from Lurie (1995)).

Component	B(m/s)	P(m/s)	U(m/s)	U/U_∞
inviscid				
stream-wise	0.055	0.00029	0.058	0.8%
vertical	0.061	0.00032	0.064	0.8%
viscous				
stream-wise	0.134	0.00012	0.155	2.0%
vertical	0.064	0.00041	0.101	1.3%
fiber-optic	0.244	0.00244	0.256	3.4%

Table 2.2 lists the bias limit, precision limit, and total uncertainty estimate from data obtained in the FFX. The total uncertainty for the current experiment should be of the same order as those given in Table 2.2. In inviscid flow the uncertainty estimate should be *very* close to that of the FFX. On the other hand, due to the difference in the nature of the two experiments,[2] the error associated with the viscous velocities, in our experiment, is less likely to be as high as that in the FFX.

2.3 Pressure Measurements

A manometer, shown in Figure 2-7, was used to measure the pressure on the suction side of the foil, where a pressure tap was located at $x/c = 0.05$, as shown in Figure 2-6.

In the case of cavitating flow, problems were encountered with the phenomenon of water vaporizing in the manometer. To remedy this problem, the manometer was moved to a level much lower than that of the pressure tap. This added pressure to the top reservoir, shown in Figure 2-7, by the amount $\rho_{H_2O}g\Delta z$, where Δz is the increased distance from the pressure tap to the manometer.

The following relation can be used to calculate the cavitation number or pressure coefficient on the foil.

---

[2]There were much larger pressure gradients in the FFX.

Top view
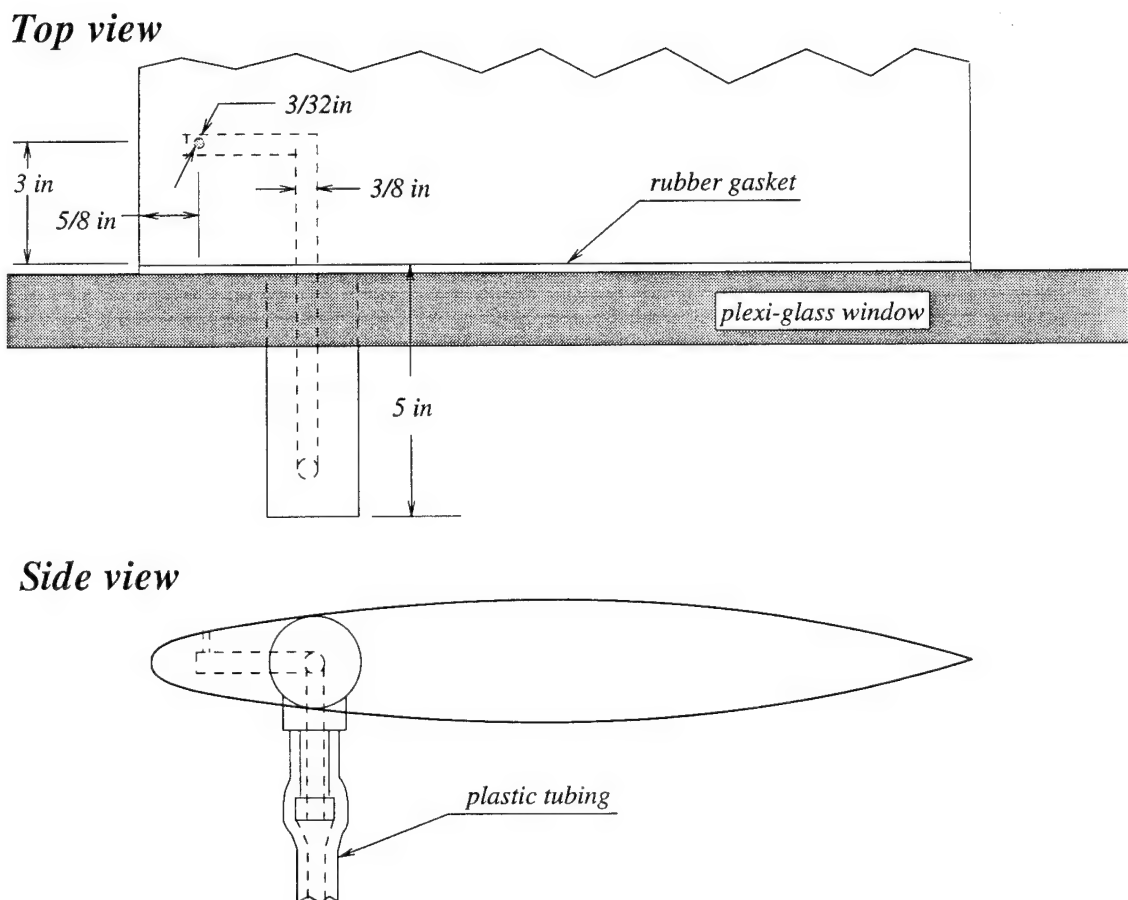
Side view

Figure 2-6: Top and side view of hydrofoil, in tunnel testing section, showing the location of the pressure tap.
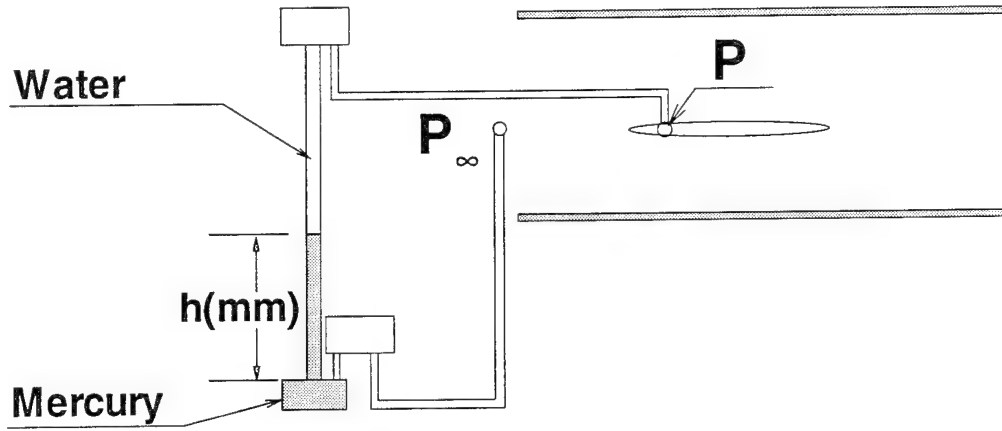
Figure 2-7: Manometer setup in water tunnel.

$$\sigma = -C_p = \frac{gh(\rho_{Hg} - \rho_{H_2O})}{\frac{1}{2}\rho_{H_2O}U_\infty^2} \tag{2.3}$$

where h is the height of the mercury level.

2.4 Geometry of the Foil

The foil used in the experiment has a zero-camber, symmetrical cross-section. Its geometry (originally unknown) was generated by first tracing the foil's section onto a piece of paper. From the trace on paper, the foil's thickness at many chordwise locations was measured. By fitting a fourth-order curve to those points, the following analytical expression for the foil thickness was derived, equation (2.4), in terms of the chordwise location, x, from the leading edge of the foil[3].

$$\bar{y} = c_1 \bar{x}^{0.5} + c_2 \bar{x} + c_3 \bar{x}^{1.5} + c_4 \bar{x}^2 \tag{2.4}$$

where $\bar{x} = x/c$, $\bar{y} = y/c$ and

---

[3]Notice that a different coordinate system, (x, y) shown in Figure 2-8, is used in the numerical results as opposed to the coordinate system used in the experiment, (x, z) shown in Figure 2-1.
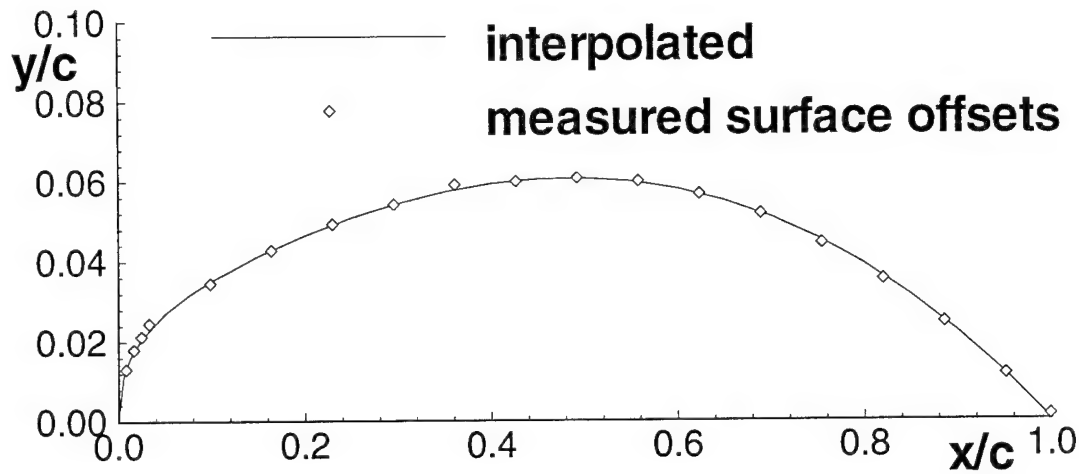
Figure 2-8: Plot of foil surface.

$$c_1 = 0.1787$$
$$c_2 = -0.3997$$
$$c_3 = 0.7611$$
$$c_4 = -0.5401$$

Figure 2-8 shows both the measured foil offsets and the interpolated points from equation (2.4). Notice that the interpolation scheme smoothed out the unevenness in the measured surface offsets.

The foil has the following dimensions:

- $c = 305\text{mm}$ (12in)

- $\rho_{LE}/c = 0.0160$

- $t_{max}/c = 0.120$ at $x/c = 0.485$

with c being the chord, ρ_{LE} being the leading edge radius, and t_{max} being the maximum thickness of the foil. The foil thickness, near the leading edge, increases as the square root of the chordwise location. In particular, the first term on the right hand side of equation (2.4) determines the value of ρ_{LE}, given by equation (2.5).

Table 2.3: Heavy Foil Coordinates

x/c	y/c	x/c	y/c
0.0000	0.0000	0.4000	0.0593
0.0050	0.0109	0.4500	0.0604
0.0075	0.0129	0.5000	0.0606
0.0125	0.0160	0.5500	0.0598
0.0250	0.0209	0.6000	0.0579
0.0500	0.0271	0.6500	0.0549
0.0750	0.0316	0.7000	0.0508
0.1000	0.0352	0.7500	0.0455
0.1500	0.0413	0.8000	0.0390
0.2000	0.0464	0.8500	0.0312
0.2500	0.0508	0.9000	0.0222
0.3000	0.0544	0.9500	0.0118
0.3500	0.0573	1.0000	0.0000

$$\rho_{LE} = c_1^2/2 \tag{2.5}$$

Table 2.3 lists the foil offsets of the "heavy" foil.

Chapter 3

CAV2D-BL: Partially-Cavitating Boundary Layer Solver

3.1 Formulation

3.1.1 Inviscid Cavitating Flow Theory

Assuming inviscid, irrotational, steady, uniform flow, in a field of infinite extent, the governing equation everywhere inside the fluid region is given by Laplace's equation:

$$\nabla^2\Phi = 0 \tag{3.1}$$

where Φ is the total velocity potential composed of the inflow potential, Φ_{in}, and the perturbation potential, ϕ. Thus, the perturbation potential is defined as:

$$\phi(x,y) = \Phi(x,y) - \Phi_{in}(x,y) \tag{3.2}$$

In order to uniquely determine ϕ, the following boundary conditions, shown in Figure 3-1 are imposed (Kinnas and Fine, 1990):

- On the **foil surface**, the following *kinematic boundary condition* is applied, which requires the fluid flow to be tangent to the surface of the foil. Therefore,
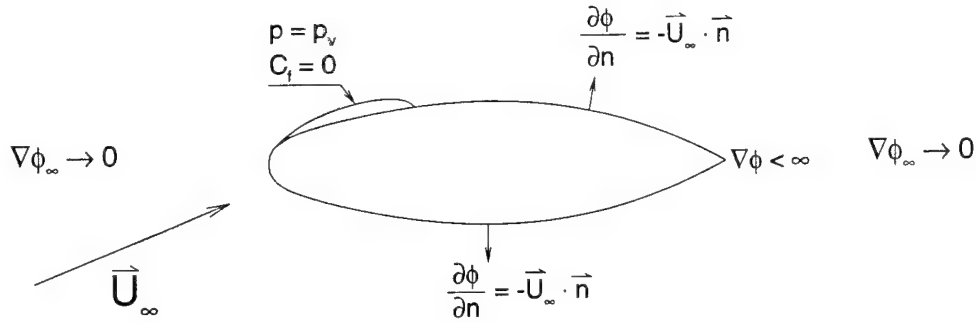
Figure 3-1: Hydrofoil with imposed boundary conditions.

$$\frac{\partial \phi}{\partial n} = -\boldsymbol{U}_\infty \cdot \boldsymbol{n} \tag{3.3}$$

where $\boldsymbol{n}$ is the surface unit normal vector.

- At **infinity** the perturbation velocities should go to zero.

$$\nabla \phi \to 0 \tag{3.4}$$

- The *Kutta condition* requires finite velocities at the **trailing edge** of the foil:

$$\nabla \phi < \infty \tag{3.5}$$

- The *dynamic boundary condition* specifies constant pressure **on the cavity**:

$$|\boldsymbol{q}_c| = U_\infty \sqrt{1 + \sigma} \tag{3.6}$$

- Near the **trailing edge of the cavity**, a *pressure recovery termination model* replaces equation (3.6):

$$|\boldsymbol{q}_{tr}| = U_\infty \sqrt{1 + \sigma}\,[1 - f(x)] \tag{3.7}$$

where $f(x)$ is an algebraic function defined in Kinnas and Fine (1990) and the cavitation number, σ, is defined as:

$$\sigma = \frac{p_\infty - p_v}{\frac{\rho}{2}U_\infty^2} \tag{3.8}$$

p_∞ is the pressure corresponding to a point in the free-stream and p_v is the cavity pressure (vapor pressure of water). The perturbation potential at a point P can be related to the potential on the foil surface and wake via Green's third identity:

$$\epsilon\pi\phi_P = \oint_{S_B} \left[\frac{\partial\phi}{\partial n}\ln R - \phi\frac{\partial\ln R}{\partial n} \right] ds - \oint_{S_W} \triangle\phi_W \frac{\partial\ln R}{\partial n}s \tag{3.9}$$

where ϕ is the perturbation potential on the foil, $\boldsymbol{n}$ is a unit vector normal to the foil surface, S_B is the foil and cavity surface, S_W is the trailing wake surface, and R is the distance between a field point, P, and the point of integration over the foil or wake surface. $\epsilon = 1$ when P is on the foil or wake surface and $\epsilon = 2$ otherwise.

In the case of fully-wetted (non-cavitating) flow, the foil and wake is discretized into $N + N_W$ panels as shown in Figure 3-5, where N is the number of panels on the foil surface and cavity and N_W is the number of panels on the trailing wake surface. The source and dipole strengths are assumed constant over each panel. On the foil surface, the source strengths, which are proportional to $\partial\phi/\partial n$, are given by the kinematic boundary condition, equation (3.3). On the cavity, the dipole strengths, which are proportional to ϕ, are given from integrating the dynamic boundary condition, equation (3.6). The discretized version of Green's theorem results in a system of linear equations from which the perturbation potential can be solved for each panel on the foil and cavity.

In finding the cavity shape, the cavity length and the point of detachment are both given. The cavity height is determined in an iterative manner until both the kinematic and dynamic boundary conditions are satisfied on the cavity (Kinnas and Fine, 1993).
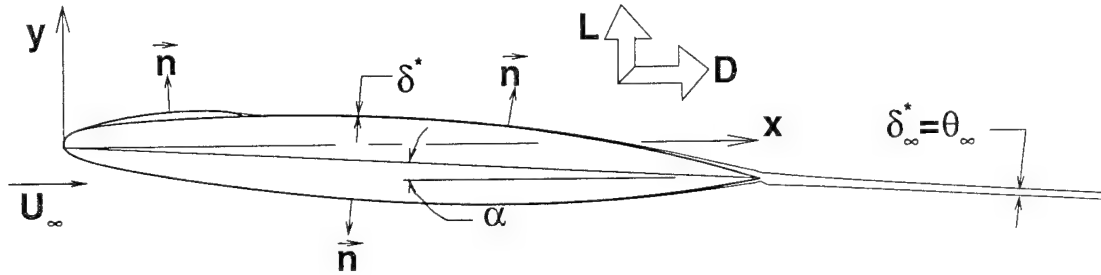
Figure 3-2: Hydrofoil with displaced body. Definition of main parameters. $\alpha = 3.5°$.

3.1.2 Boundary Layer Theory

Near the foil, viscous effects are confined in the boundary layer. To account for these effects, blowing sources, of strength $\hat{\sigma}$ are added to the foil surface.

$$\hat{\sigma} = \frac{d(U_e \delta^\star)}{ds} \tag{3.10}$$

where s is the arclength along the foil, U_e is the velocity at the edge of the boundary layer, and δ^* is the displacement thickness.[1] Figure 3-2 shows the definition of the main parameters used in viscous theory. Given an inviscid edge velocity distribution, the following boundary layer equations are solved (Drela, 1989).

$$\frac{d\theta}{ds} + (H+2)\frac{\theta}{U_e}\frac{dU_e}{ds} = \frac{C_f}{2} \tag{3.11}$$

$$\frac{\theta}{H^*}\frac{dH}{ds}\frac{dH^*}{dH} = \frac{2C_d}{H^*} - \frac{C_f}{2} + (H-1)\frac{\theta}{U_e}\frac{dU_e}{ds} \tag{3.12}$$

$$\frac{d\tilde{n}}{ds} = \frac{d\tilde{n}}{dRe_\theta}\frac{dRe_\theta}{ds} \tag{3.13}$$

---

[1]The displacement thickness is defined as the distance the streamlines are displaced due to the boundary layer: $\delta^* = \int_0^\infty (1 - u/U_e)\, dy$. For more information on this see Schlichting (1979).

$$\frac{\delta}{C_\tau}\frac{dC_\tau}{ds} = 5.6\left[C_{\tau_{EQ}}^{1/2} - C_\tau^{1/2}\right] + 2\delta \times \left\{\frac{4}{3\delta^\star}\left[\frac{C_f}{2} - \left(\frac{H_k - 1}{6.7H_k}\right)^2\right] - \frac{1}{U_e}\frac{dU_e}{ds}\right\} \qquad (3.14)$$

In the case of laminar flow, equations (3.11), (3.12), and (3.13) are solved for the quantities δ^*, θ, and $\tilde{n}$. For turbulent flow, equations (3.11), (3.12), and (3.14) are solved for the quantities δ^*, θ, and C_τ.

The inviscid flow is coupled with the viscous flow via the wall transpiration model. This model gives the edge velocity at each panel in terms of the inviscid edge velocity and a mass defect term, $m = U_e\delta^*$.[2]

$$U_e = U_e^{inv} + \mathcal{E}\{U_e\delta^\star\} \qquad (3.15)$$

The boundary layer equations are solved first with the edge velocity distribution given from inviscid theory. Once δ^* is found, U_e is updated via equation (3.15). The boundary layer equations are then solved again. This process continues until convergence is achieved.

This method is extended to partially-cavitating hydrofoils by ignoring the two-phase flow near the cavity surface, treating the fluid/vapor interface as constant-pressure, free streamlines, and forcing C_f to zero on the cavity surface (Villeneuve, 1993; Kinnas et al., 1994). The boundary layer equations are integrated over the non-linear cavity and foil surface.

3.2 Numerical Implementation

The details of the numerics used to model viscous flow around a partially-cavitating hydrofoil are given in the following three steps. Figure 3-3 illustrates the different stages involved in the calculation.

---

[2]$\mathcal{E}$ is a geometry-dependent operator, the discretized version of which is given in Section 3.2.2 (Hufford, 1990; Drela, 1989).

3.2.1 Step 1: Calculate the cavity height (PCPAN)

Given a hydrofoil geometry, the first step is to calculate the cavity height. This is accomplished by running PCPAN, the partially-cavitating panel method, which solves for the inviscid cavity flow in non-linear theory (Kinnas and Fine, 1990).

In PCPAN, the user must specify the cavity leading and trailing edge. The method solves the inviscid flow in an iterative manner, by updating the cavity height until both the kinematic boundary condition and dynamic boundary condition are satisfied on the cavity. PCPAN gives as its result the cavity ordinates and the cavitation number.

3.2.2 Step 2: Calculate inviscid edge velocity on compound foil (CAV2D-BL)

The next step involves using the loci of points which envelope both the cavity and foil surface, as shown in Figure 3-3, as a new foil: the "compound" foil.

Discretize Green's third identity, equation (3.9), into N panels to get (Hufford, 1990):

$$\pi\phi_i = \sum_{j=1}^{N} S_{ij}^{CF}\frac{\partial\phi_j}{\partial n} - \sum_{j=1}^{N} D_{ij}\phi_j - \Delta\phi_w W_i \tag{3.16}$$

where

$$
\begin{aligned}
D_{ij} &= \int_{S_j^{CF}} \frac{\partial\ln R}{\partial n}d\boldsymbol{s} \\
S_{ij} &= \int_{S_j^{CF}} \ln R d\boldsymbol{s} \\
W_i &= \int_{S_w} \frac{\partial\ln R}{\partial n}d\boldsymbol{s}
\end{aligned}
$$

$$\tag{3.17}$$

D_{ij} is an influence function on i due to the jth dipole; S_{ij} is an influence function on i due to the jth source. W_{ij} is the contribution of source strength from the wake and S^{CF} is the surface bounded by the union of the foil and cavity surface. The Kutta condition, equation (3.5), reduces to Morino's condition:
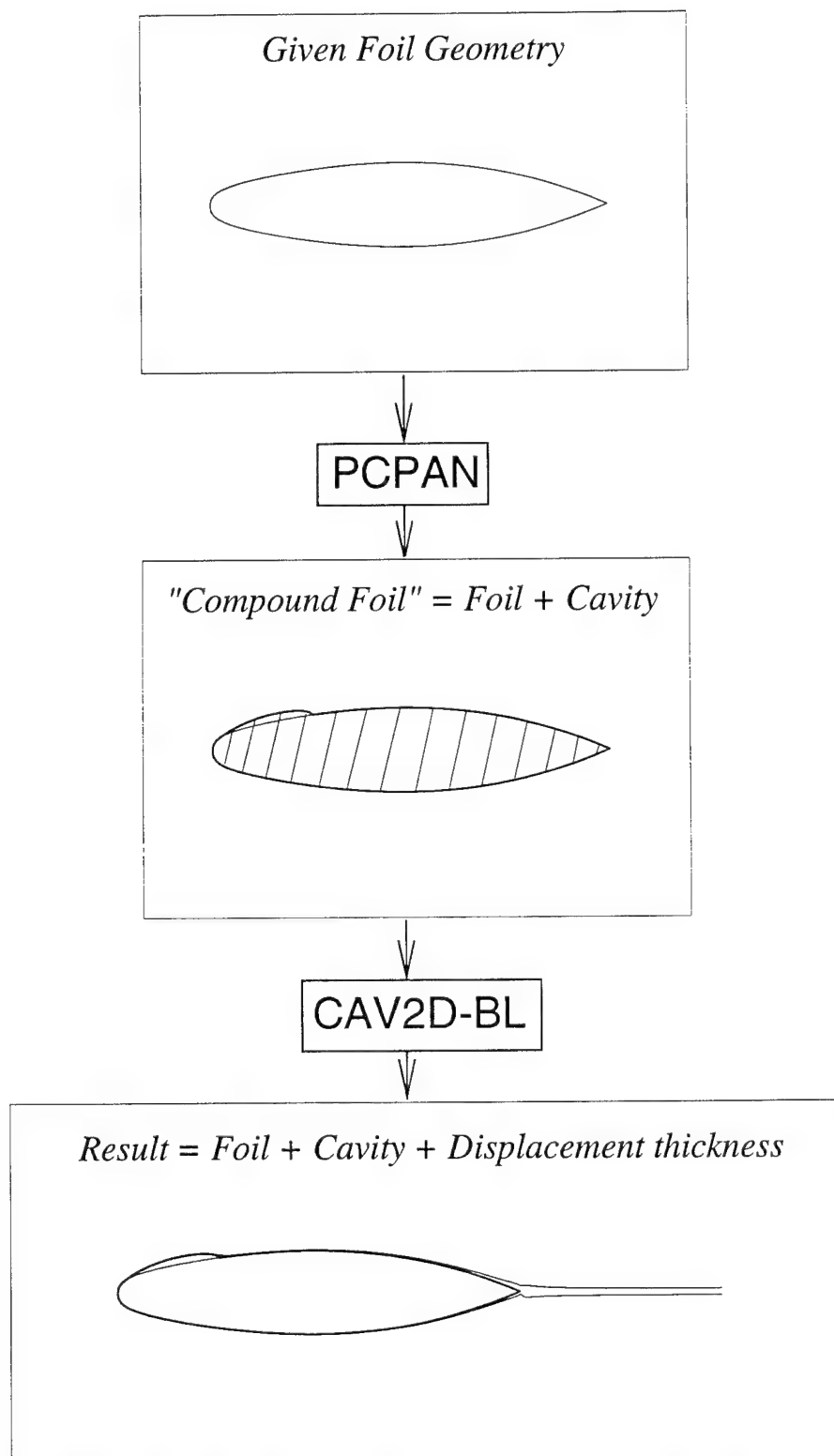
Figure 3-3: Flow of calculation method for solving viscous flow on a 2D partially-cavitating hydrofoil.

$$\Delta\phi_w = \phi_N - \phi_1 \tag{3.18}$$

Thus, equation (3.16) can be represented by the following set of algebraic equations:

$$
\begin{bmatrix}
\pi & D_{12} & \cdots & D_{1N} \\
D_{21} & \ddots & & \vdots \\
\vdots & & \ddots & D_{N-1,N} \\
D_{N1} & D_{N2} & \cdots & \pi
\end{bmatrix}
\begin{bmatrix}
\phi_1 \\
\vdots \\
\vdots \\
\phi_N
\end{bmatrix}
+
\begin{bmatrix}
-W_1 & 0 & \cdots & 0 & W_1 \\
-W_2 & 0 & \cdots & 0 & W_2 \\
\vdots & \vdots & & \vdots & \vdots \\
-W_N & 0 & \cdots & 0 & W_N
\end{bmatrix}
\begin{bmatrix}
\phi_1 \\
\vdots \\
\vdots \\
\phi_N
\end{bmatrix}
$$

$$
=
\begin{bmatrix}
0 & S_{12} & \cdots & S_{1N} \\
S_{21} & \ddots & & \vdots \\
\vdots & & \ddots & S_{N-1,N} \\
S_{N1} & S_{N2} & \cdots & 0
\end{bmatrix}
\tag{3.19}
$$

Let

$$
A_{ij} =
\begin{bmatrix}
\pi & D_{12} & \cdots & D_{1N} \\
D_{21} & \ddots & & \vdots \\
\vdots & & \ddots & D_{N-1,N} \\
D_{N1} & D_{N2} & \cdots & \pi
\end{bmatrix}
+
\begin{bmatrix}
-W_1 & 0 & \cdots & 0 & W_1 \\
-W_2 & 0 & \cdots & 0 & W_2 \\
\vdots & \vdots & & \vdots & \vdots \\
-W_N & 0 & \cdots & 0 & W_N
\end{bmatrix}
\tag{3.20}
$$

and equation (3.19) simplifies to:

$$A_{ij}\phi_j = S_{ij}\frac{\partial\phi_j}{\partial n} \tag{3.21}$$

Therefore,

$$\left[\phi^{inv}\right] = [A]^{-1}[S]\left[\frac{\partial\phi}{\partial n}\right] \tag{3.22}$$

and, from equation (3.2), the total *inviscid* potential becomes:

$$\left[\Phi^{inv}\right] = [\Phi_{in}] + \left[\phi^{inv}\right] \tag{3.23}$$

The *inviscid* edge velocity can then be determined by numerical differentiation of equation

(3.23) as such:

$$U_e^{inv} = \frac{d\Phi^{inv}}{ds} \approx \frac{[\Phi^{inv}]_{i+1} - [\Phi^{inv}]_i}{s_{i+1} - s_i} \tag{3.24}$$

3.2.3 Step 3: Solve the boundary layer equations on compound foil (CAV2D-BL)

The inviscid edge velocity, U_e^{inv}, is used as the 0-th iteration for the viscous solution. Equation (3.35) is solved along with the boundary layer equations, equations (3.11), (3.12), and (3.13) for laminar flow and equations (3.11), (3.12), and (3.14) for turbulent flow. This closed set of coupled non-linear equations can then be solved using Newton's method.

$$[J_{ij}] [\delta \mathcal{X}]^k = \{-R_i\}^k \quad 1 \le i \le N + N_W \tag{3.25}$$

where

$$\mathcal{X}_j^k = \left\{ \begin{array}{c} \theta_j \\ m_j \\ \tilde{n} \ or \ C_{\tau_j} \end{array} \right\}^k \tag{3.26}$$

and J_{ij} is the viscous Jacobian given by:

$$J_{ij}^k = \frac{\partial R_i^k}{\partial \mathcal{X}_j} \tag{3.27}$$

R_i is the residual, the difference between the edge velocities of the kth iteration and the $k - 1$ iteration:

$$R_i^k = U_{e_i}^k - U_{e_i}^{k-1} \tag{3.28}$$

If the residual is below the user-specified value (EPS1), the iterations will stop. Otherwise, $\mathcal{X}$ is updated as follows:

$$[\mathcal{X}]^{k+1} = [\mathcal{X}]^k + [\delta\mathcal{X}]^k \tag{3.29}$$

The algorithm checks for excessive changes and underrelaxes the residual if it is higher than the accumulated root-mean-square change.

3.2.4   Step 4: Update the edge velocity (CAV2D-BL)

The effects of the boundary layer are modeled by adding blowing sources to the surface of the "compound" foil. In doing this, equation (3.16) becomes:

$$\sum_{j=1}^{N} A_{ij}\phi_j = \sum_{j=1}^{N} S_{ij}\frac{\partial\phi_j}{\partial n} + \sum_{j=1}^{N+N_w} B_{ij}\hat{\sigma}_j \tag{3.30}$$

where $\hat{\sigma}$ is the blowing source strength given in equation (3.10) and B_{ij} is an influence function, similar to S_{ij}, representing the influence of i on the jth source and is given by:

$$B_{ij} = \int_{S_j^{CF}} \ln R ds \tag{3.31}$$

In matrix form, equation (3.30), becomes:

$$[A][\phi] = [S]\left[\frac{\partial\phi}{\partial n}\right] + [B][\hat{\sigma}] \tag{3.32}$$

By multiplying the system by the inverse A matrix, and using equation (3.22):

$$[\phi] = \left[\phi^{inv}\right] + [A]^{-1}[B][\hat{\sigma}] \tag{3.33}$$

From equation (3.2), the total potential Φ can be determined by:

$$[\Phi] = \left[\Phi^{inv}\right] + [A]^{-1}[B][\hat{\sigma}] \tag{3.34}$$
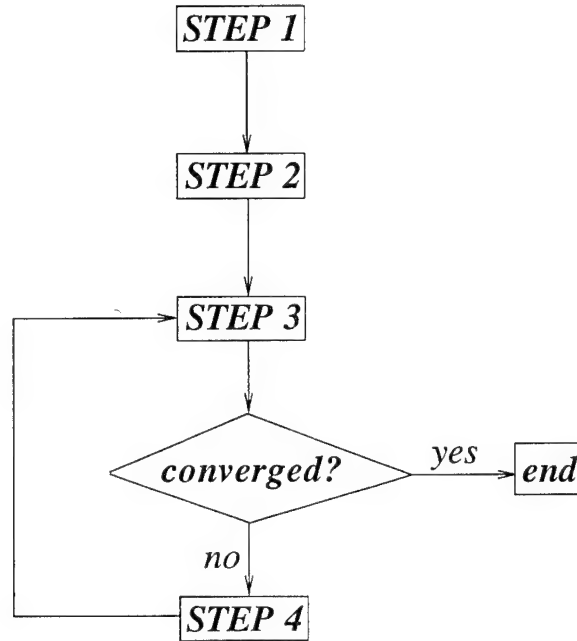
Figure 3-4: Flow of steps involved in coupled cavity analysis/boundary layer method.

Numerical differentiation of equation (3.34) with respect to the arclength s gives the edge velocity at the panel nodes:

$$U_e^{k+1} = U_e^{inv} + \mathcal{E}\{U_e^k \delta^{*^k}\} \approx \frac{\Phi_{i+1} - \Phi_i}{s_{i+1} - s_i} \qquad (3.35)$$

where

$$\mathcal{E} = \frac{d}{ds}[A]^{-1}[B]\frac{d}{ds} \qquad (3.36)$$

Figure 3-4 is a simple illustration of the flow from Steps 1 to 4.

3.2.5 Indexing of the panels

In coupling PCPAN and CAV2D-BL, careful steps must be taken in defining the regions where the boundary conditions are to be applied. The systems used in indexing the panels are defined differently in PCPAN than in CAV2D-BL as shown in Figure 3-5. In PCPAN, the panels are numbered clockwise, where the first index is at the trailing edge

of the foil.

On the other hand, CAV2D-BL first searches for the stagnation point. The location of the stagnation point is placed in the center of the panel. On the suction side, the first index is the half-panel above the stagnation point; subsequent numbers follow clockwise. On the pressure side, the first index is the half-panel below the stagnation point; subsequent numbers follow counter-clockwise, as shown in Figure 3-5. In CAV2D-BL, the suction side of the foil is called *side 1 (is=1)* and the pressure side of the foil is *side 2 (is=2)*.

The following quantities are used to specify the cavity location:

- NLE - number of panels between leading edge and cavity detachment (PCPAN)

- $LCAV$ - cavity trailing edge node number (PCPAN)

- IBL - panel number index (CAV2D-BL)

- $ICLES$ - cavity leading edge panel number, suction side (CAV2D-BL)

- $ICLEP$ - cavity leading edge panel number, pressure side (CAV2D-BL)

- $ICTE$ - cavity trailing edge panel number (CAV2D-BL)

These values are used to specify panels on which C_f must go to zero. Notice that the values given from PCPAN refer to the panel nodes while the values from CAV2D-BL refer to the actual panel and are related to NLE and $LCAV$ given from PCPAN in the following manner.

The indices in PCPAN are related to those in CAV2D-BL by:

$$
\begin{aligned}
IBL &= j \\
ICLES &= NLE + 1 \\
ICTE &= LCAV - N/2 + 1
\end{aligned}
\tag{3.37}
$$
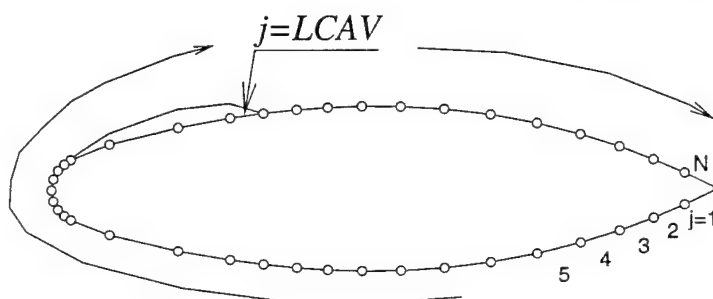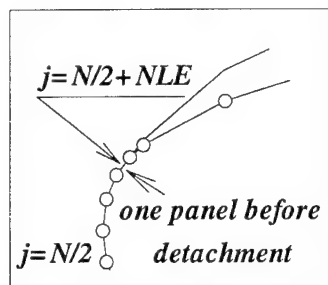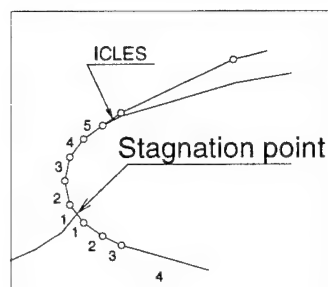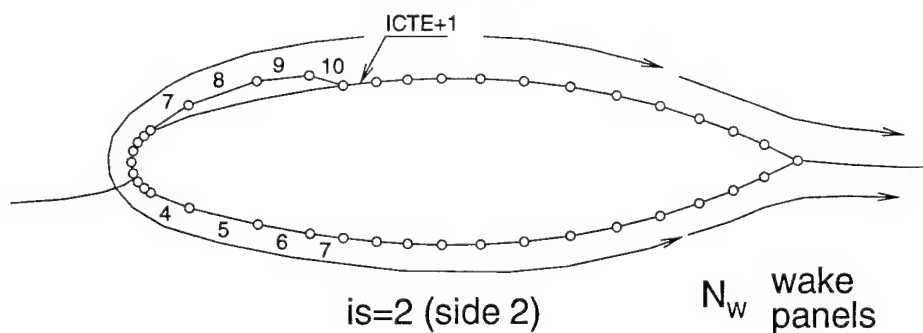
Figure 3-5: Index arrangement for PCPAN, SCPAN, and CAV2D-BL. Indices correspond to panel numbers (as opposed to node number).

For side 1:

$$C_f = \begin{cases} nonzero & 1 \leq j < ICLES \\ 0 & ICLES \leq j \leq ICTE \\ nonzero & ICTE < j \leq N/2 + NSTAG \\ 0 & j > N/2 + NSTAG \end{cases} \qquad (3.38)$$

For side 2:

$$C_f = \begin{cases} nonzero & 1 \leq j < N/2 - NSTAG \\ 0 & j > N/2 - NSTAG \end{cases} \qquad (3.39)$$

where N is the number of panels representing the compound foil and cavity surface, NF is the number of panels on the pressure side of the foil surface, and $NSTAG$ is the number of panels shifted from the centerline of the leading edge.

3.3   Analytical Forces

The lift coefficient, corresponding to the coordinate system shown in Figure 3-2, is computed by taking the vertical component of the pressures integrated over the entire foil surface. This expression is given by:

$$C_L = \oint C_P^{vis} n_y ds \qquad (3.40)$$

where C_P^{vis} are the "viscous" pressures, or the pressures computed on the displaced foil surface as shown in Figure 3-7, and n_y is the y-component of the unit normal vector.

The drag is composed of an inviscid and viscid contribution as such:

$$C_D = C_D^{inv} + C_D^{vis} \qquad (3.41)$$

The inviscid term, C_D^{inv}, is attributed to the drag of the cavity and is given by:

$$C_D^{inv} = \oint C_P^{inv} n_x ds \qquad (3.42)$$

where C_P^{inv} are the *inviscid* pressures shown in Figure 3-7 and n_x is the x-component of the unit normal vector. Cavity drag can be explained by attenuation of pressure near the trailing edge of the cavity, accurately modeled by the pressure recovery termination model, equation (3.7).

C_D^{vis} is the viscous drag term and is given by the "far-wake" approximation as (Drela, 1989):

$$C_D^{vis} = \frac{2\theta_\infty}{c} \tag{3.43}$$

where θ_∞ is the momentum thickness computed far downstream,[3] as shown in Figure 3-2.

3.4 Convergence Characteristics

For 200 panels on a HP 9000/735 with a risc chip, the coupled PCPAN/CAV2D-BL took less than two minutes.

The convergence of the results of the viscous cavity solution with number of panels is shown in Figure 3-6. The inviscid solution converges much quicker than the viscous solution. The viscous cavitation number, σ^v, is not constant over the extent of the cavity, evident in Figure 3-7.

3.5 Results

An example of results from this method is shown in Figure 3-7. This shows the case of a 20% cavity at 3.5 degrees with the boundary displacement thickness superimposed on the foil and wake surface. Shown at the bottom of Figure 3-7 are the inviscid and viscous pressure distributions on the foil. Notice that viscosity largely affects the cavitation number. In addition, the pressure is not constant over the entire extent of the cavity anymore. From comparing the areas under the viscous and inviscid pressure distributions, we can also infer that the lift coefficient decreases due to the viscous effects.

---

[3]Five chord lengths aft of the trailing edge.
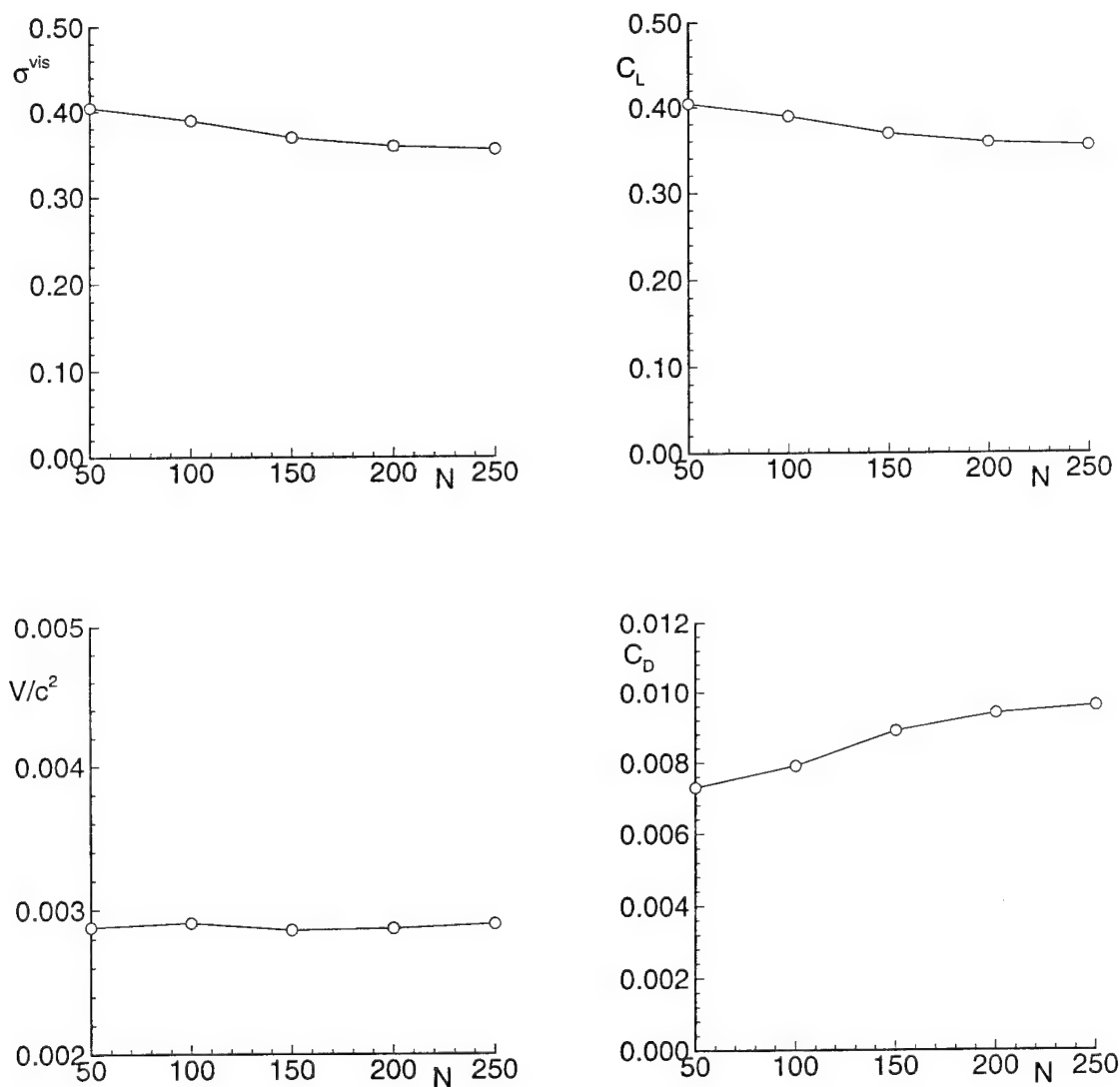
Figure 3-6: Convergence characteristics of viscous cavity solution for C_L, C_D, σ^{vis}, and V/c^2 (cavity volume). $\alpha = 3.5^o$, $l/c = 0.30$, $N =$ the number of panels on the foil and cavity.
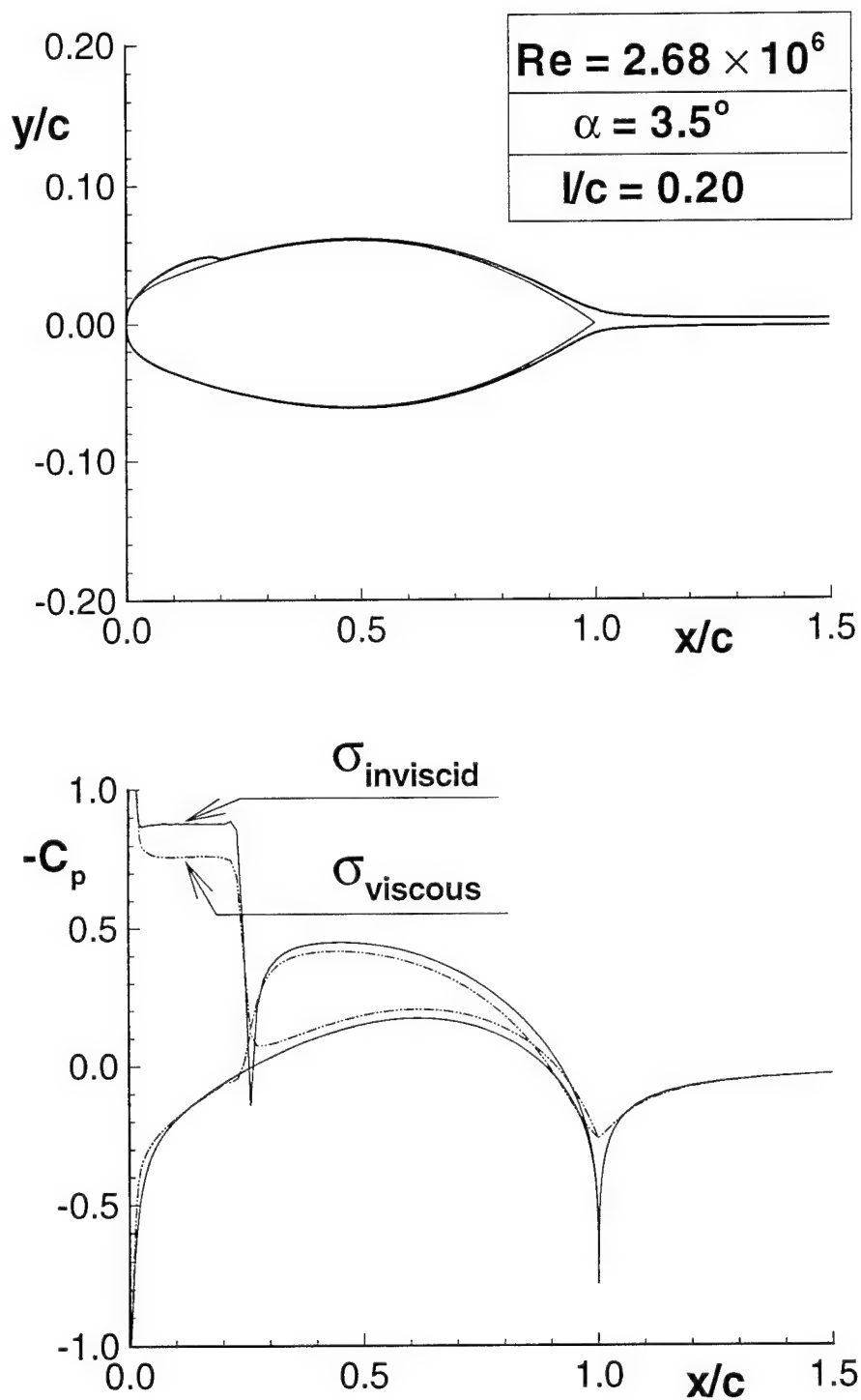
Figure 3-7: Above: Present method's prediction of heavy foil with viscous effects. Below: Viscous and inviscid pressure distribution on foil.

Table 3.1: Cavitation number and cavity volume from the analysis method, using both predicted and experimentally observed cavity detachment as input.

detachment type	l_D/c	σ	V/c^2
experimental	0.02	1.007	0.00176
predicted	0.022	0.991	0.00165

Figure 3-8 shows δ^*, θ, and H for the hydrofoil shown in Figure 3-7. Notice on the suction side that there is a sharp peak in the displacement thickness. Also, ahead of the cavity, the shape factor is above four, indicating laminar separation.

3.6 Cavity Detachment Point

By adjusting the cavity detachment point, it was found that laminar separation occurred just ahead of the experimentally observed cavity detachment. This is in accordance with the cavity detachment criterion of Franc and Michel (1985). Figure 3-9 shows the current method can be used, in systematic manner, to determine the cavity detachment. In this procedure, one initially inputs the leading edge as the cavity detachment then increases the cavity detachment location until the shape factor, H, is four just before the specified detachment. Table 3.1 shows the differences in cavitation number and cavity volume using: 1) the experimentally observed cavity detachment location as an input to CAV2D-BL and 2) the criterion of Franc and Michel.

3.7 Effects of Tunnel Walls

The tunnel walls are accurately modeled, in both the inviscid cavity solution and the boundary layer solver, by providing an adequate number of images of the sources and dipoles (which represent the foil, cavity, and the boundary layer displacement thickness). The analysis method was performed with and without the effect of tunnel walls, for *fixed* cavitation number, to investigate the effect of tunnel blockage on the cavity solution.
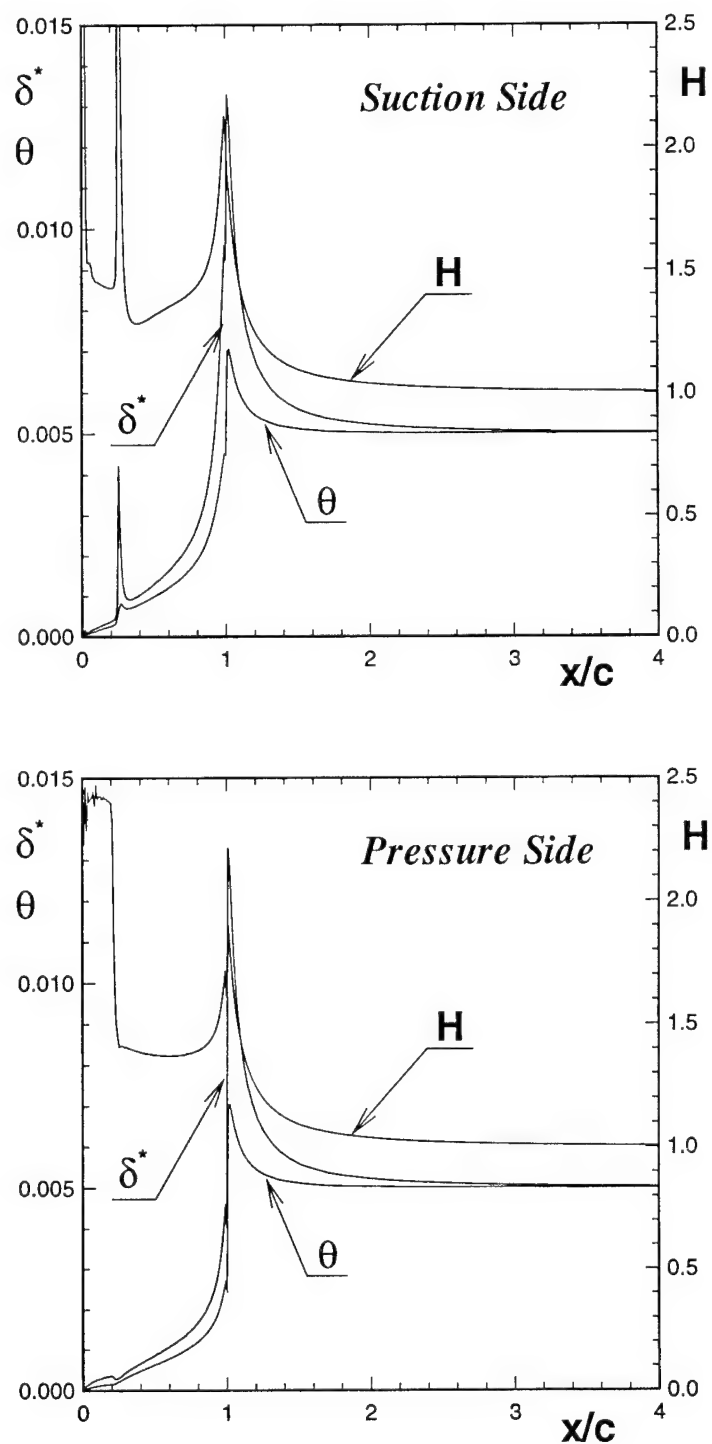
Figure 3-8: Displacement thickness, momentum thickness, and shape factor along suction and pressure sides of hydrofoil. $\alpha = 3.5^{\circ}, l/c = 0.20$
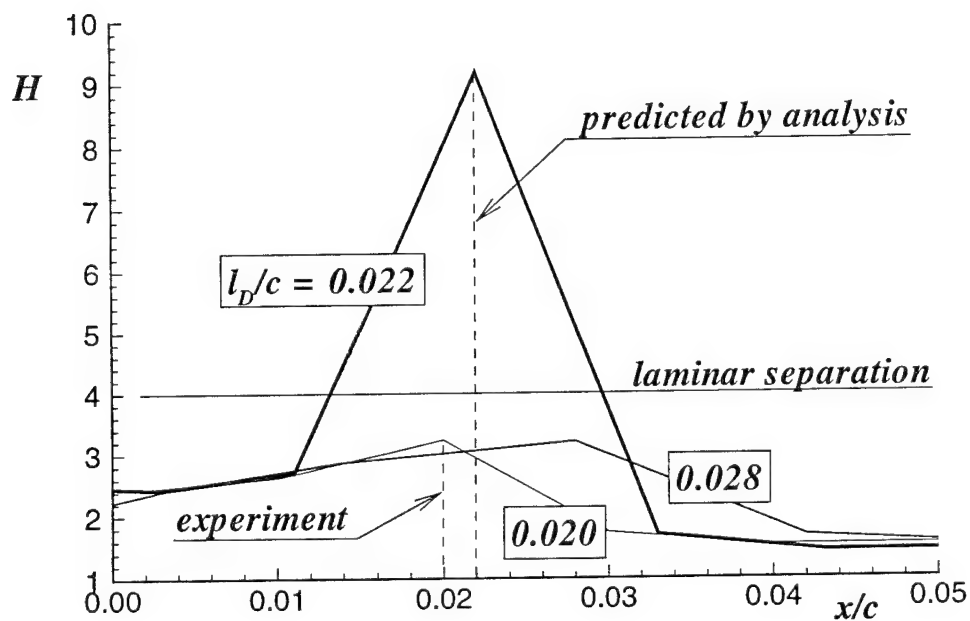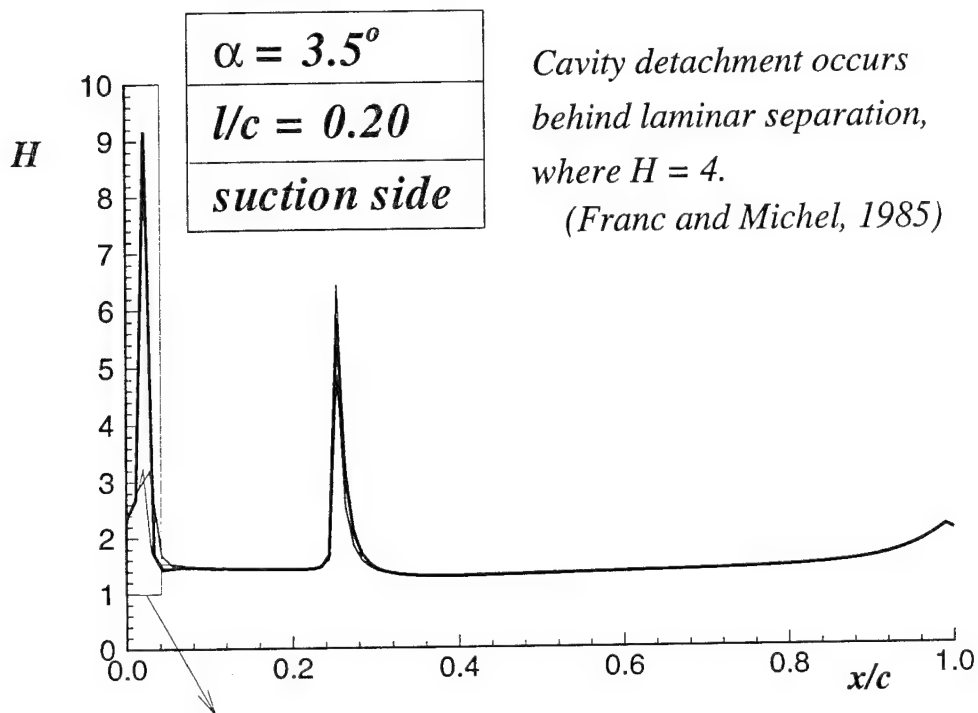
Figure 3-9: Shape factor along suction side of foil showing the method used to predict cavity detachment. $l/c = 0.20$, $\alpha = 3.5°$.
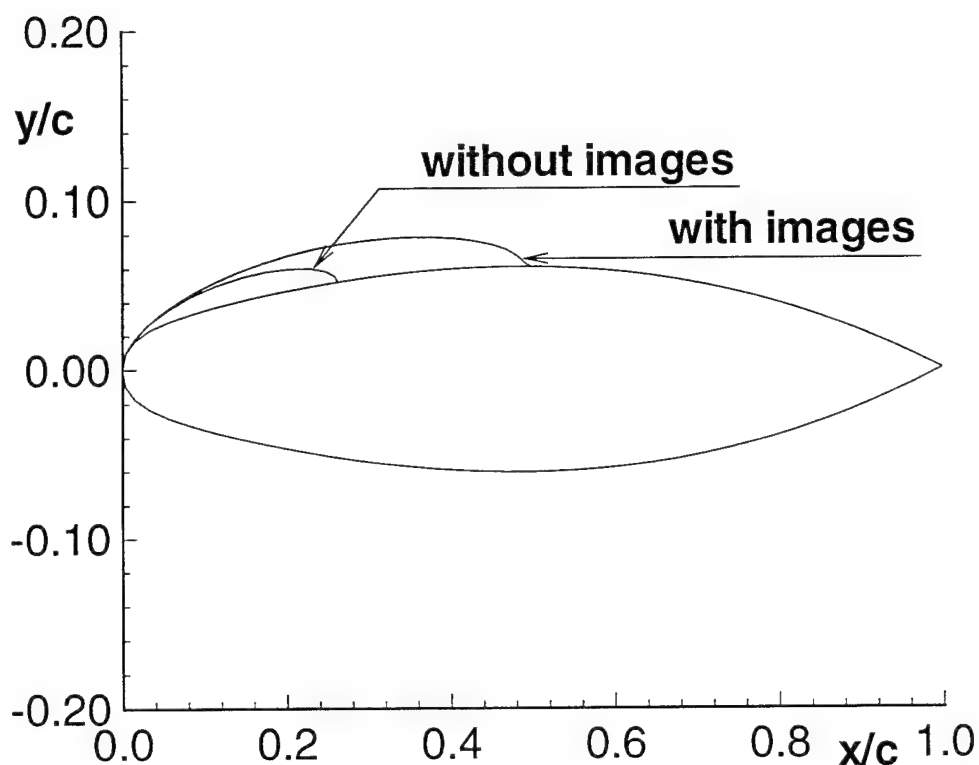
Figure 3-10: Foil geometry and cavity shape showing the effect of tunnel walls. $\sigma=0.86$

The results of this study, shown in Figure 3-10, yield a drastic difference, of nearly fifty percent in cavity length. Thus, experiments performed in the water tunnel are expected to produce much larger cavities than they would if they were in the "real world", or not constricted by the tunnel walls. This discrepancy *must* be accounted for whenever testing is being conducted in the water tunnel.

Maixner (1977) investigated the influence of wall effects on the force and moment coefficients of a super-cavitating hydrofoil. He results did not show a marked increase in wall effects on force and moment coefficients for lower angles of attack. He noted the most pronounced differences, between bounded and unbounded flow, were on the cavity and in the wake. Baker (1972) concluded that the effects of tunnel blockage are negligible for tunnel height-to-foil chord ratios (H/c) greater than ten.

Chapter 4

CAV2D-BL: Super-Cavitating Boundary Layer Solver

4.1 Formulation & Numerical Implementation

4.1.1 Step 1: Calculate cavity height (SCPAN)

The formulation of the super-cavitating hydrofoil is very similar to the that of partial-cavitation, given in Chapter 3. Figure 4-1 shows a discretized version of a super-cavitating foil and a definition of the main parameters.

As a first iteration for the non-linear solution, SCPAN uses the cavity shape from the linear solution. The linear solution is obtained by applying a source and vorticity formulation.

In a transition region at the trailing edge of the cavity, an end parabola model (as shown in Figure 4-2) replaces the cavity shape. This model serves to accurately represent the actual pressure attenuation as evidenced in experiments (Meijer, 1959). The shape of the end parabola is given by the linear solution. Its vertical position is determined iteratively until the kinematic boundary condition is satisfied on its surface.

Over the cavity surface, not including the transition region, the dynamic boundary condition is applied. In the transition region, the kinematic boundary condition is applied. The cavity shape is updated iteratively until the kinematic boundary condition is

56
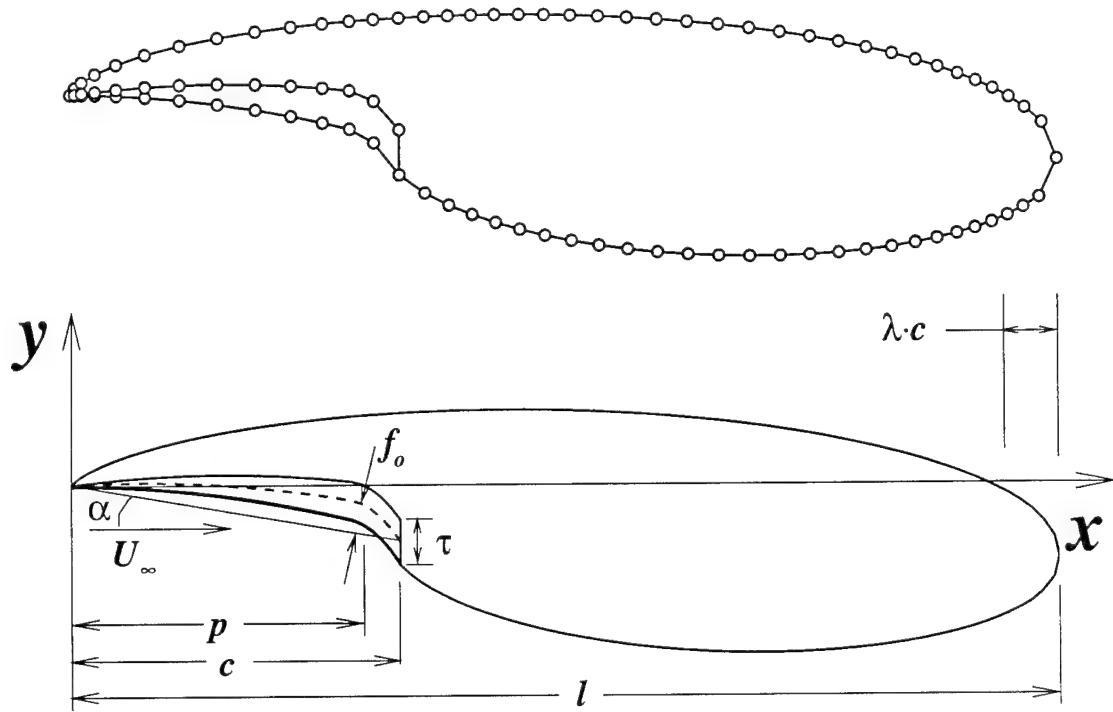
Figure 4-1: Super-cavitating hydrofoil in inviscid non-linear theory. Definition of main parameters. Panel arrangement on the cavity and foil shown for $N = 80$.
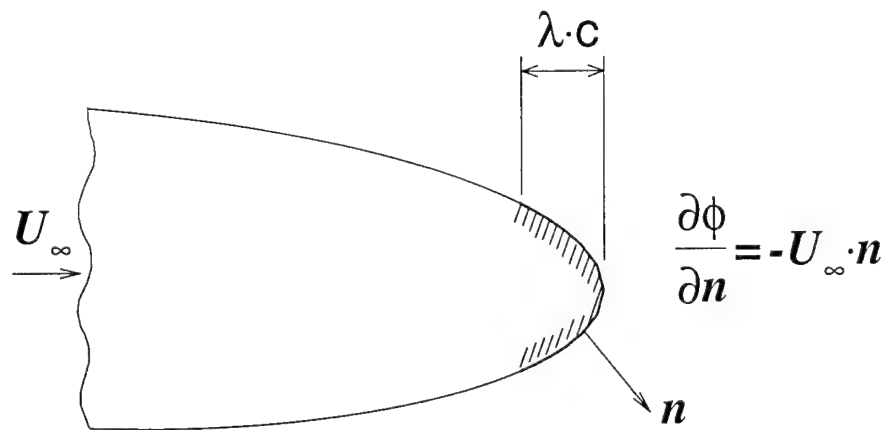
Figure 4-2: The super-cavitating end parabola model where the kinematic boundary condition is applied.
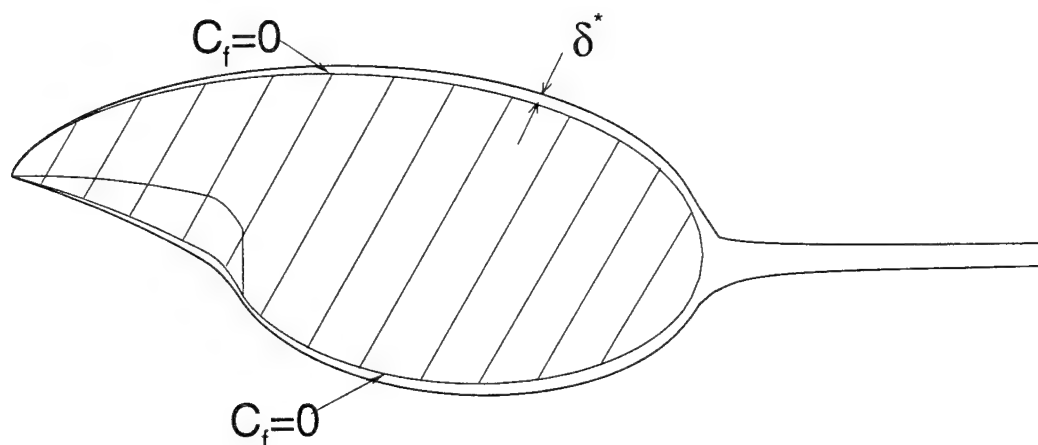
Figure 4-3: Super-cavitating hydrofoil with its boundary displacement thickness.

satisfied over the entire cavity extent.

4.1.2 Steps 2 & 3: Solve viscous flow around "compound" foil (CAV2D-BL)

Once the cavity height is known, the boundary conditions are applied on the "compound" foil, the boundary of the union of the cavity and foil surface, as shown in Figure 4-3. The "compound" foil must be *scaled* to unity and run at *zero* angle of attack. Also, in order to achieve convergence of the viscous cavity solution, the boundary layer solver's transition location searching routine is automatically turned off. Hence, for the viscous super-cavity solution, the user must specify the transition location.

4.2 Indexing of the panels

When solving the boundary layer equations, blowing sources are added to surface of the "compound" foil. The requirement that the boundary layer grows as a free-shear layer is met by forcing C_f to zero on the following panels:

- For side 1 ($is=1$):

$$C_f = 0 \quad j > 0 \tag{4.1}$$

- For side 2 ($is=2$):

$$C_f = \left\{ \begin{array}{ll} nonzero & j < ICLEP \\ 0 & j \geq ICLEP \end{array} \right\} \tag{4.2}$$

- where SCPAN is related to CAV2D-BL by:

$$
\begin{aligned}
ICTE &= N/2 + 1 \\
ICLES &= 0 \\
ICLEP &= NF + 1
\end{aligned}
\tag{4.3}
$$

and NF is the number of panels representing the pressure side of the foil surface

4.3 Results

The present method is applied to a super-cavitating foil with NACA 4-digit camber distribution and linear thickness form. Figure 4-4 shows the resulting nonlinear cavity shape and displacement thickness along the foil for a Reynolds number of 2×10^7. Notice that viscosity has little effect on the pressure distribution in Figure 4-4. Also shown in Figure 4-4 is the friction coefficient on the pressure side of foil and cavity, which is forced to zero aft of the trailing edge of the foil.

Figure 4-5 shows lift and drag characteristics for various cavitation numbers. It is evident in this figure that viscosity has a negligible effect on the lift. As the cavitation number increases, the viscous lift increases with respect to the inviscid lift. The reason for this is that the displacement thickness grows with increasing cavitation number, changing the effective angle of attack of the "compound" foil. The difference in drag coefficients, between inviscid and viscous flow, is much more pronounced, as shown in Figure 4-5.
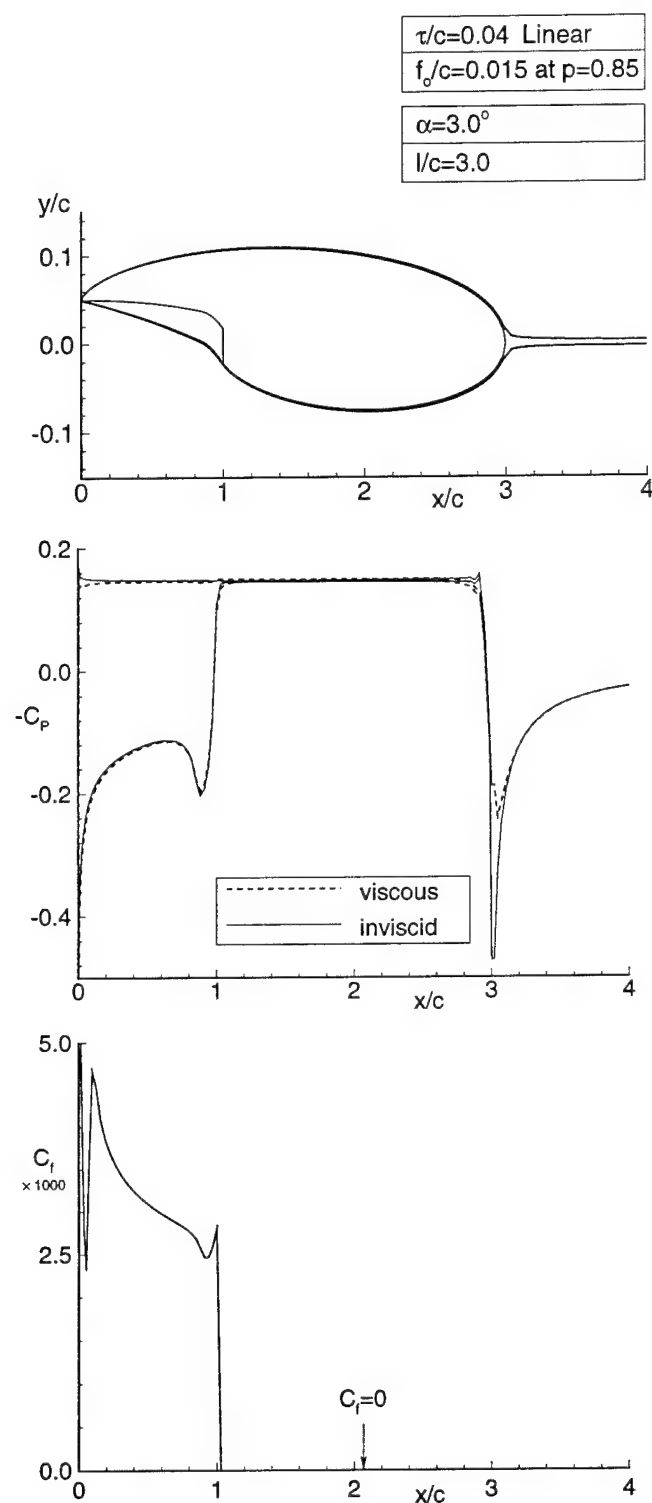
Figure 4-4: Super-cavitating hydrofoil in inviscid and viscous flow at $Re = 2 \times 10^7$. Cavity shape and boundary layer displacement thickness (top); pressure distributions (middle); and friction coefficient on the pressure side of the foil and cavity (bottom). All predicted by the present method.

Table 4.1: Convergence of viscous cavity solution (σ, V/c^2, C_L and C_D) with number of panels. Super-cavitating hydrofoil; $\tau/c = 0.045$, $f_o/c = 0.015$, $p = 0.85$, $\alpha = 3°$.

N	σ	V/c^2	C_L	C_D
100	0.145	0.365	0.282	0.0219
160	0.146	0.364	0.287	0.0223
200	0.146	0.363	0.292	0.0231

This difference is largely attributed to the frictional drag on the pressure side of the foil.

Figure 4-5 can be used to determine an "equivalent" cavity length which, if run under inviscid flow, would produce the same lift and cavity volume as the viscous cavity solution. Notice that the inviscid cavity solution underpredicts the cavity length for given C_L and σ. This can be reasoned by intuition in the following way: the angle of attack in viscous flow would have to be increased to produce the larger cavity that inviscid flow predicts; therefore, if the same angle of attack were used in both inviscid and viscous theory, the inviscid solution must produce a smaller cavity. Different cavity lengths for σ and α, are shown in Kinnas et al (1994) for inviscid flow and various Reynolds numbers. The "equivalent" σ concept can be applied to three dimensional geometries in a strip-wise sense. This is addressed much more extensively in Section 6.1.

Table 4.1 shows the convergence characteristics of the viscous super-cavitating solution for increasing panels numbers.
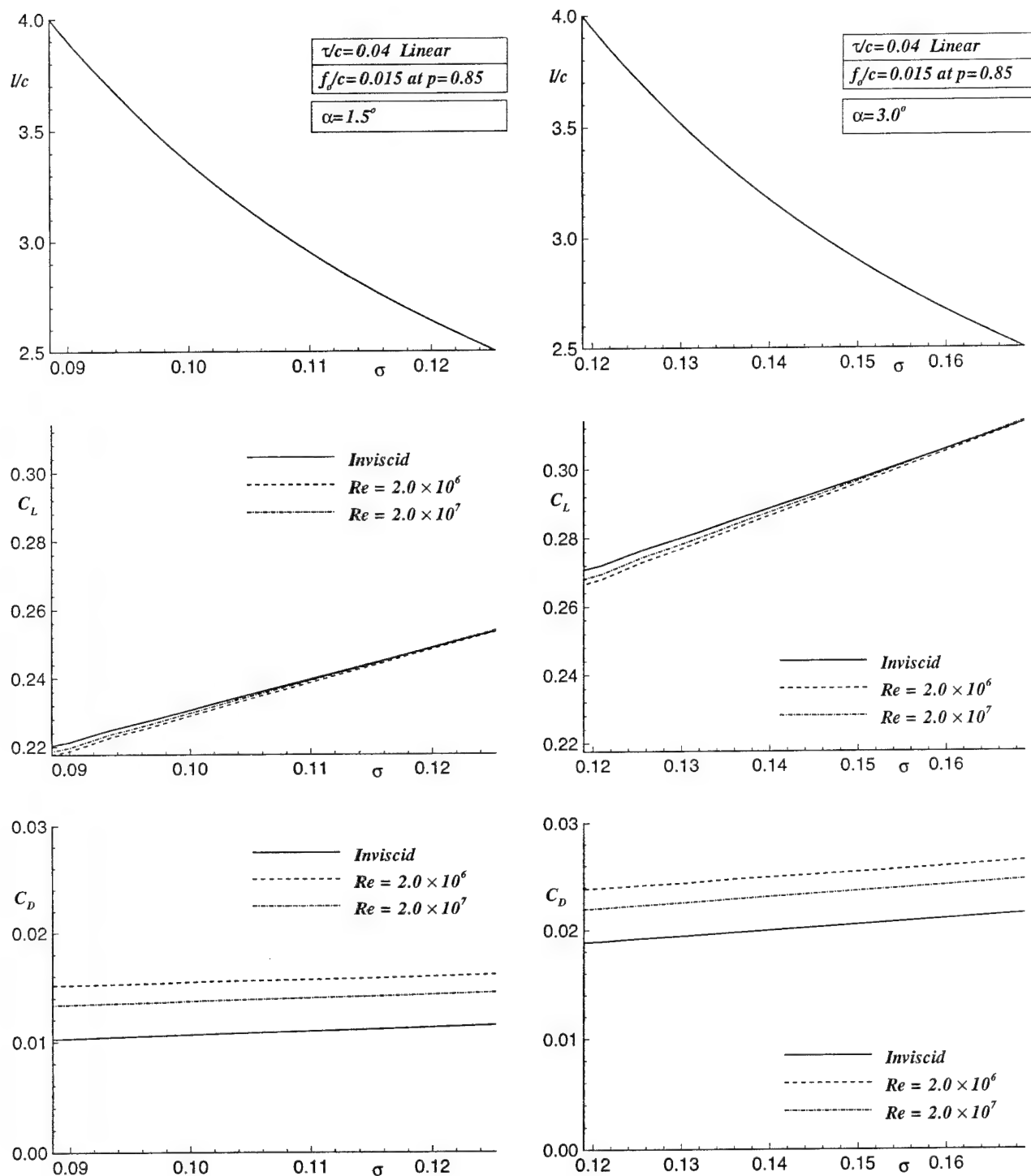
Figure 4-5: Cavity length, lift and drag coefficient versus cavitation number for a super-cavitating hydrofoil at $\alpha = 1.5°$ (left) and $\alpha = 3.0°$ (right), in inviscid and viscous flow; predicted by the present method.

Chapter 5

Experimental Versus Numerical Results: Phases II & III

This section contains experimental versus numerical comparisons, from Phases I and II of the experiment, for the quantities: velocities along contour surrounding the hydrofoil, velocities in boundary layer region, velocities near cavity surface, pressure measurements, and forces acting on the hydrofoil. Correlations between experiment and theory were also made with the data from Phase I of the experiment; they are given in Appendix D.

The angles of attack shown in the figures of this section may be confusing. With each reinstallation of the foil, the angle of attack changed slightly. All of the boundary layer measurements and measurements along the rectangular contour [1] were performed in Phase II of the experiment, where the angle of attack was 3.5°. All of the pressure measurements and velocity measurements near the cavity surface were performed in the third phase of the experiment, where the angle of attack was 3.25°. Refer to Table 2.1 for the details of each phase of the experiment.

The underlying intention for these comparisons is to be extremely systematic in correlating the analytical results with the experimental data. The comparisons between experiment and theory, in the case of cavitating flow, are based on the assumption that

---

[1] Except for the fully-wetted case, which was performed in Phase III. This measurement was performed again in Phase III because the free-stream velocity for the fully-wetted case in Phase II was inaccurately recorded.

Table 5.1: Comparison of lift and drag coefficients between experiment and theory. $\alpha = 3.25°$ in fully-wetted flow (l/c=0). $\alpha = 3.5°$ in cavitating flow (10%, 20%, 30%, and 40%).

l/c	Experiment		Theory		% Difference	
	C_L	C_D	C_L	C_D	C_L	C_D
0.0	0.3619	0.0119	0.3682	0.0102	2%	15%
0.1	0.4064	0.0164	0.3930	0.0172	3%	5%
0.2	0.4036	0.0190	0.4065	0.0182	1%	4%
0.3	0.4225	0.0208	0.4094	0.0184	3%	12%
0.4	0.4621	0.0261	0.4247	0.0183	8%	30%

the fully-wetted results should match well with the analytical model. Under this assumption, the fully-wetted results provide a minimum bound to the errors expected in the cavitating comparisons.

Error cancellation is a common problem in experimental versus numerical comparisons. In light of this, the most trustworthy basis of comparison is the *actual velocities* as opposed to integrated quantities, such as the displacement thickness δ^*. For instance, the experimental and analytical displacement thickness, calculated from integrating the respective boundary layer profiles at the bottom of Figure 5-9, give very similar numbers; however, the actual boundary layer profiles differ drastically. Therefore, if the velocities compare well with experiment, then so should the displacement thickness, lift and drag, etc. but not necessarily vice-versa.

5.1 Forces in the Experiment

5.1.1 Method of Calculation

Lift and drag were computed from momentum theory using velocity measurements taken along a control surface about the hydrofoil as shown in Figure 2-1 (Kinnas, 1991).

From Newton's law and the momentum conservation law, the lift and drag can be expressed in terms of momentum integrations along a rectangular contour surrounding the foil. The lift force is given by:

$$L = M_z^L + M_z^B - M_z^R - M_z^T + P_z \tag{5.1}$$

where M is the momentum flux through the left, L, right, R, bottom, B, and top, T sides of a rectangular contour about a hydrofoil (see Figure 2-1) and are defined as:

$$
\begin{aligned}
M_z^{L,R} &= \rho \int_{z_B}^{z_T} w_{L,R} u_{L,R} dz \\
M_z^{B,T} &= \rho \int_{x_L}^{x_R} w_{B,T} w_{B,T} dx
\end{aligned}
\tag{5.2}
$$

$$P_z = \frac{\rho}{2} \int_{x_L}^{x_R} (u_T^2 + w_T^2 - u_B^2 - w_B^2) dx \tag{5.3}$$

and,

$$D = \rho U_\infty \int_{z_L}^{z_U} \Delta u_R dz - \rho \int_{z_L}^{z_U} (\Delta u_R)^2 dz \tag{5.4}$$

where Δu_R is the horizontal velocity defect in the wake and z_L and z_U is the vertical location of the bottom and top of the wake defect region, respectively, of the rectangular contour.

Thus, the data collected from a contour around the foil can be used with these integrations to calculate the lift and drag force acting on the foil. In this formulation, the flow is considered inviscid on the top and bottom cuts of the contour. Also, the effects of viscosity due to right and left sides of the rectangle are shown, in Kinnas (1991), to have negligible effect on the lift.

5.1.2   Comparisons with Theory

Figure 5-1 illustrates the experimental and analytical lift and drag coefficients, computed from equations (5.1) and (5.4) respectively. In Figure 5-1, the fully-wetted results ($l/c=0$) compare very well with the analytical model. For the larger cavity lengths, the experiment separates from theory. As mentioned earlier, this can be explained by the increased

unsteadiness in the larger cavities.

5.2 Velocity Comparisons

5.2.1 Near the Cavity Surface

Velocities are compared on a vertical traverse above the cavity surface. The numerical method gives the cavitation number, σ, for a given l/c. Equation (3.6) relates the cavity velocity, q_c, to the cavitation number, σ. Figure 5-2 shows the horizontal velocities along a traverse above the cavity. The results are shown for various cavity lengths. q_c^{exp} is defined as the dash line in Figure 5-2. Notice that the error becomes larger as the cavity length increases. This can be explained by the increasing amount of unsteadiness of the cavity with increasing cavity lengths.

5.2.2 On Rectangular Control Surface

Velocities are also compared on the rectangular control surface along which LDV measurements are obtained, as shown in Figure 2-1. Velocities can be obtained from the analytical model anywhere in the flow-field by summing the contribution of the velocity induced by each singularity (including the boundary layer sources and images) on the foil and wake surface.

As is expected, the comparisons are in good agreement with theory for the fully-wetted case, Figure 5-4. As l/c increases, the velocities stray from theory near the region of the cavity as shown in Figures 5-5 - 5-7. In addition, it should be noted that the standard deviations become larger with increasing cavity extent. This can be attributed to the increasing diameter of the entrained bubbles in the flow, which obscures the path of data retrieval of the LDV.

In Figures 5-4, 5-5, 5-6, and 5-7, the analytical model does not predict the velocity defect in the wake of the foil. However, this momentum deficit can be predicted using a method similar to that described in Appendix B. Figure D-4 shows the viscous model's prediction of the velocity profile in the wake of a fully-wetted hydrofoil for a variety of
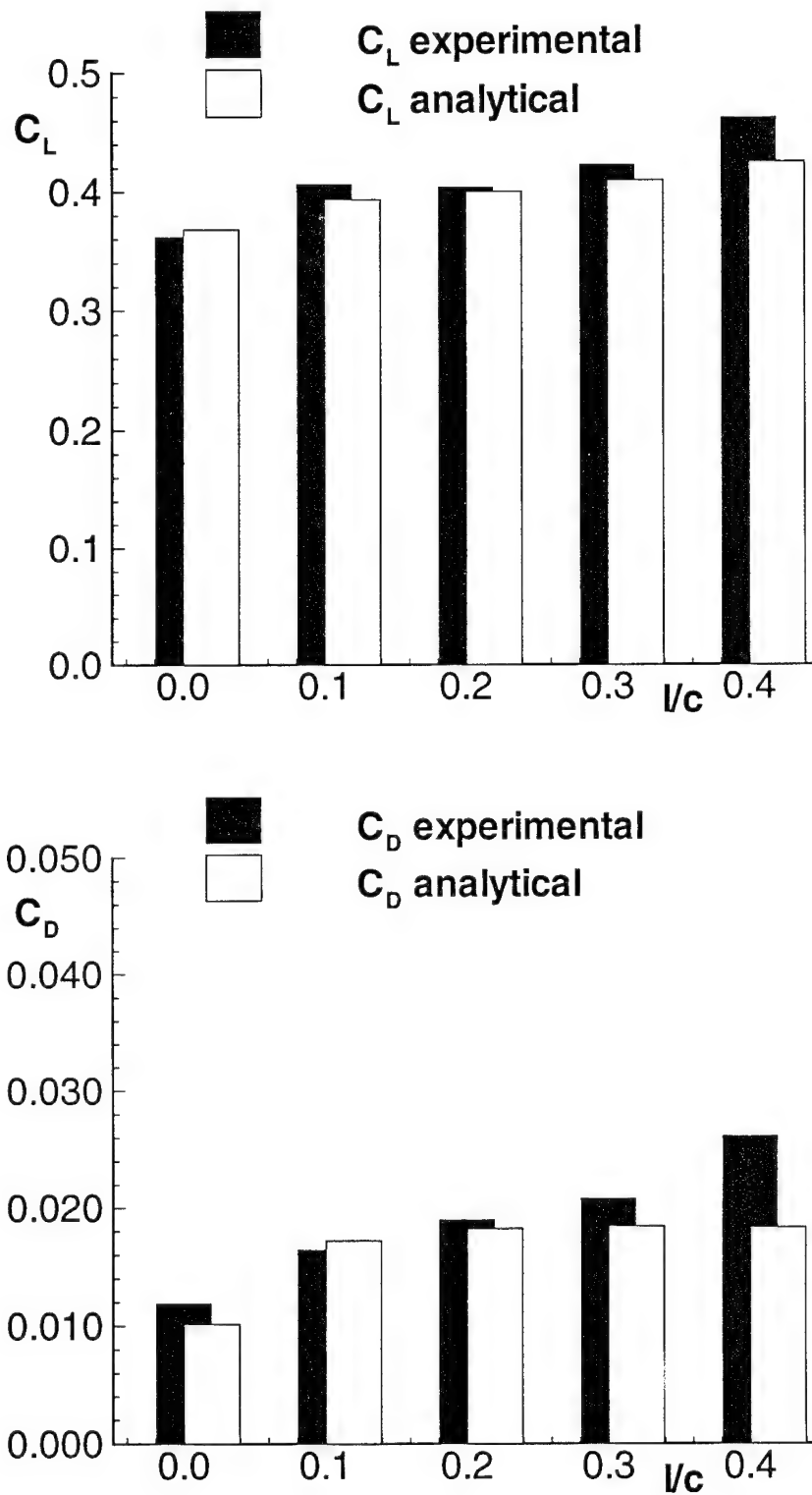
Figure 5-1: Above: the experimental lift coefficient versus the analytical model's prediction for the variety of cavity lengths. Below: the drag coefficient versus the analytical model's prediction.
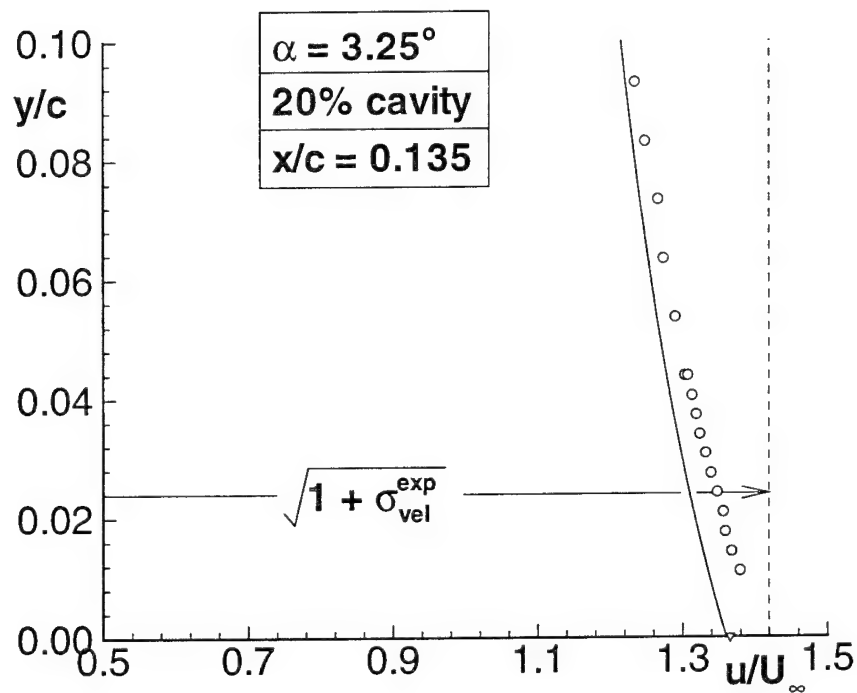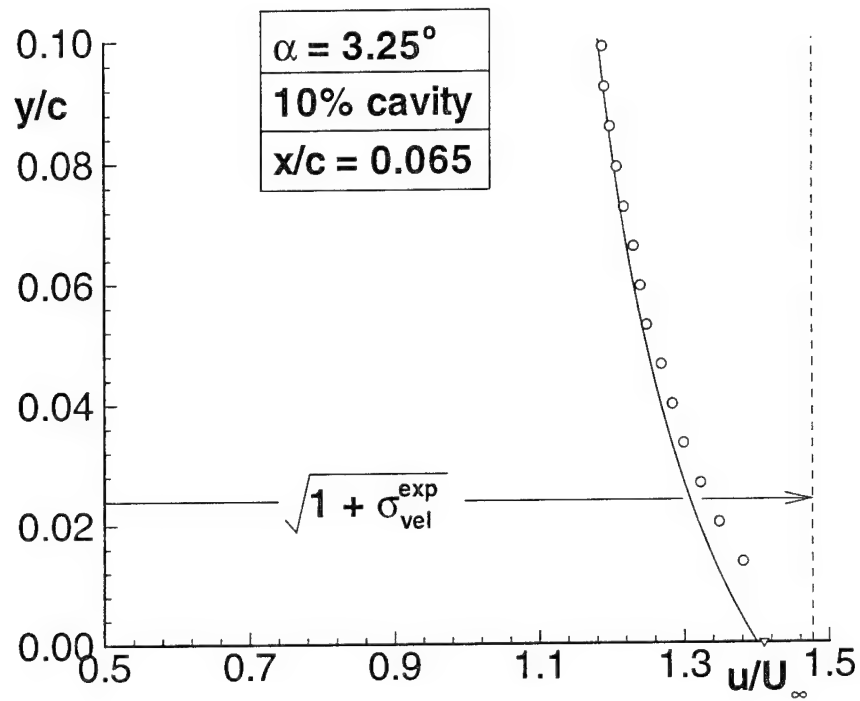
Figure 5-2: Velocity measurements along the normal to the cavity surface for cavity lengths of $l/c = 0.10, 0.20$. $\alpha = 3.25°$. ($y = 0$ corresponds to the cavity surface location)
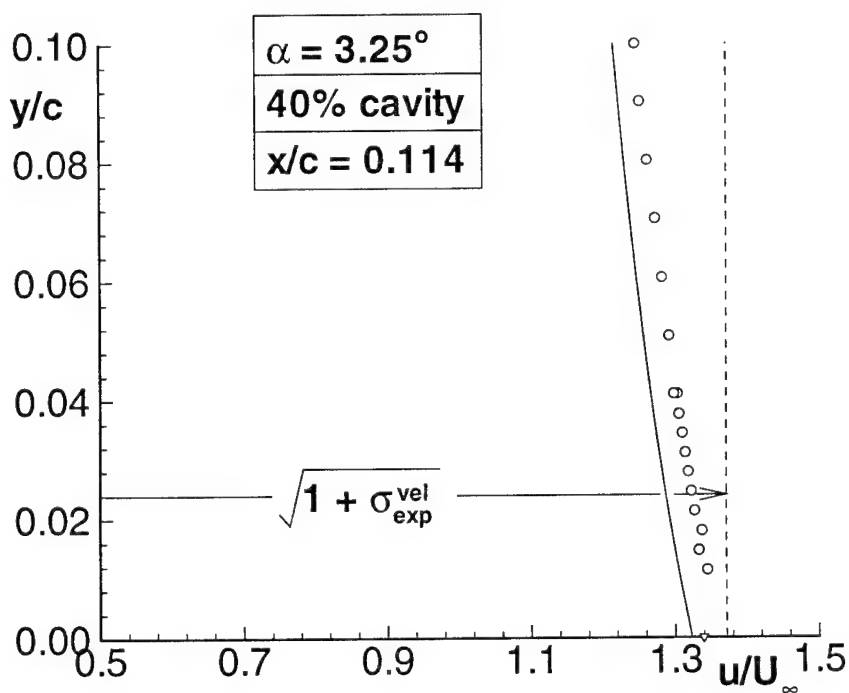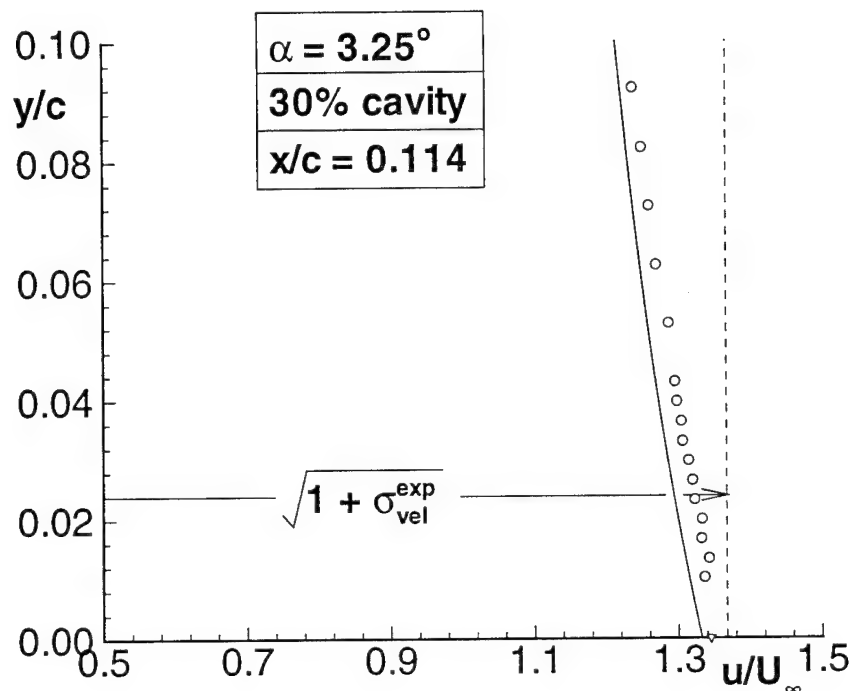
Figure 5-3: Velocity measurements along the normal to the cavity surface for cavity lengths of $l/c = 0.30, 0.40$. $\alpha = 3.25°$. ($y = 0$ corresponds to the cavity surface location)

pressure-side transition locations. It was necessary to study the transition location in Phase I of the experiment because transition to turbulent flow was not stimulated (as was the case in Phases I & II of the experiment).

5.2.3 In the Boundary Layer

Figures 5-8 - 5-10 compare experimental velocity measurements (circles) to analytical approximations (solid lines) given by the viscous model via Swafford's method, which is described in Appendix B.

It is evident in Figures 5-8 - 5-10 that θ^{exp} is greater than θ^{an}, where θ^{exp} is the experimental momentum thickness and θ^{an} is the analytical momentum thickness.[2] The reason for this large difference in momentum thickness is:

> *The current inviscid/viscous flow coupling does not provide for the momentum loss at the trailing edge of the cavity.*

One way of modeling this increased momentum thickness would be to add a jump, $\Delta\theta$, in the momentum thickness at the trailing edge of the cavity. The value of $\Delta\theta$ should be the value which would give the same total drag as equation (3.41) gives in the present method. Thus, if a jump were imposed, the "far-wake" approximation, equation (3.43), would capture the total drag (including the cavity drag) acting on the hydrofoil.

Although the boundary layer profiles do not match well for the cavitating case, the fully-wetted analytical profiles match almost identically with that of the experiment.

5.2.4 Pressure Measurements

Cavitation numbers are compared in Table 5.2. Three methods were used in computing the cavitation number here:

1. σ_p^{exp} is the cavitation number as measured from the manometer shown in Figure 2-7, and given by equation (2.3)

---

[2]Kato (1987) observed the differences in displacement thickness between cavitating and fully-wetted flow.

$$\alpha = 3.25^o \ fully\text{-}wetted$$
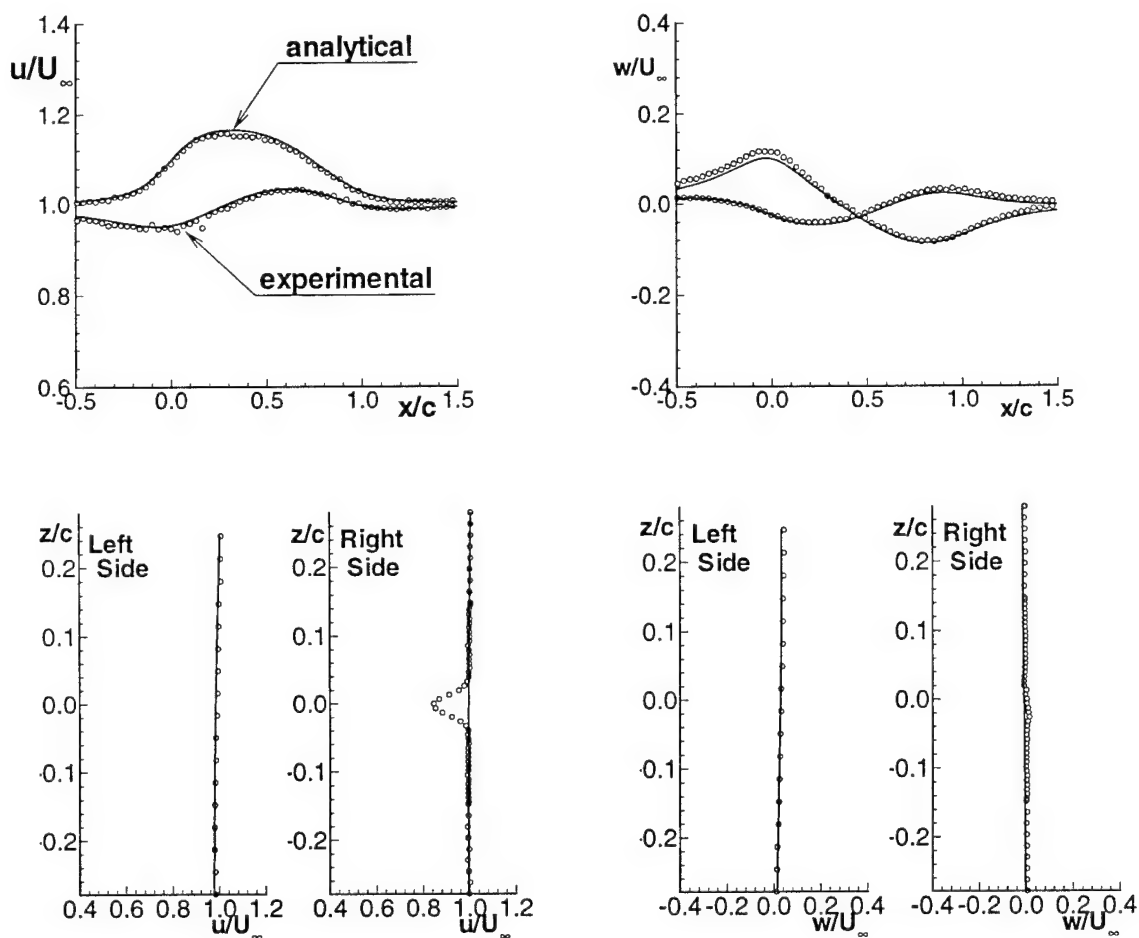
Figure 5-4: Horizontal and vertical velocities along all sides of a rectangular contour surrounding the hydrofoil. $fully - wetted$, $\alpha = 3.25^o$.

$$\alpha = 3.5^o \qquad 10\% \; cavity$$
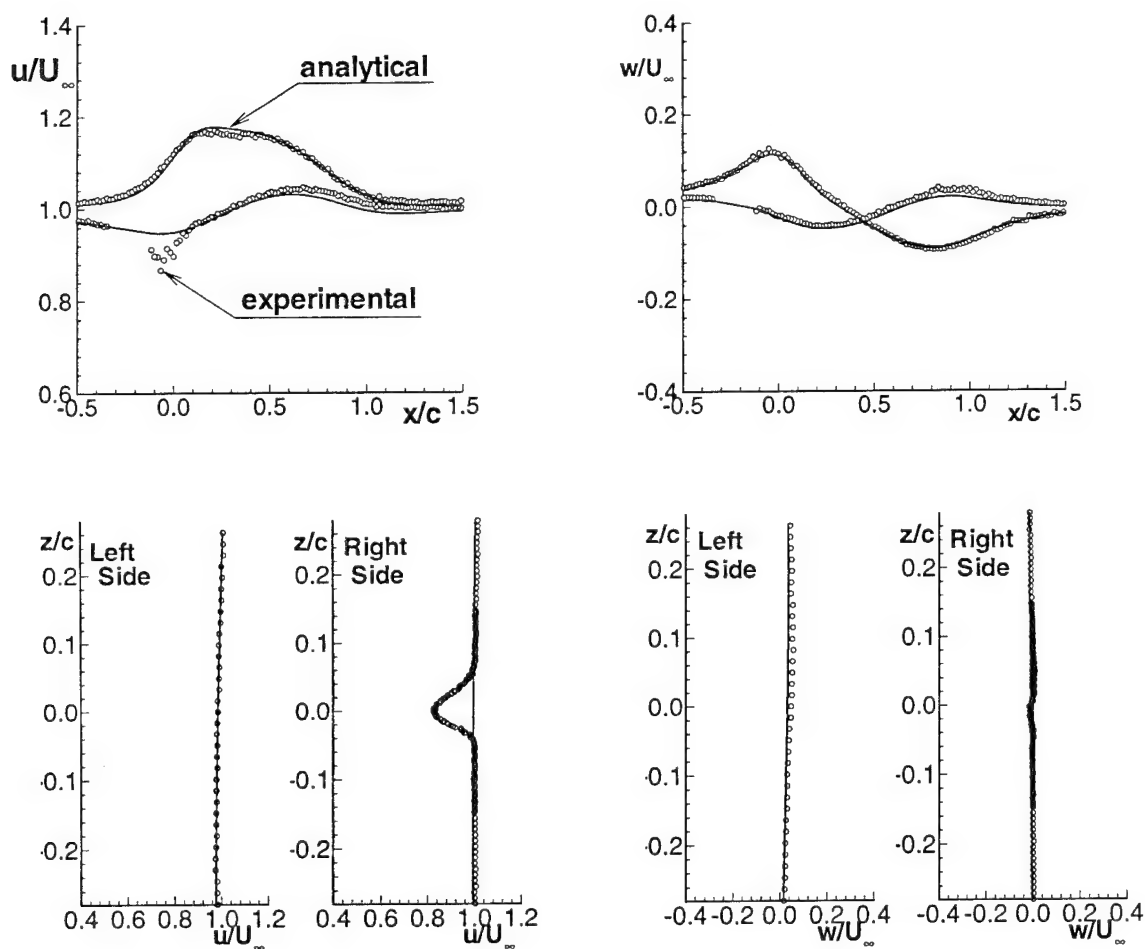
Figure 5-5: Horizontal and vertical velocities along all sides of a rectangular contour surrounding the hydrofoil. $l/c = 0.10$, $\alpha = 3.5^o$.

$$\alpha = 3.5^o \quad 20\% \; cavity$$
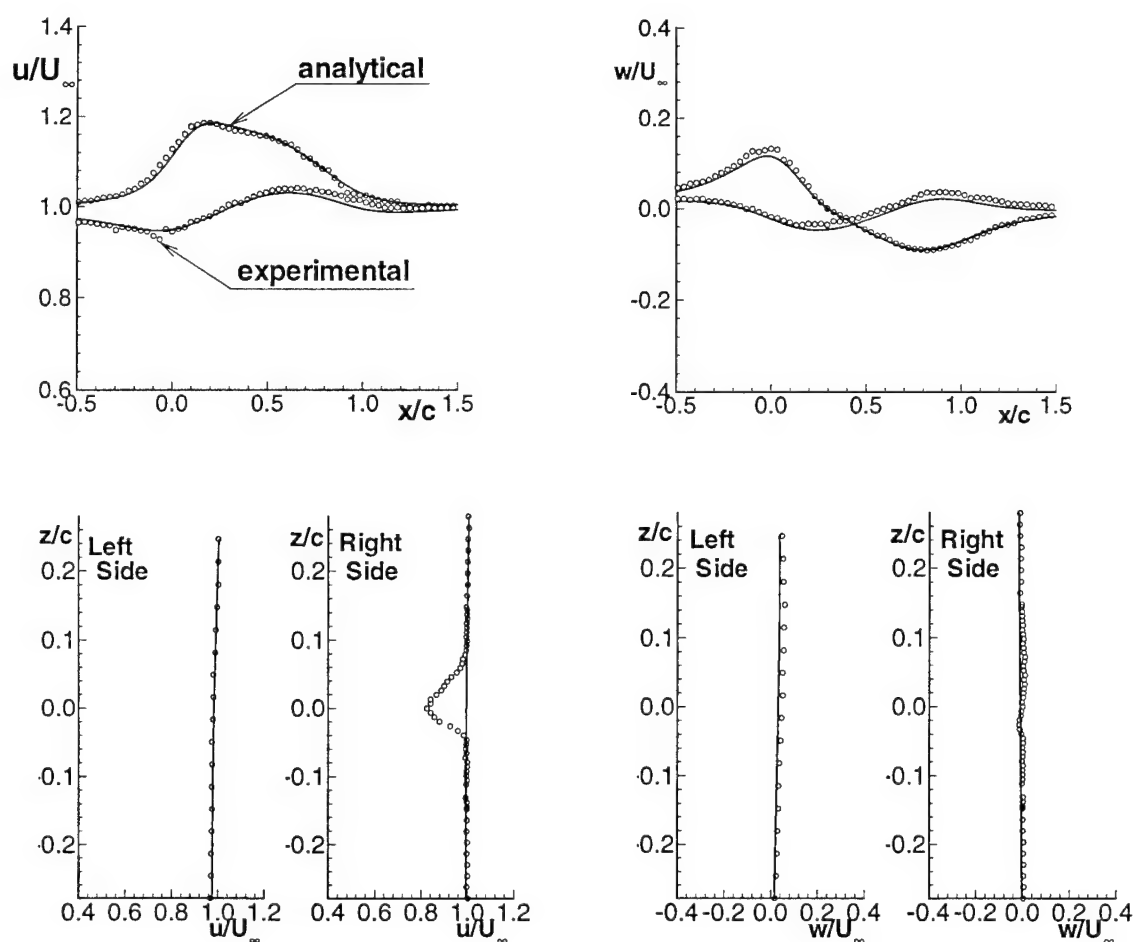
Figure 5-6: Horizontal and vertical velocities along all sides of a rectangular contour surrounding the hydrofoil.$l/c = 0.20$, $\alpha = 3.5°$.
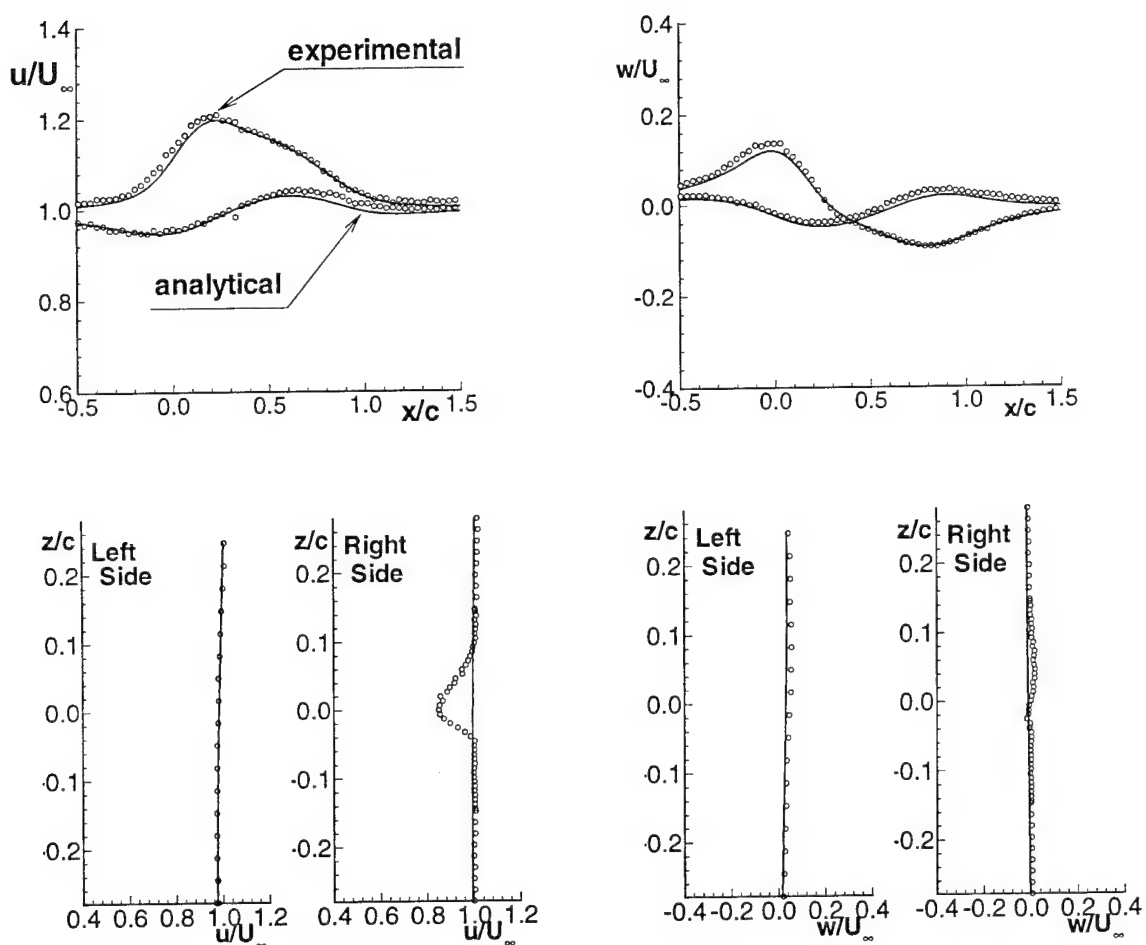
Figure 5-7: Horizontal and vertical velocities along all sides of a rectangular contour surrounding the hydrofoil. $l/c = 0.30$, $\alpha = 3.5°$.
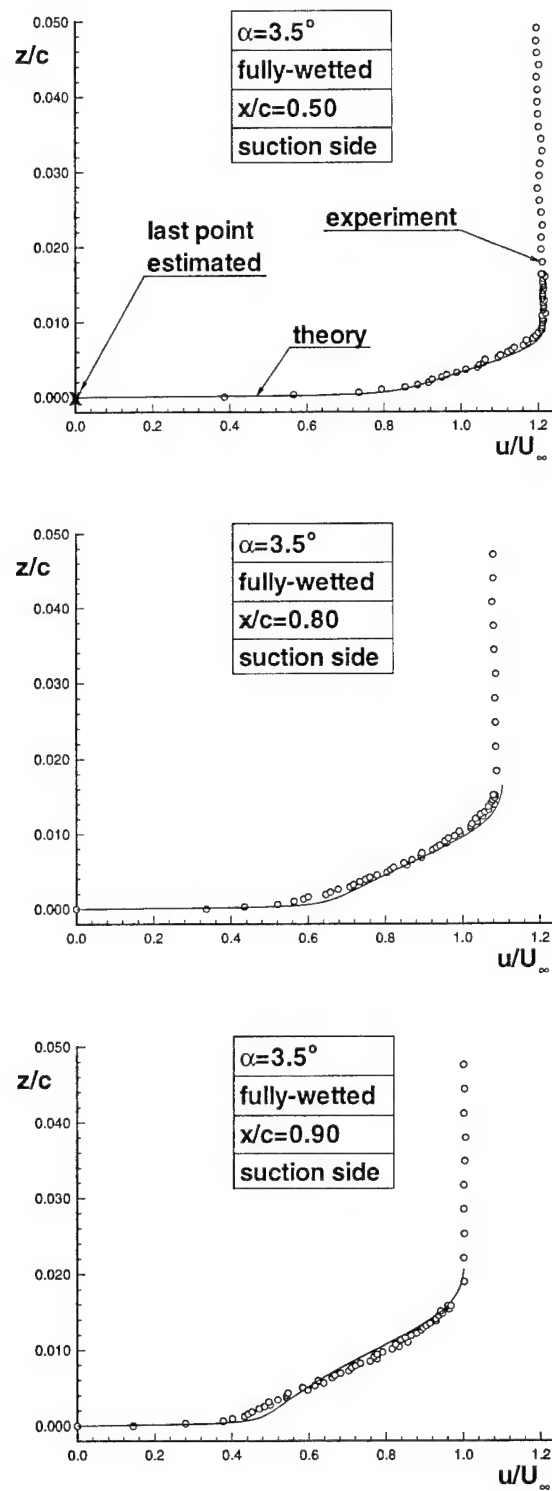
Figure 5-8: Top: Boundary layer profiles comparing experiment (circles) and theory (solid line), $x/c = 0.50$, fully-wetted, and $\alpha = 3.5°$. Middle: $x/c = 0.80$. Bottom: $x/c = 0.90$.
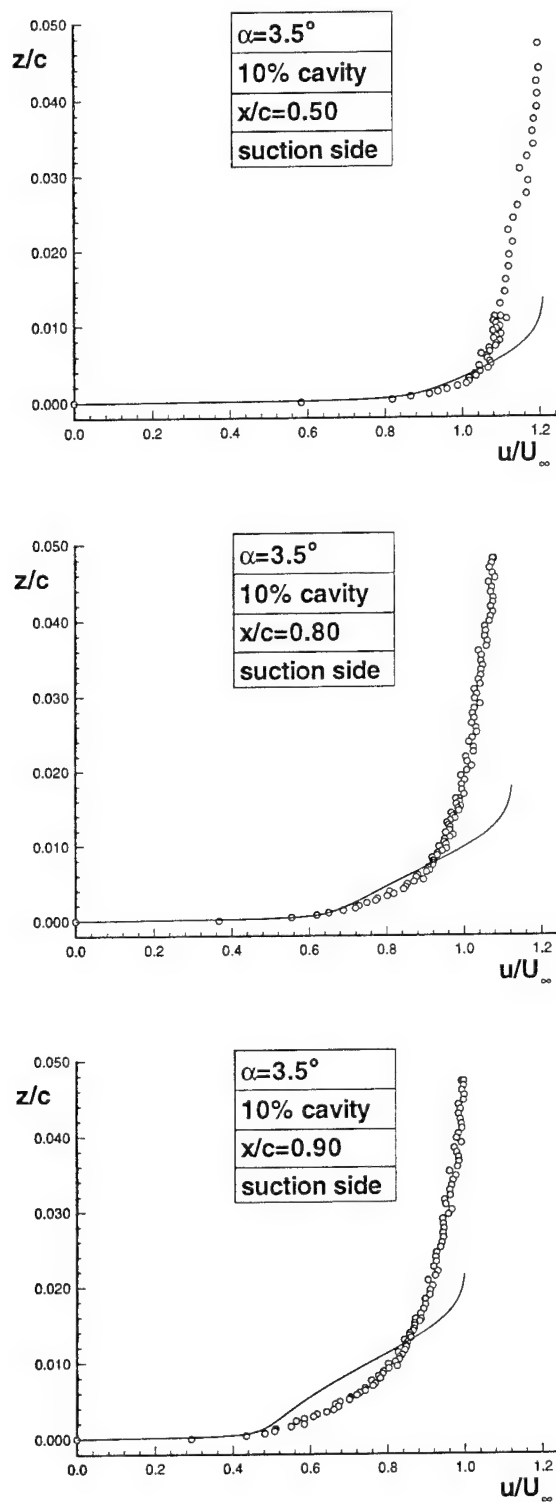
Figure 5-9: Top: Boundary layer profiles comparing experiment (circles) and theory (solid line), $x/c = 0.50$, $l/c = 0.10$ and $\alpha = 3.5°$. Middle: $x/c = 0.80$. Bottom: $x/c = 0.90$.
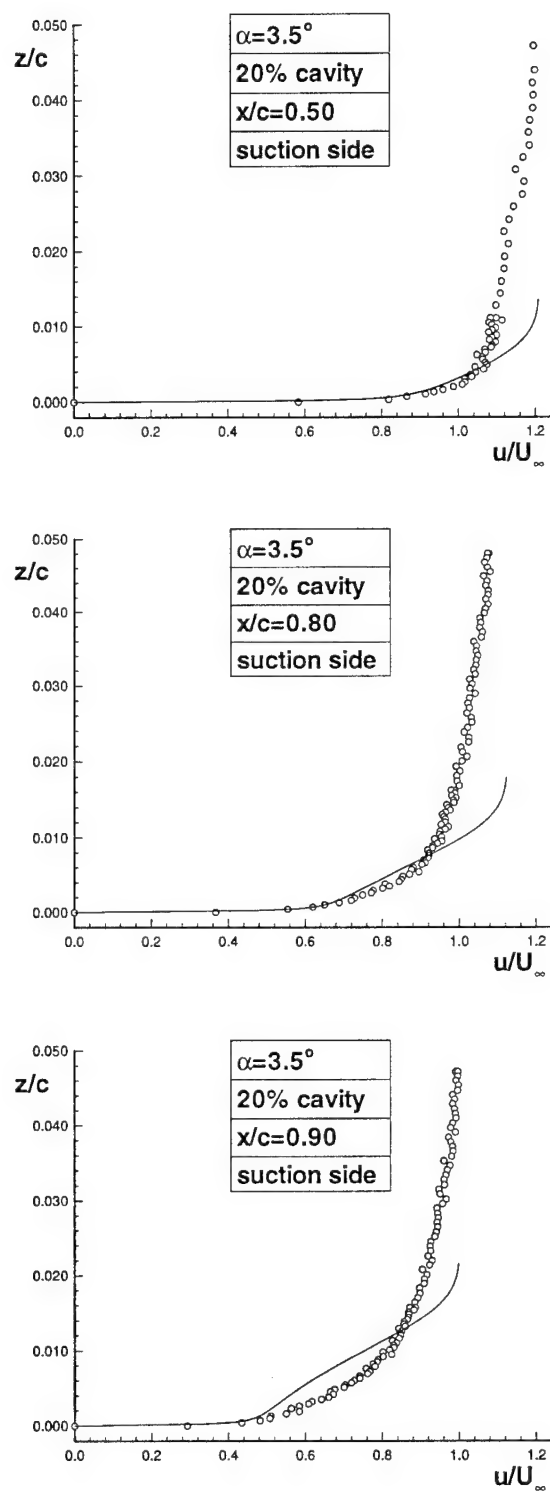
Figure 5-10: Top: Boundary layer profiles comparing experiment (circles) and theory (solid line), $x/c = 0.50$, $l/c = 0.20$ and $\alpha = 3.5^o$. Middle: $x/c = 0.80$. Bottom: $x/c = 0.90$.

Table 5.2: Cavitation number comparisons between experiment and theory, $\alpha = 3.25^o$. (*exp* stands for experimental, *p* for differential pressure manometer, *ptun* for tunnel pressure manometer, *vel* for velocity measurements, *an* for analytical result, *inv* for inviscid, and *vis* for viscous.)

| l/c	σ_p^{exp}	σ_{ptun}^{exp}	σ_{vel}^{exp}	σ_{inv}^{an}	σ_{vis}^{an}
0.0	0.8850	—	—	0.9795	0.8510
0.1	1.1215	1.0203	1.2041	1.0578	0.9871
0.2	0.9893	0.9053	1.0118	0.9205	0.8649
0.3	0.9296	0.8362	0.8520	0.8597	0.8081
0.4	0.8784	0.8132	0.8651	0.8379	0.7974

2. σ_{ptun}^{exp} is the cavitation number measured from the tunnel pressure manometer,[3] given by:

$$\sigma_{ptun}^{exp} = \frac{\rho_{Hg}gh + p_v(T_{tun}) - p_v(T_{room})}{\frac{1}{2}\rho_{H_2O}U_\infty^2} \qquad (5.5)$$

Equation (5.5) takes into account the difference in vapor pressure between the tunnel temperature, T_{tun}, and room temperature, T_{room}.

3. σ_{vel}^{exp} is the cavitation number computed by using equation (3.6) and the cavity velocity, q_c

Method 1 is used in fully-wetted flow to determine the pressure coefficient on the foil. On the other hand, method 2 is used in the case of cavitating flow to determine the cavitation number. Figure 5-11 shows $-C_P$ in the case of fully-wetted flow, and σ_{ptun}^{exp} in the case of cavitating flow. In Figure 5-11, the cavitation number is computed from equation (5.5).

5.2.5   Errors in Determining the Foil Surface

Although the LDV positioning system is extremely accurate,[4] there still exists some uncertainty in determining the foil surface. This uncertainty is evidenced in the boundary

---

[3]The tunnel pressure manometer measures *only* the pressure in the free-stream. The low side of the manometer is directly connected to a reservoir containing vapor pressure.

[4]The maximum error associated with the position of the laser is 0.5mm.
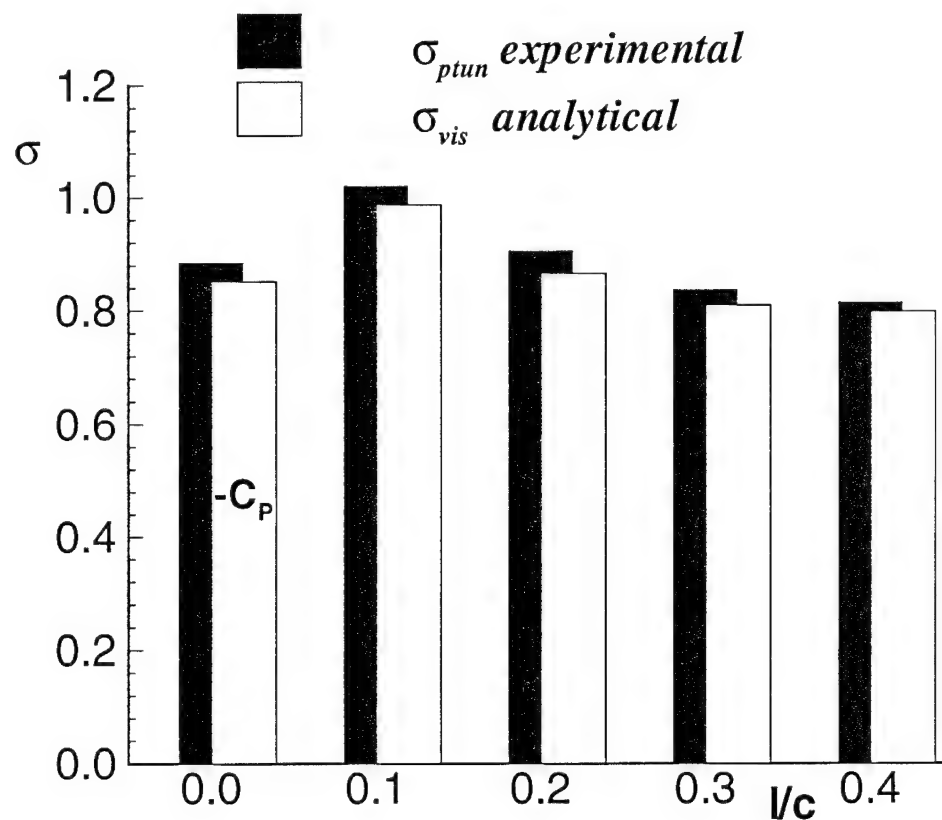
Figure 5-11: Comparison of cavitation number (pressure coefficient in fully-wetted flow) between experiment and theory for various cavity lengths. $\alpha = 3.25^0$.

layer profile comparisons. In other words, the experimental data is shifted from the ex-
perimental coordinate system (shown in Figure 2-1) to the numerical coordinate system,
in which case the foil surface is at $z = 0$.

One way of finding the foil surface is to assume the viscous sublayer is approximately
linear. In this case, the experimental profile can be extrapolated using a least squares fit
to data points measured in the sublayer. However, this assumes that a sufficient amount
of points are measured in the viscous sub-layer. Since only one or two measurements
are typically obtained in the sublayer, the extrapolated location of the foil surface has
a relatively large margin of error. Instead of using this method, the lowest data point
measured is just assumed to be the foil surface (which works very well if the data is finely
spaced).

Chapter 6

Conclusions

A systematic comparison between experiment and theory has been performed for a partially-cavitating hydrofoil. Velocity measurements near the cavity surface are compared with the numerical prediction. Also, velocities are compared in the boundary layer region and on a rectangular contour surrounding the hydrofoil. The results are in very good agreement with those from the analysis method in the case of fully-wetted flow, but begin to deteriorate with increasing cavity extent.

A coupled, nonlinear, inviscid cavity analysis method and a boundary layer solver is shown to accurately predict the velocities anywhere in the flow-field in fully-wetted flow. In this analysis method, tunnel walls are accurately modeled with an adequate number of image singularities, representing the foil, cavity, and displacement thickness. In cavitating conditions, the analysis method correlates well with the experiment in the regions of inviscid flow; however, in the boundary layer region, the analysis method does not accurately model the displacement and momentum loss of the cavity (as evidenced in velocity profiles aft of the cavity). Lift and drag coefficients, computed from momentum integrations, are shown to be in good agreement with those predicted from the analysis method.

6.1   Application to Propulsor Blades

Nothing yet has been mentioned about the applicability of the present method to propulsor blades. The philosophy underlying the motivation to model viscous flow around cavitating propulsors is to be extremely systematic in reaching the final goal, ensuring that each step in the process is accurately modeled. This means starting with simple geometries and working to more complex ones.

The present method can be extended to three-dimensional geometries by employing a technique called the "equivalent" σ along two-dimensional strips of a three-dimensional geometry (Kinnas et al., 1994). In the case of cavitating flow, since the lift is fixed to the designer's desire, the procedure would include finding the correct cavity length as an input to PCPAN/SCPAN; the correct cavity length would be that which gave the correct lift under viscous flow as in inviscid flow. Thus, the "equivalent" σ^{vis} in viscous flow is σ^{inv} in inviscid flow that produces the same lift coefficient. This method can be applied to propeller blades by calculating a new "equivalent" σ at each radial strip along the blade.

Figure 4-5 can be used, for super-cavitating foils, to find the cavity length in viscous flow which produces the same lift as an "equivalent" cavity length in inviscid flow. Similar figures are shown in Kinnas (1994) which can be used to find the "equivalent" cavity length for partially-cavitating foils.

Fine and Kinnas (1992) solved for the cavity solution over finite-span three-dimensional hydrofoils using a *fully nonlinear, three-dimensional cavity analysis* method. In their routine, the cavity analysis method would iteratively calculate the cavity planform at all locations along the span. Hufford, on the other hand, (1990) solved for the *fully-wetted* flow around propulsor blades by applying the two-dimensional boundary layer equations in a strip-wise sense. Hence, one possible way to address the problem of viscous cavitating flow over three-dimensional geometries would be to apply Hufford's method on the "compound" blade (the surface confined by both the cavity and foil surface) produced from the method of Kinnas and Fine (1992).

6.2 Recommendations

This thesis attempts to further develop an analysis method for solving the viscous flow around cavitating propulsors. This has been accomplished by using experimentation to further study cavitation, using experimental results to validate the numerical method, and modifying the code to give results that parallel those obtained in experiments.

Villeneuve (1993) used a strongly-coupled viscous/cavity approach, which simultaneously solved for the sources due to both cavity height and effects of the boundary layer. In his method, the blowing sources were placed on the foil surface underneath the cavity. It was noticed that Villeneuve's method became problematic when the cavity height was large with respect to the displacement thickness.

This work rectified the problematic behavior of Villeneuve's method by using a lightly coupled viscous/cavity approach in which case the nonlinear cavity is first determined in inviscid flow. The blowing sources representing the boundary layer are then applied to the cavity surface. Results presented herein have shown that this method works very well.

However, the present method *still* does not correctly solve the problem. And this can be evidenced by the fact that the dynamic boundary condition is not satisfied on the entire extent of the cavity (see Figure 3-7). While the pressure *typically* does not vary much from the cavitation number, there are some cases where the viscous cavitation number is not well defined at all.

A strongly coupled viscous/cavity solver that places the blowing sources on the updated cavity height would provide the most accurate solution to the problem of viscous cavitating flow around hydrofoils. This could be accomplished using PCPAN/SCPAN and CAV2D-BL in an iterative manner. Thus,

- PCPAN/SCPAN would generate the cavity solution

- CAV2D-BL would calculate the viscous flow on the present iteration's "compound" foil

- the displacement thickness would be added to the present iteration's "compound"
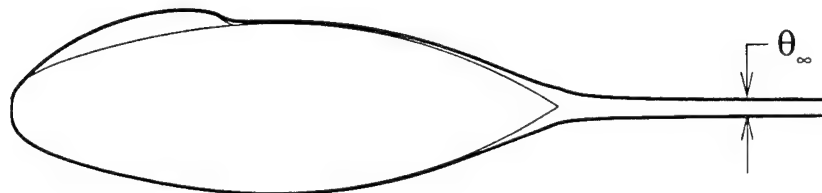
foil

- PCPAN/SCPAN would be run again, now solving for the incremental cavity height that would make the foil satisfy both the kinematic and dynamic boundary condition

- This would update until the incremental cavity height becomes smaller than a specified criterion

Although more accurate, this method has the trade-off of being less computationally efficient. Kinnas et al (1994) performed two iterations of this method and found the results not to differ much from the present method.
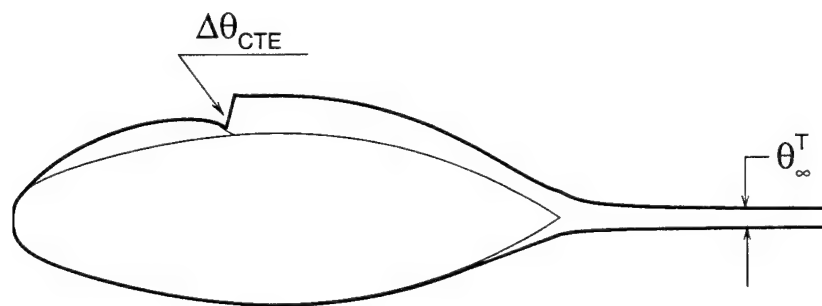
6.3   Preliminary "Momentum Jump" Model

Accurately modeling the energy losses caused by the cavity should be of primary focus in the continued development of CAV2D-BL. Although, the experimental forces correlate well with theory, the flow-field cannot accurately be modeled without the implementation of a "momentum jump" model – which would model the momentum deficit produced by the cavity via adding the correct amount of momentum and displacement thickness at the trailing edge of the cavity. Figure 6-1 illustrates the concept adding a jump at the trailing edge the cavity. To date, the current method includes only a *preliminary* momentum jump. Figure 6-2 shows results from the current method of the momentum thickness along the suction side the foil and wake surface. In this figure, $\Delta\theta_{CTE}$ is the value that the user specifies, which, when added just aft of the cavity, would capture the total drag in the wake, $2\theta_\infty^T$. The bottom graph in Figure 6-2 shows how the analytical velocity profile changes, with increasing θ, to favor the experimental profile.

The current preliminary results do not accurately model the additional increase in displacement thickness as observed by Kato (1987). Thus, the completion of the current work lies in determining a method for calculating both δ_{CTE}^* and $\Delta\theta_{CTE}$, which, when applied, would produce velocity profiles similar to those observed in experiments.

Current method:

$$\text{where } \theta_\infty = \frac{C_D^{vis}}{2}$$

Momentum jump model:

$$\text{where } \theta_{CTE} \text{ is such that: } \theta_\infty^T = \frac{C_D^{vis} + C_D^{inv}}{2}$$

Figure 6-1: Top: the current viscous cavity model showing the momentum thickness along the foil and wake surface. Bottom: the current model with the proposed jump model.
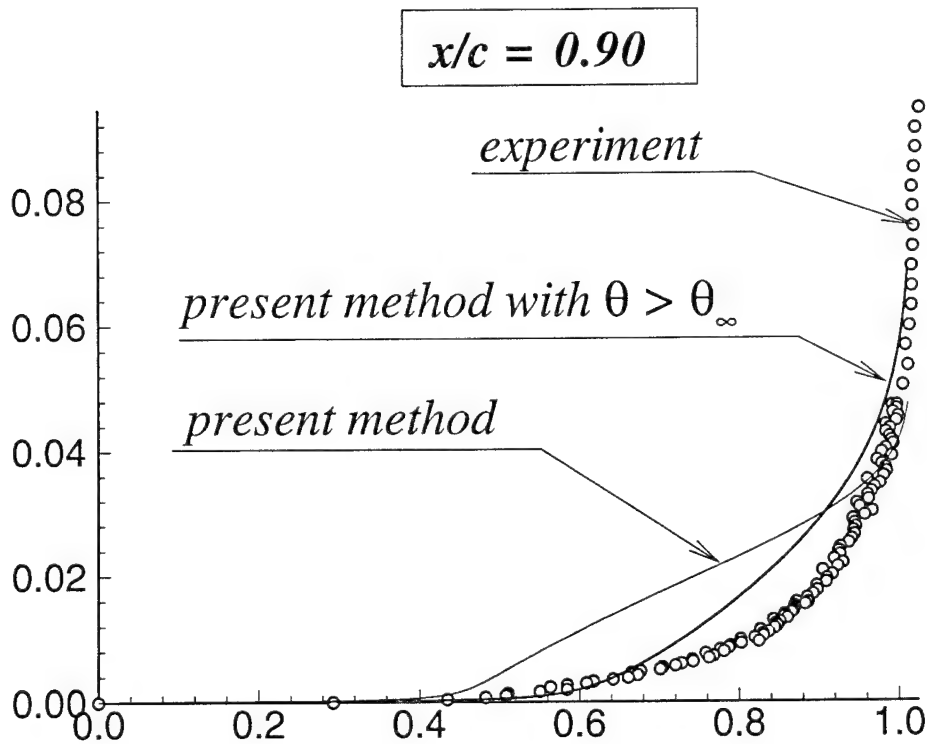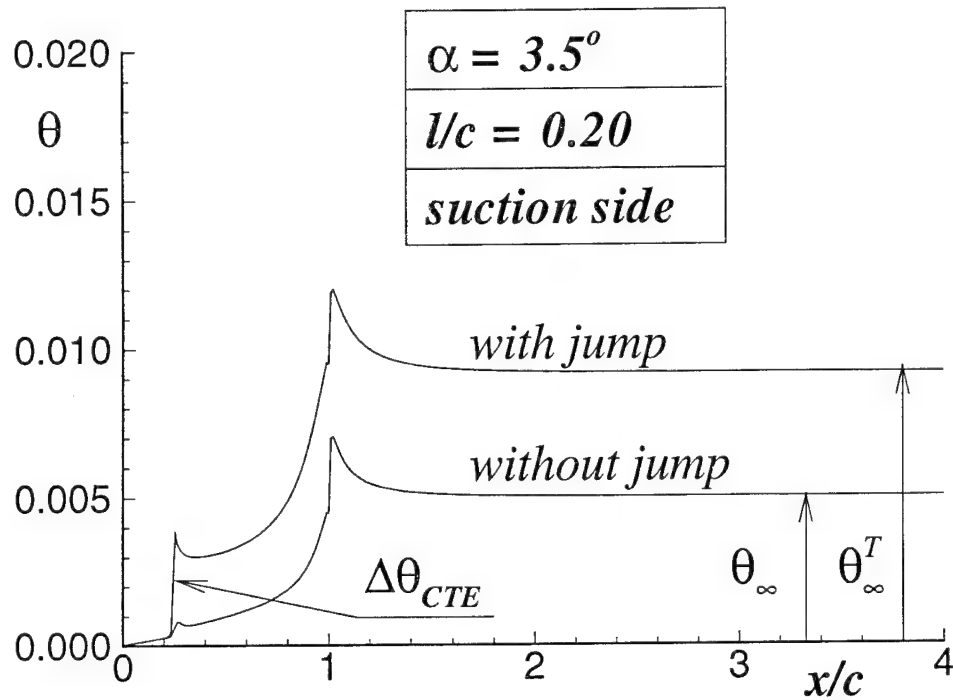
Figure 6-2: Top: preliminary results of the proposed jump model showing the momentum thickness along the suction side of the foil and wake. Bottom: velocity profiles showing trends of increasing momentum thickness.

Bibliography

Baker, E., 1972. Analytical Prediction of Wall Effect on Fully Cavitating Lifting Foils, Using Nonlinear Theory. Technical Report No. 3688, NSRDC.

Drela, M., 1989. XFOIL: An Analysis and Design System for Low Reynolds Number Airfoils. In *Lecture Notes in Engineering (Volume 54, Low Reynolds Number Aerodynamics)*, New York. Springer-Verlag.

Fine, N., 1988. Computational and Experimental Investigations of the Flow Around Cavitating Hydrofoils. Technical Report No. 88-6, MIT, Department of Ocean Engineering.

Fine, N. and Kinnas, S., 1993. A Boundary Element Method for the Analysis of the Flow Around 3-D Cavitating Hydrofoils. *Journal of Ship Research*, 37:213–224.

Franc, J. and Michel, J., 1985. Attached cavitation and the boundary layer: Experimental investigation and numerical treatment. *Journal of Fluid Mechanics*, vol. 154:pp 63–90.

Geurst, J., 1959. Linearized Theory for Partially Cavitated Hydrofoils. *International Shipbuilding Progress*, 6-60.

Hufford, G., 1990. Viscous Flow Around Marine Propellers Using Boundary Layer Strip Theory. Master's thesis, Massachusetts Institute of Technology.

Kato, H., Yamaguchi, and Kubota, A., 1987. Laser Doppler Velocimeter Measurements in Cavitation Tunnel. In *Volume 2, Proceedings of the 18th International Towing Tank Conference*, pages 433–437, Kobe, SNAJ.

Kerwin, J., 1992. The MIT Marine Hydrodynamics Water Tunnel - A 53rd Anniversary Celebration. Presented at the New England Section SNAME Meeting, MIT.

Kinnas, S., 1991. Hydrofoil Lift and Drag from Momentum Integrations. Technical Report No. 91-4, Department of Ocean Engineering, MIT.

Kinnas, S. and Fine, N., 1990. Non-Linear Analysis of the Flow Around Partially or Super-Cavitating Hydrofoils by a Potential Based Panel Method. In *Boundary Integral Methods-Theory and Applications, Proceedings of the IABEM-90 Symposium, Rome, Italy, October 15-19, 1990*, pages 289–300, Heidelberg. Springer-Verlag.

Kinnas, S. and Fine, N., 1992. A nonlinear boundary element method for the analysis of unsteady propeller sheet cavitation. In *Proceedings of the Nineteenth Symposium on Naval Hydrodynamics*, Seoul, Korea.

Kinnas, S. and Fine, N., 1993. A Numerical Nonlinear Analysis of the Flow Around Two- and Three-dimensional Partially Cavitating Hydrofoils. *Journal of Fluid Mechanics*, 254:151–181.

Kinnas, S. and Mazel, C., 1993. Numerical vs. Experimental Cavitation Tunnel (A Supercavitating Hydrofoil Experiment). *Journal of Fluids Engineering*, 115:pp. 760–765.

Kinnas, S., Mishima, S., and Brewer, W., 1994. Non-Linear Analysis of Viscous Flow Around Cavitating Hydrofoils. In *Proceedings of the Twentieth Symposium on Naval Hydrodynamics*, Santa Barbara, California. Office of Naval Research.

Lurie, E. H., 1993. Unsteady Response of a Two-dimensional Hydrofoil Subject to High Reduced Frequency Gust Loading. Master's thesis, Massachusetts Institute of Technology.

Lurie, E. H., 1995. A Preliminary Note on Error Analysis of the Flapping Foil Experiment. Technical Report No. 95-3, Department of Ocean Engineering, MIT.

Maixner, M. R., 1977. An Experimental Investigation of Wall Effects on Supercavitating Hydrofoils of Finite Span. Technical Report No. 83481-3, Department of Ocean Engineering, MIT.

Meijer, M., 1959. Some Experiments on Partially Cavitating Hydrofoils. *International Shipbuilding Progress*, 6(60).

Press, W. H., Teukolsky, S. A., Vetterling, W. T., and Flannery, B. P., 1992. *Numerical Recipes in Fortran*. Cambride University Press, New York.

Schlichting, H., 1979. *Boundary-Layer Theory*. McGraw-Hill, Inc.

Swafford, T., 1983. Analytical Approximation of Two-dimensional Separated Turbulent Boundary-layer Velocity Profiles. *AIAA paper, 21-6*.

Uhlman, S. S. and Jinag, C.-W., 1977. Experiments on a Partially Cavitating Plano-Convex Hydrofoil with Comparison to Theory. Technical Report No. 83481-2, MIT, Department of Ocean Engineering.

Villeneuve, R., 1993. Effects of Viscosity on Hydrofoil Cavitation. Master's thesis, Department of Ocean Engineering, MIT.

Wade, R., 1967. Linearized Theory of a Partially Cavitating Plano-Convex Hydrofoil Including the Effects of Camber and Thickness. *Journal of Ship Research*, 11-1.

Wade, R. B. and Acosta, A. J., 1966. Experimental Observations on the Flow Past a Plano-Convex Hydrofoil. *Journal of Basic Engineering*, pages 273–283.

Whitfield, D., 1978. Analytical Description of the Two-dimensional Turbulent Boundary-layer Velocity Profile. *AIAA paper, 78-1158*.

Wu, T., Whitney, A., and Lin, J., 1970. Final Report: Wall Effects in Cavity Flows. Technical Report No. E-97A-18, California Institute of Technology.

Appendix A

Calculating Displacement Thickness

In order to calculate the displacement thickness from the measured velocity profile, the data must be integrated either numerically or analytically. However, due to the physical limitations[1] of the LDV we could not measure the entire boundary layer profile (see Figure A-1), so numerical integration cannot accurately estimate the area under the missing region. Hence we must extrapolate the profile in that region.

In order to extrapolate the profile in this region, the following method was used (Press et al., 1992):

- a power law curve of the following general form is fit to the existing points:

$$u(z) = (Az + B)(z - z_o)^n \qquad (A.1)$$

- least squares can then be used to minimize the sum of the squares

$$G(a) = \sum_{i=1}^{N} [(u_{exp})_i - u(z_i; A, B, z_o, n)]^2 \qquad (A.2)$$

where $a = [A\ B\ z_o\ n]$

- by requiring

---

[1]We were not able to rotate the beams to measure the tangential component of the velocity near the foil surface. At stations near the trailing edge, where the foil surface was at a larger angle, one beam would become occluded as we tried to measure horizontal velocities
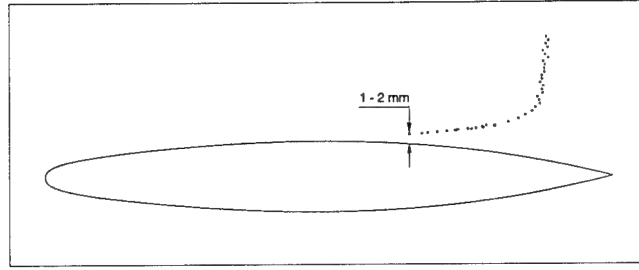
Figure A-1: A 1 - 2 mm gap in measuring exists between the foil and the closest point measured.

$$\frac{\partial G}{\partial a} = 0 \;\Rightarrow\; \frac{\partial G}{\partial A} = \frac{\partial G}{\partial B} = \frac{\partial G}{\partial z_o} = \frac{\partial G}{\partial n} = 0 \tag{A.3}$$

- simultaneously solve for A, B, z_o, n

- define δ^* in terms of $u(z)$, δ_{exp}, $u(\delta_{exp})$, and z

$$\delta^* = \int_0^{\delta_{exp}} \left(1 - \frac{u(z)}{u(\delta_{exp})}\right) dz \tag{A.4}$$

- find δ^* in terms of $u(z)$ by

$$\delta^* = \delta_{exp} - \frac{1}{u(\delta_{exp})} A \frac{\delta_{exp}^{n+2}}{n+2} + (Az_o + B) \frac{\delta_{exp}^{n+1}}{n+1} \tag{A.5}$$

where δ_{exp} is the boundary layer thickness estimated from the measured velocity profile.

Because the boundary layer profile increases asymptotically, δ_{exp} is not always a clearly defined quantity; it is typically taken as the height of the boundary layer when the velocity is 99% of the free-stream value (Schlichting, 1979). Due to the form of equation (A.5), errors due to the estimating the value of δ_{exp} are greatly magnified.

Figure A-2 shows an example of this method, which was applied to data from Phase I of the experiment. Although this seems to match well, this method can be deceiving because its accuracy is a function of the distance from the closest point to the foil.

Therefore, the method should only be used in cases where the LDV measures extremely close to the foil.
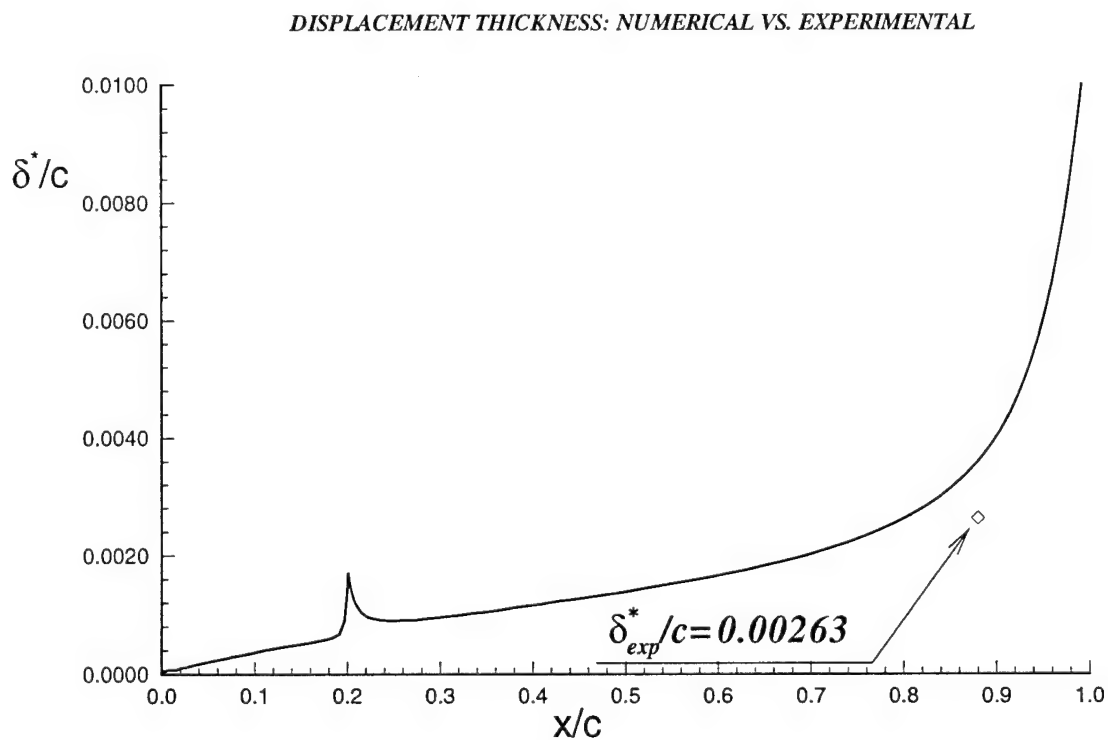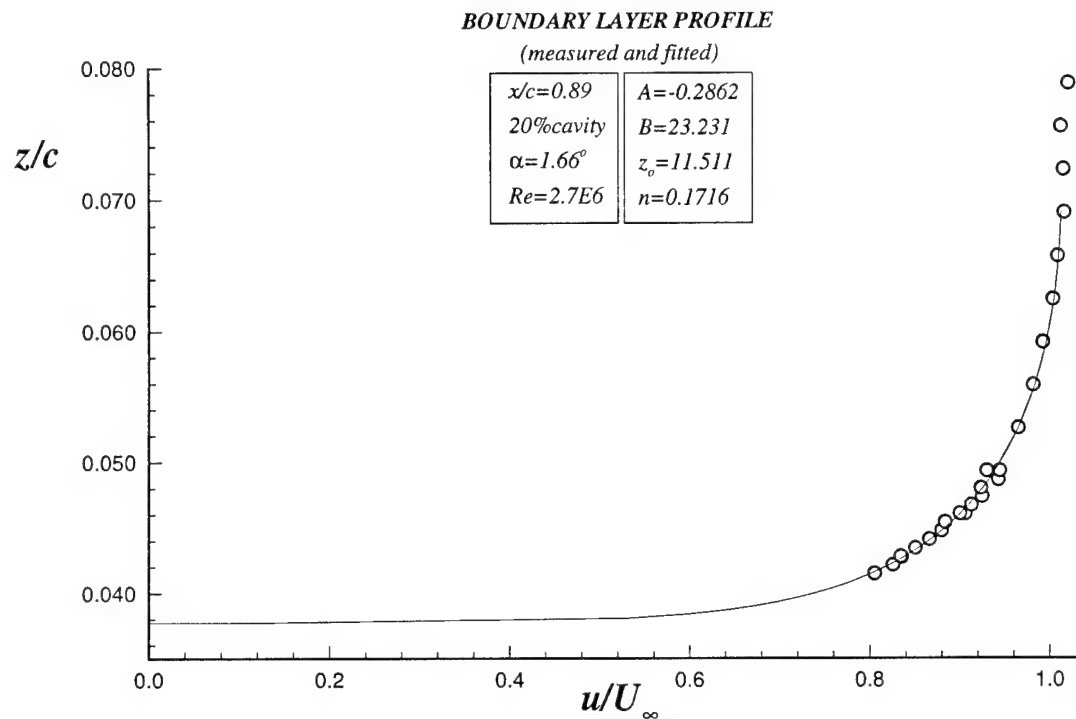
BOUNDARY LAYER PROFILE

(measured and fitted)

x/c=0.89	A=-0.2862
20%cavity	B=23.231
α=1.66°	z_o=11.511
Re=2.7E6	n=0.1716

DISPLACEMENT THICKNESS: NUMERICAL VS. EXPERIMENTAL

$\delta^*_{exp}/c = 0.00263$

Figure A-2: Above: The present method fit to a boundary layer profile. Below, resulting displacement thickness from present method (shown as a diamond) as well as viscous flow model's displacement thickness prediction.

Appendix B

Boundary Layer Construction

The boundary layer solver gives such integral quantities as the displacement thickness, δ^*, the momentum thickness, θ, and the shape factor, H. However, it does not give any insight of the shape of the boundary layer. Swafford (1983) presents a method of constructing two-dimensional turbulent boundary layers from H and Re_θ.

The method is based on Whitfield's method (Whitfield, 1978) which composes the boundary layer of an inner and outer solution. The inner solution is able to treat both attached and separated flow and is given by the first term in equation (B.1). The outer solution must vanish near the wall and reach unity as it approaches infinity. The following equation meets both requirements:

$$
\begin{aligned}
u^+ = \frac{s}{0.09} \tan^{-1}(0.09y^+) \\
+ (u_e^+ - \frac{s\pi}{0.18}) \tanh^{1/2}[a(\frac{y}{\theta})^b]
\end{aligned}
\tag{B.1}
$$

where $u+$ is the mean stream-wise velocity normalized on the wall-friction velocity, $\sqrt{\tau_w/\rho}$, u_e^+ is the inner-law edge velocity, y^+ is the non-dimensional vertical distance, and s is a sign indicator, equal to one for attached flow and minus one for separated flow. These equations are given by:

$$u_e^+ = \left(\frac{2}{|C_f|}\right)^{1/2} \tag{B.2}$$

$$y^+ = \frac{Re_\theta}{u_e^+}\frac{y}{\theta} \tag{B.3}$$

$$\frac{u}{u_e} = \frac{u^+}{u_e^+} \tag{B.4}$$

$$s = \frac{C_f}{|C_f|} \tag{B.5}$$

The function $g(y/\theta)$ was chosen to give the best fit to numerous experimental velocity profiles, both attached and separated, and is given by:

$$g(y/\theta) = \tanh^{1/2}\left[a(\frac{y}{\theta})^b\right] \tag{B.6}$$

$$a = \tanh^{-1}[g^2(2)]/2^b \tag{B.7}$$

$$b = \frac{\ln\left(\frac{\tanh^{-1}[g^2(2)]}{\tanh^{-1}[g^2(5)]}\right)}{\ln(\frac{2}{5})} \tag{B.8}$$

where a and b are found by matching the velocity distributions at $y/\theta = 2$ and $y/\theta = 5$ (Whitfield, 1978). Swafford's formula is based on an empirical correlation which is used to estimate C_f. This empirical correlation,

$$C_f = \frac{0.3e^{-1.33H}}{(\log_{10} Re_\theta)^{1.74+0.31H}}$$
$$+(1.1 \times 10^{-4})\left[\tanh\left(4 - \frac{H}{0.875}\right) - 1\right] \tag{B.9}$$

is based on three source: (a) inferred values of C_f from equation (B.1), (b) Coles' Law of the Wall-Law of the Wake, and (c) measured velocity profiles. Furthermore, the correlation treats both attached and separated[1] flows.

---

[1]In which case C_f is negative

Appendix C

Experimental Data: Phase I

Figures C-1 - C-5 show all the velocity measurements taken in the boundary layer region during Phase I of the experiment. The data has been normalized with a free-stream velocity of 25 ft/s and a chord length of 12 in.
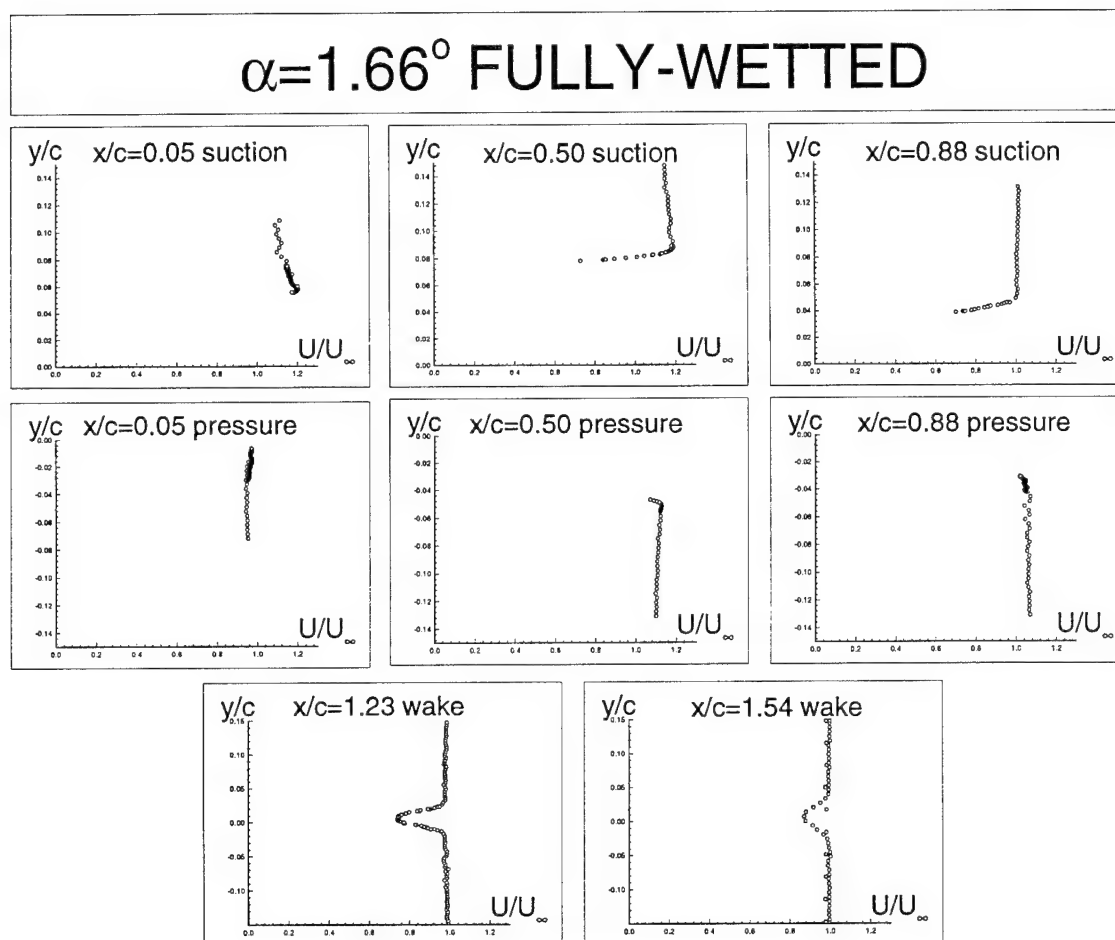
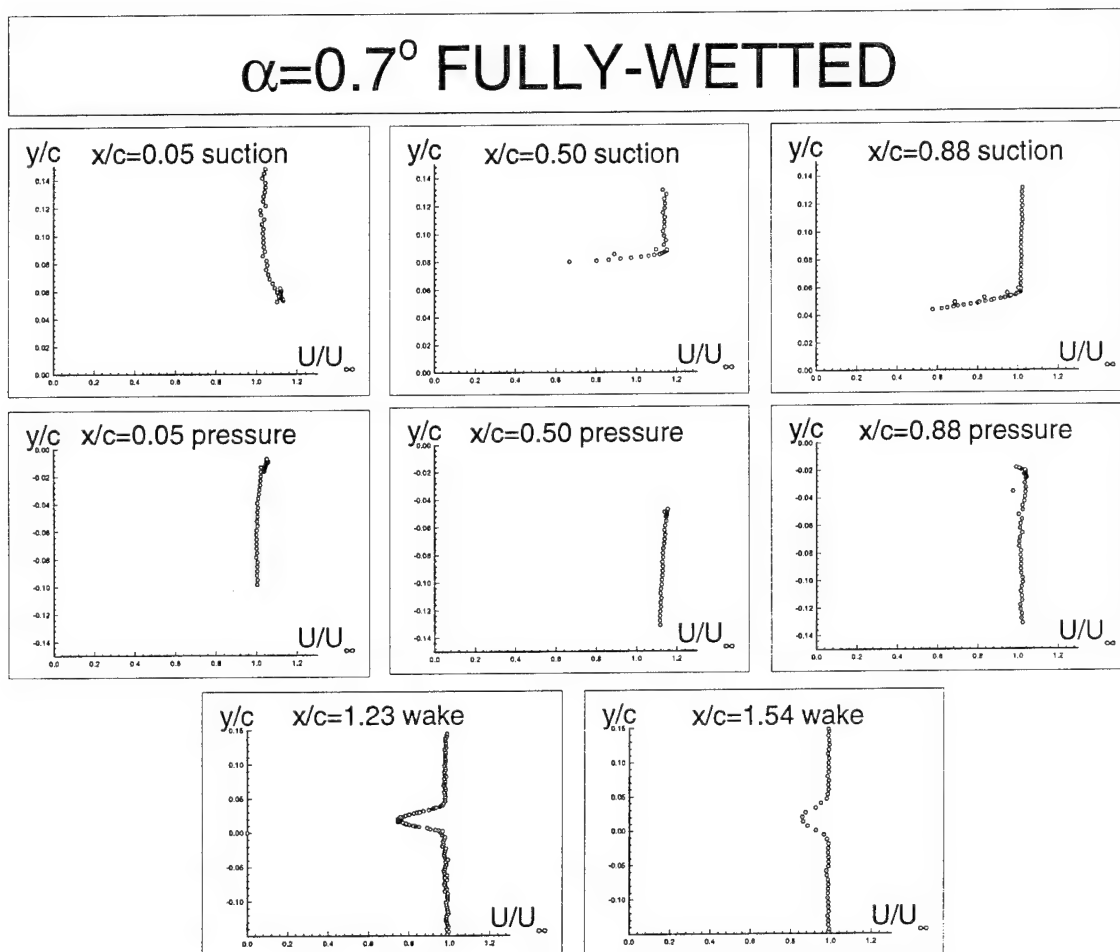Figure C-1: Experimental velocity measurements in the boundary layer region. $\alpha = 1.66°, fully - wetted$.

α=0.7° FULLY-WETTED

Figure C-2: Experimental velocity measurements in the boundary layer region. $\alpha = 0.7°, fully - wetted.$
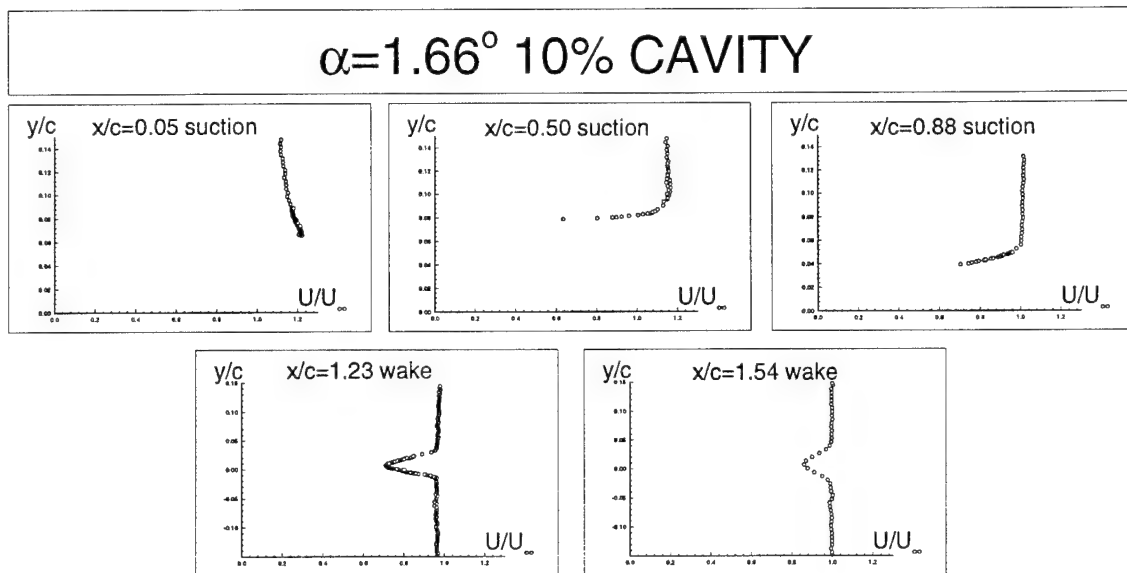
Figure C-3: Experimental velocity measurements in the boundary layer region. $\alpha = 1.66°, 10\%cavity$.
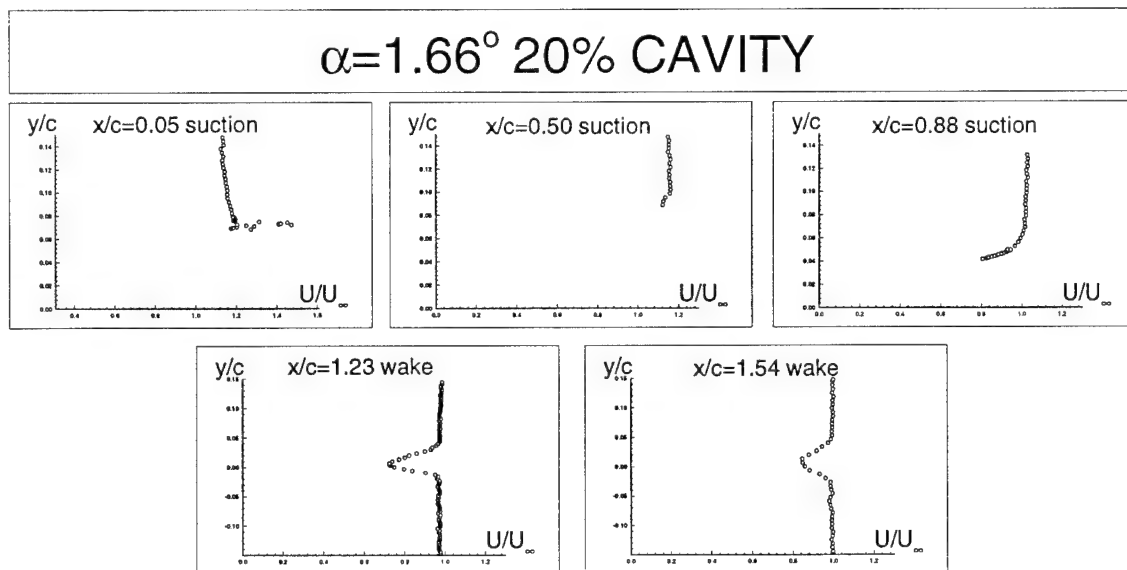
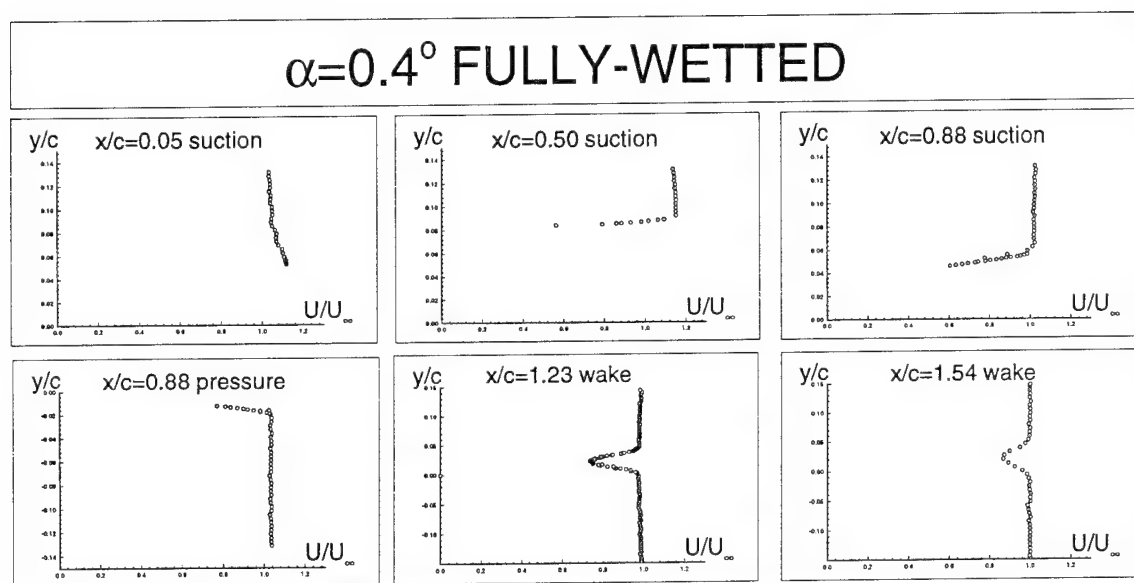Figure C-4: Experimental velocity measurements in the boundary layer region. $\alpha = 1.66°, 20\%cavity$.

α=0.4° FULLY-WETTED

Figure C-5: Experimental velocity measurements in the boundary layer region. $\alpha = 0.4^o, fully-wetted.$

Appendix D

Experimental Versus Numerical Results: Phase I

This appendix includes results from Phase I of the partially-cavitating hydrofoil experiment. In Phase I of the experiment, the following two problems constituted a high margin of error when compared to theory:

1. Only the horizontal beam was used in measuring the velocities in the boundary layer region. Thus, the laser could not measure velocities within 1 - 2 mm of the foil surface. Also, velocities measured are not those parallel to the foil.

2. The pressure side of the foil was not forced to turbulate. Therefore, the comparisons given in Phase I are shown as a function of laminar to turbulent transition location. The boundary layer solver uses an e^n "envelope" method to find the transition location. For this experiment, the e^n method predicted a transition location of approximately eighty percent of the chord length, which is not very likely for a Reynold's number of three million. Figure D-3 shows several boundary layers predicted by CAV2D-BL for various transition locations. From Figure D-3, one can infer the transition location which will produce the correct velocity profile downstream. Assuming that the boundary layer solver can accurately predict velocity profiles in fully-wetted flow, which is justified in Figure D-6, then Figure D-3 shows that the transition location tends towards $x/c = 0.1$ rather than $x/c = 0.8$. This

same behavior is evident in the wake as shown Figure D-4. Since the displacement thickness grows downstream, Figure D-4 is a much more sensitive measure of the transition location than D-6.

Cavity shapes and corresponding pressure distributions are shown in Figures D-1 - D-2. Figure D-2 is particularly interesting, a case where *two* cavities formed on the hydrofoil: leading edge cavitation and bubble/midchord cavitation. Two cavities were generated by first producing the leading edge cavity using PCPAN, then using the "compound" foil as an input to PCPAN, to generate the midchord cavity. The pressure distribution shown in Figure D-2 shows two cavitation numbers, which means the leading edge cavity does not satisfy the dynamic boundary condition.

Figure D-5 - D-6 compare velocity profiles between experiment and theory. Each profile is taken on the suction side of the foil. Figure D-5 shows essential differences in the shape of the boundary layer due to the increased momentum deficit owing to the cavity (see Section 5.2.3).

Finally, lift and drag coefficients are plotted against transition location in Figures D-7 - D-9. These results are very displeasing, but with all the many corrections made since Phase I, the current lift and drag are shown to agree very well with theory as shown in Figure 5-1.

No conclusion should be contrived, as to the accuracy of the numerical method, from the comparisons shown in this Appendix. The intention of this data is to present a collectively exhaustive set of data from which people may learn what works and what does not.
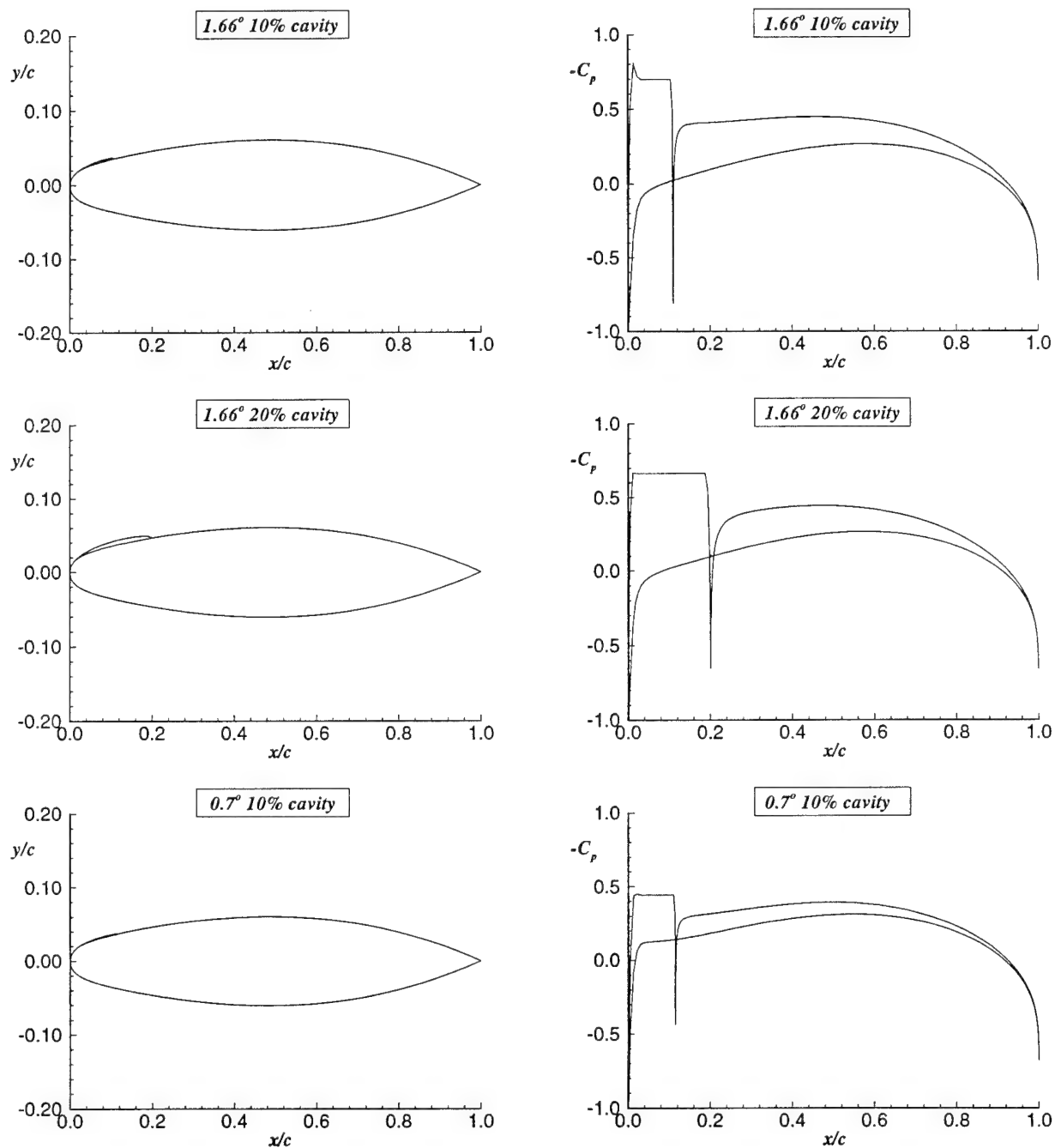
Figure D-1: Left: the inviscid cavity model with 10% cavity and $\alpha = 0.7^\circ$. Right: the corresponding pressure distribution. (10% 20% (1.66°), 10% (0.7°))
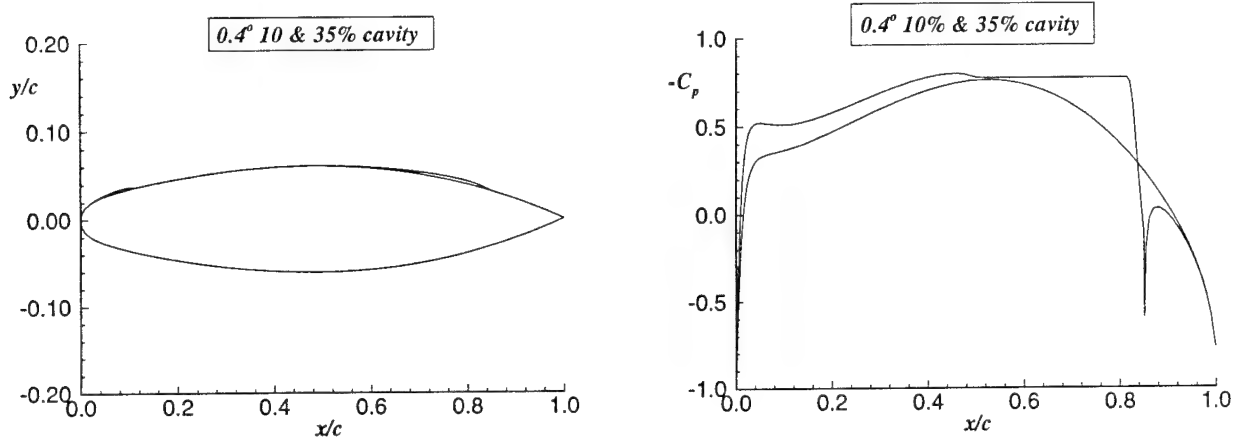
Figure D-2: Left: the inviscid model's versatility allows the prediction of two cavities. 10% and 25% cavities $\alpha = 0.4^\circ$ Right: corresponding pressure distribution.
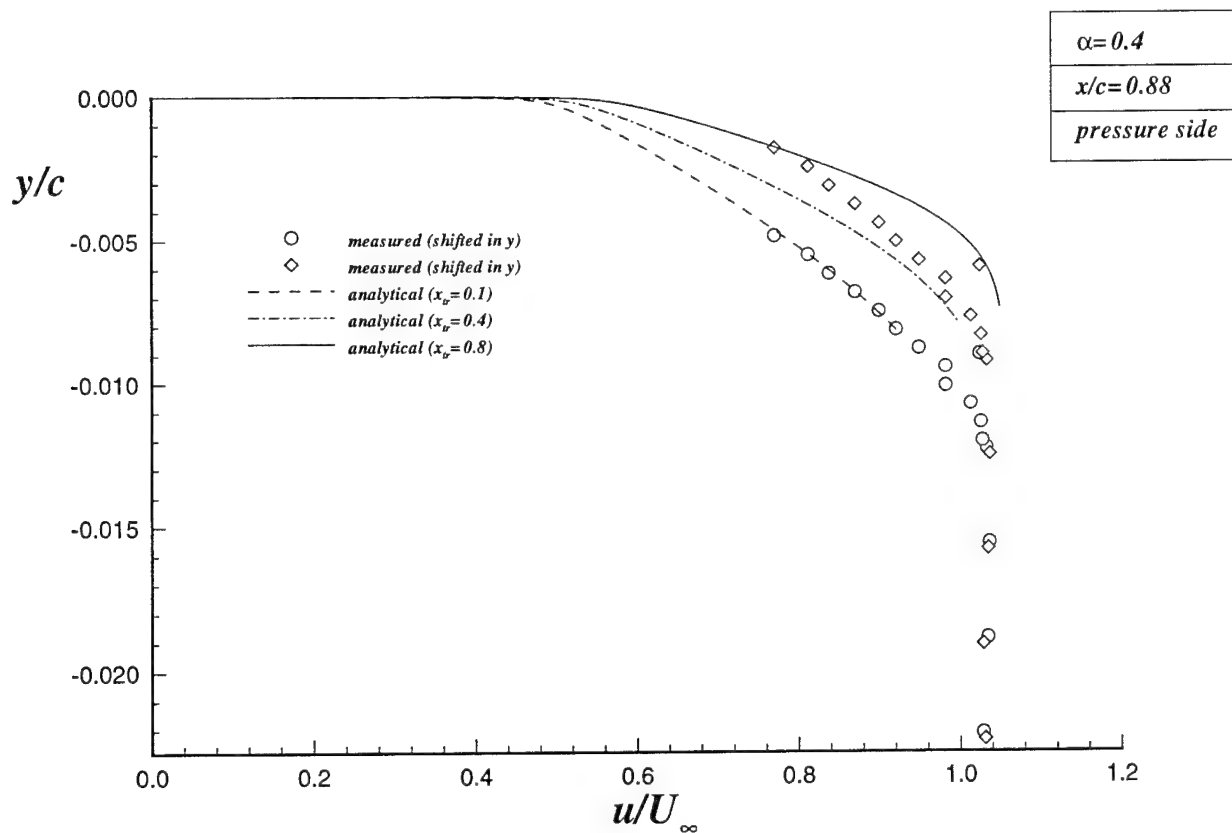

Figure D-3: Velocity profiles for both experimental and analytical showing the effect of transition location on the boundary layer. The measured profile has been arbitrarily shifted vertically due to the ambiguity in the foil surface.
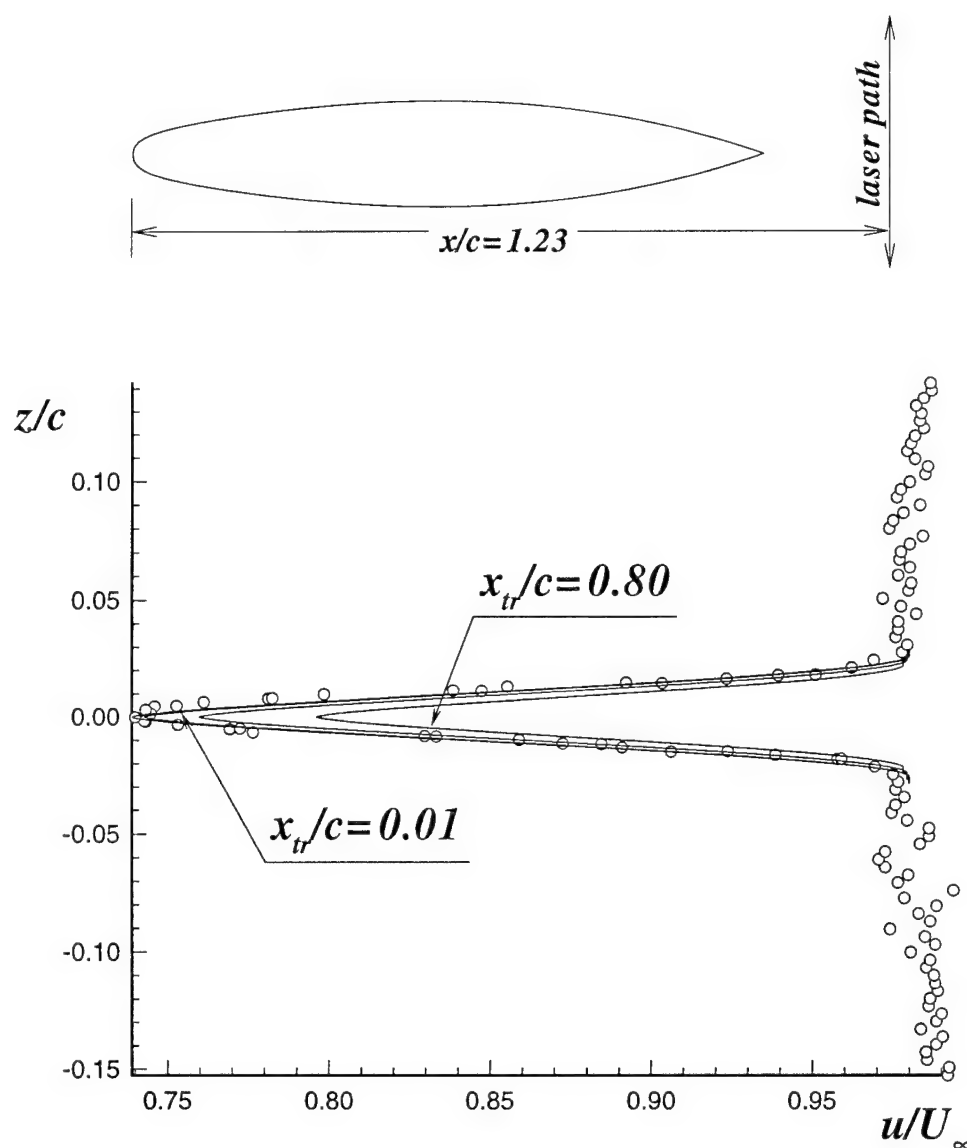
Figure D-4: Prediction of velocity profile in wake for various (pressure-side) transition locations. $\alpha = 1.66°$, $fully - wetted$
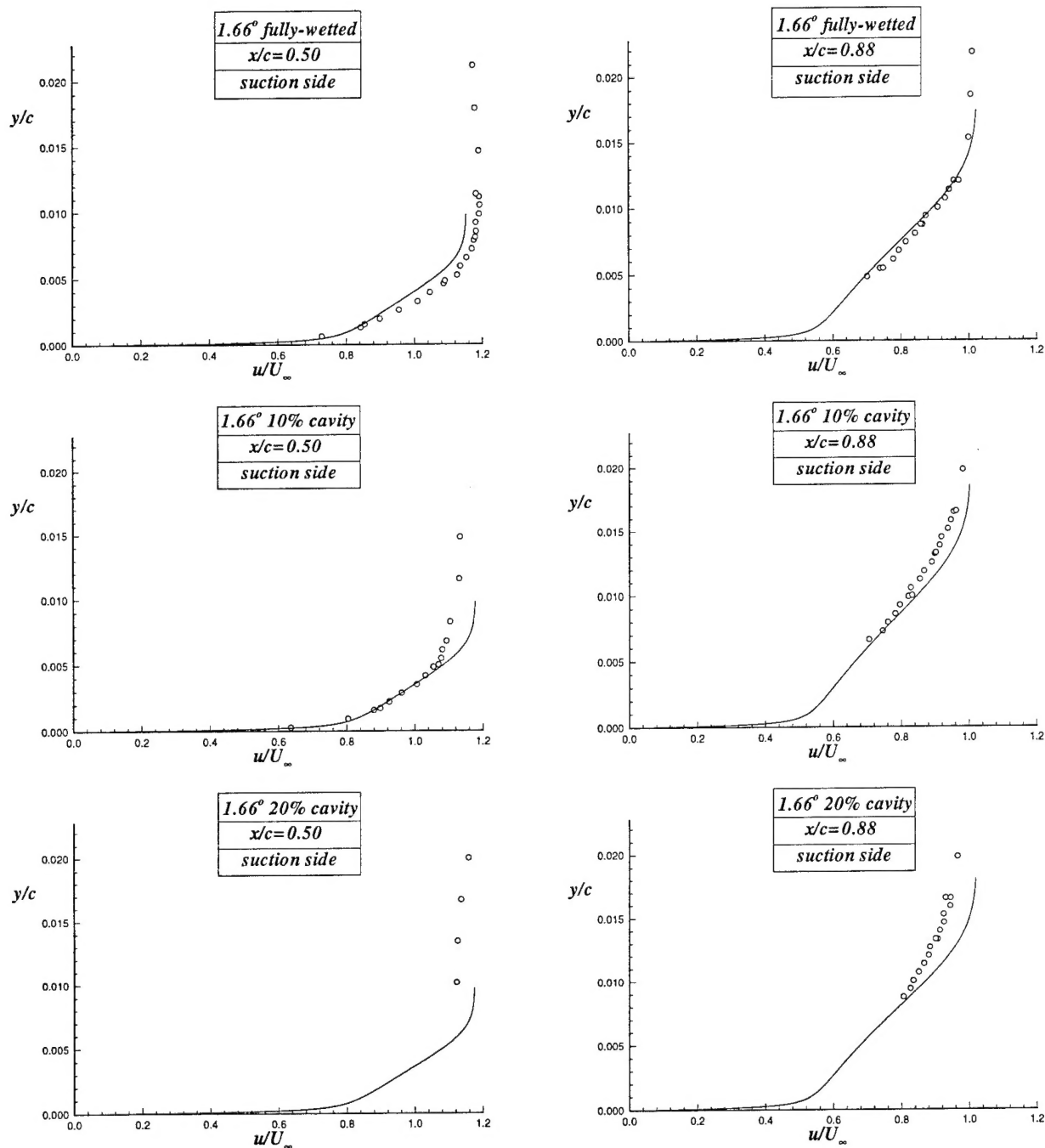
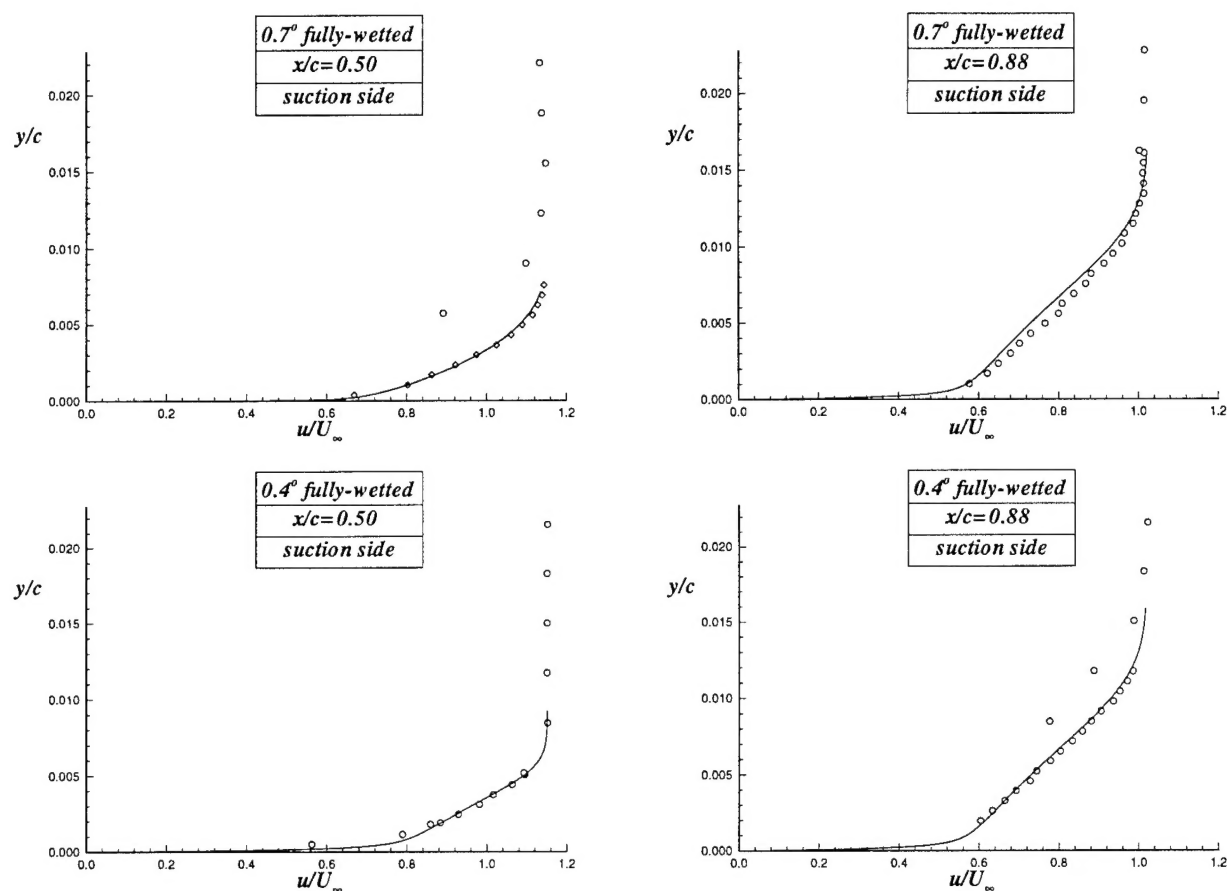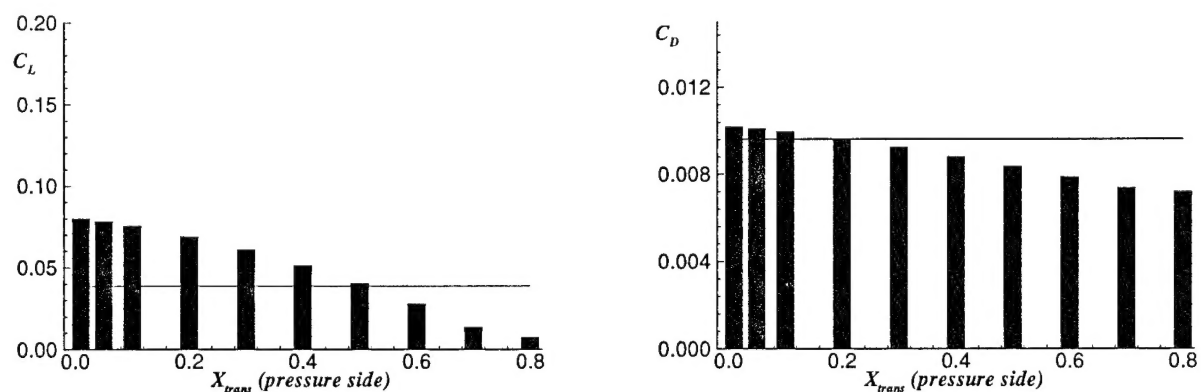Figure D-5: Velocity profile comparisons between experiment and viscous model.

Figure D-6: Velocity profile comparisons between experiment and viscous model.

Figure D-7: Lift and drag coefficients as a function of transition location, on the pressure side of the foil. Fully-wetted, $\alpha = 0.7°$.
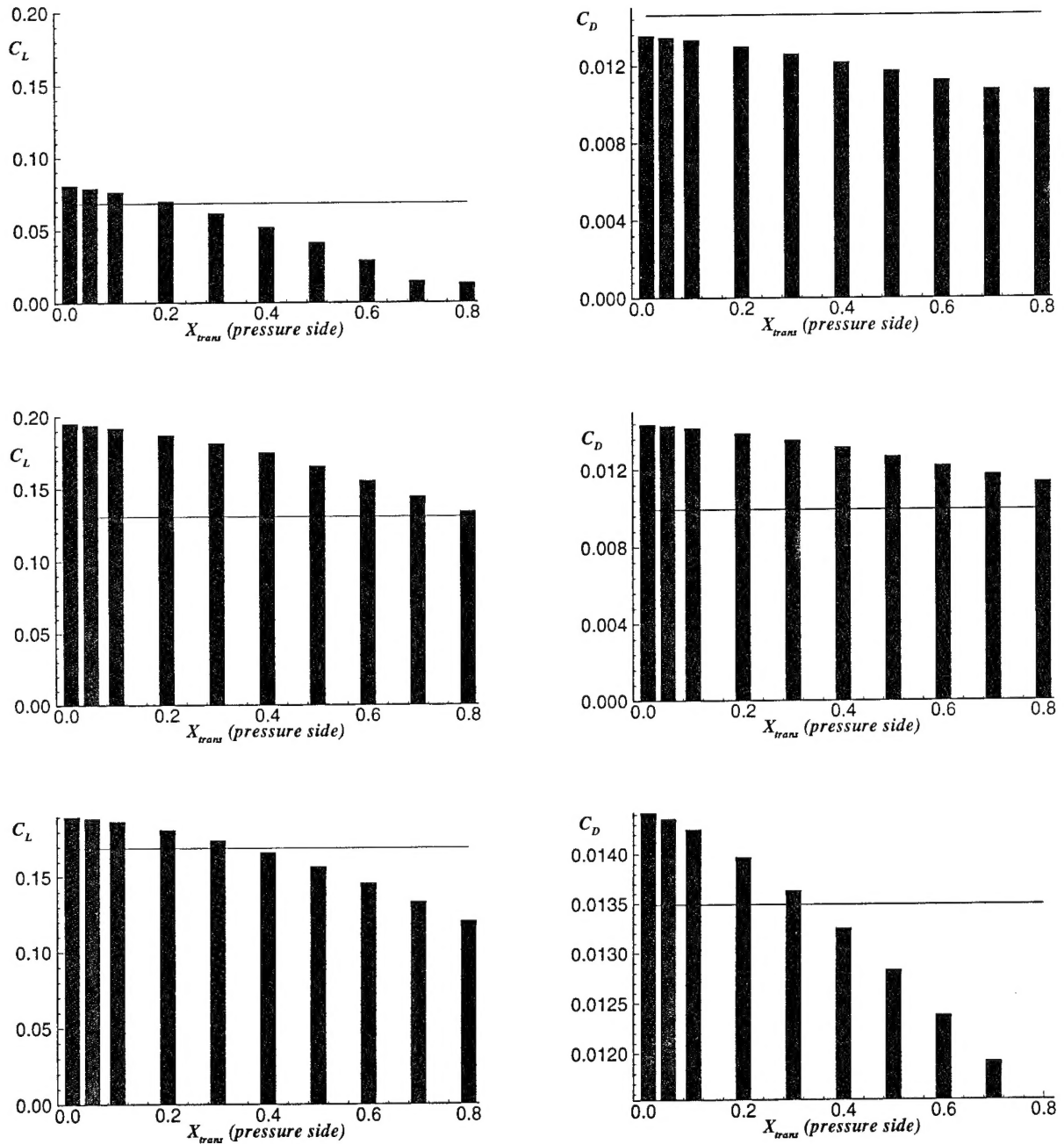
Figure D-8: Lift and drag coefficients as a function of transition location, on the pressure side of the foil. Cavity flow, $\alpha = 1.66°$, $l/c = 0.20$.
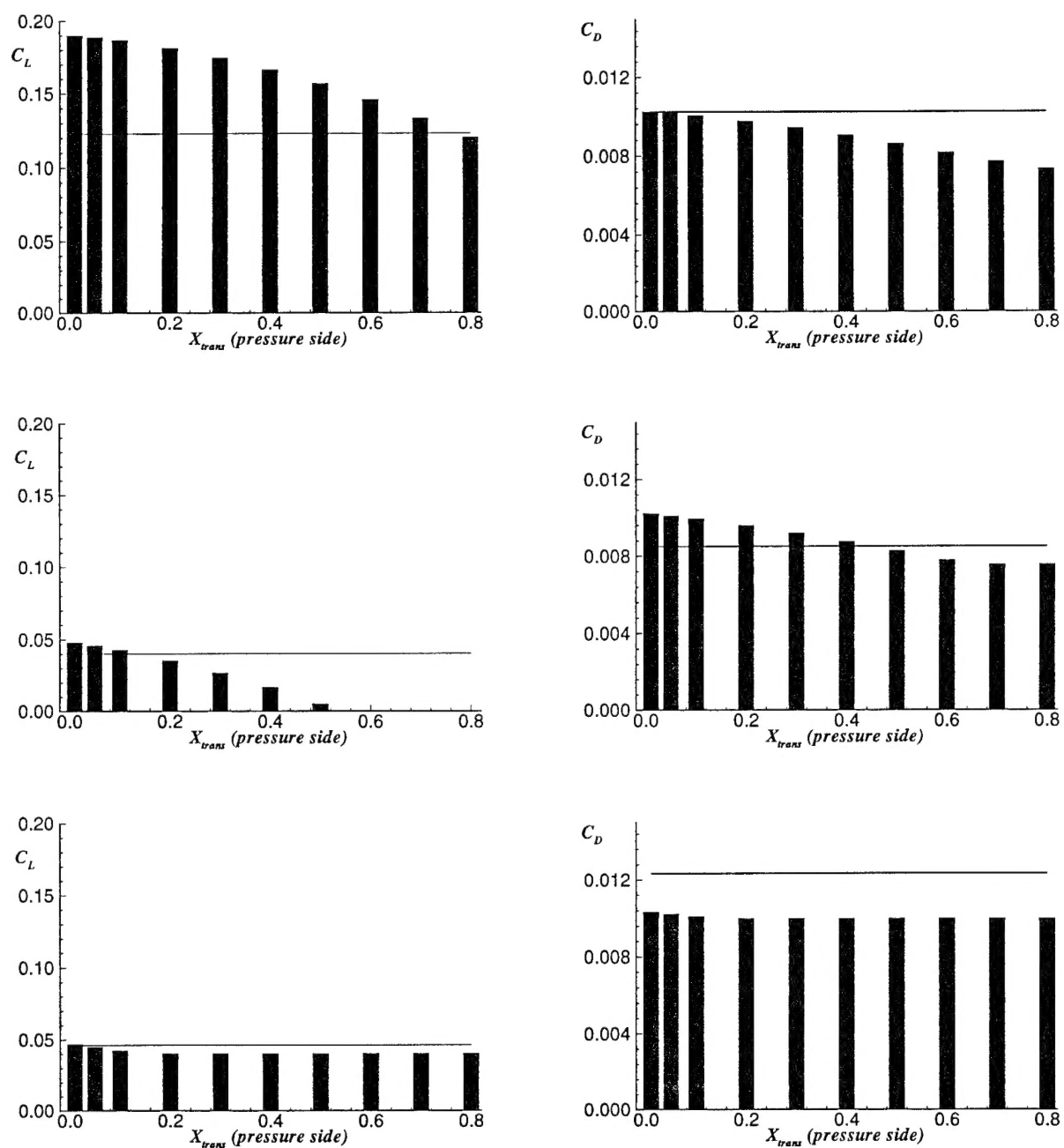
Figure D-9: Lift and drag coefficients as a function of transition location, on the pressure side of the foil. Cavity flow, $\alpha = 0.4°$, $l/c = 0.45$.